

The Pennsylvania State University

The Graduate School

College of Engineering

**A NONCOVALENT ROUTE FOR PREPARING HYBRID
NANOSTRUCTURES USING PARYLENE NANORODS AS
TEMPLATES**

A Dissertation in

Engineering Science and Mechanics

by

Niranjan A. Malvadkar

© 2010 Niranjan A. Malvadkar

Submitted in Partial Fulfillment
of the Requirements
for the Degree of

Doctor of Philosophy

May 2010

The dissertation of Niranjan A. Malvadkar was reviewed and approved* by the following

Melik C. Demirel
Associate Professor of Engineering Science and Mechanics
Dissertation Adviser
Chair of Committee

Mirna Urquidi-Macdonald
Professor of Engineering Science and Mechanics

Ivica Smid
Associate Professor of Engineering Science and Mechanics

David L. Allara
Professor of Polymer Science and Chemistry

Walter J. Dressick
Senior Research Manager and Chemist
Center for Bio/Molecular Science and Engineering
US Naval Research Laboratories, Washington, DC 20375
Special Member

Judith A. Todd
Professor of Engineering Science and Mechanics
P. B. Breneman Department Head

*Signatures are on file in the Graduate School.

Abstract

In this thesis, a methodology to prepare hybrid nanostructures of metals and ceramics on obliquely aligned, quasi-periodic poly(chloro-*p*-xylylene) (Parylene-C) nanorods (nanoPPX) templates *via* a noncovalent route is described. NanoPPX templates are deposited using a modified vapor deposition technique called oblique angle polymerization (OAP) which directs the monomer flux at an angle (typically $\sim 10^\circ$) to the substrate. In a typical procedure to prepare hybrid nanostructures, an aromatic ligand, such as pyridine, is first physisorbed onto the nanoPPX surface by means of treatment with either aqueous solution of the ligand or ligand vapors. Subsequently, a Pd(II)-based colloidal dispersion is covalently ligated to the pyridyl N-sites that provides the catalytic sites where metal reduction is facilitated. Deposition of various metals such as, but not limited to, Ni, Co, Cu, and Ag can be carried out onto the Pd(II)-laden nanoPPX films using an appropriate electroless plating bath. Besides metals, thin layer of ceramics (*e.g.*, TiO₂) can also be deposited using the noncovalent functionalization methodology. Metals or ceramic layer is deposited conformally to the underlying PPX nanorods and exhibits high adhesion strength despite the presence of noncovalent forces at the interface. In contrast, analogous plating procedure on conventionally deposited (*i.e.*, without any directional constraint to the monomer flux) “planar” (devoid of any nano-morphological features) PPX films show no or patchy metallization with poor adhesive properties. A statistical investigation using factorial analysis suggests that the ligand adsorption

condition (*i.e.*, aqueous or vapor treatments) profoundly impacts the morphology of the metal layer due to the pyridine orientation at the nanoPPX surface.

The adsorption and stabilization of pyridine molecules occurs *via* preferential π - π interactions with the aromatic moieties of the PPX chain. A detailed investigation of the nanoPPX porosity using gas physisorption study and a complementary study of pyridine adsorption using a quartz crystal microbalance (QCM) suggest that irreversible pyridine penetration occurs into the micropores of size ~ 1 – 2 nm that dominates the nanoPPX structure. On the other hand, planar PPX film cannot incorporate enough ligand due to lack of micropores necessary for pyridine stabilization, resulting in poor metallization.

The thesis also explores three applications of these hybrid nanostructures prepared by the noncovalent route in which the quasi-periodicity of the PPX nanorods and the tunability of the deposited metal nanostructured morphology are effectively leveraged. In the first application, Co membranes grown on nanoPPX surface, exhibiting highly interconnected porous structure, are shown to function as excellent catalysts for hydrogen production from NaBH_4 decomposition. The second application employs the quasi-periodicity of the underlying nanoPPX morphology by using Ag/nanoPPX hybrid nanostructures as surface-enhanced Raman spectroscopy (SERS) platforms for RSV gene detection. Finally, a preliminary investigation exploring the prospects of TiO_2 /nanoPPX nanocomposites as orthopaedic implant coatings is presented.

Table of Contents

List of Figures	vii
List of Schemes	x
List of Tables	xi
Acknowledgements	xii
Chapter 1. Thesis Overview	1
1.1. Background.....	1
1.1.1. Electroless Metallization of Polymer Surfaces.....	1
1.1.2. Ordered Nanomaterials.....	4
1.1.3. Noncovalent Strategy for Electroless Metallization.....	6
1.2. Research Objectives.....	7
1.3. Thesis Organization.....	8
1.4. Representative Publications.....	10
References.....	12
Chapter 2. Metal/NanoPPX Hybrid Nanostructures	17
2.1. NanoPPX.....	17
2.1.1. NanoPPX Deposition.....	17
2.1.2. Chemistry of PPX Formation.....	20
2.1.3. Mechanism of NanoPPX Formation.....	22
2.1.4. Physicochemical Properties of NanoPPX.....	26
2.2. Preparation of Metal/NanoPPX Hybrid Nanostructures.....	27
2.2.1. Noncovalent Ligand Functionalization.....	28
2.2.2. Surface Catalyzation.....	29
2.2.3. Electroless Metal Plating.....	30
2.3. Preliminary Metal Growth Model.....	30
2.4. Chemical Analysis.....	35
2.5. Factorial Analysis.....	42
2.6. Model Refinement.....	47
2.7. Summary.....	50
References.....	52
Chapter 3. TiO₂/NanoPPX Hybrid Nanostructures	55
3.1. Introduction.....	55
3.2. Preparation of TiO ₂ /nanoPPX Hybrid Nanostructures.....	56
3.3. Mechanism for Ceramization of NanoPPX Film.....	57
3.4. Effect of Ligand Functionality.....	59
3.5. Effect of LPD Bath Time.....	64
3.6. Chemical Analysis.....	66
3.7. Nature of Crystallinity.....	71
3.8. Summary.....	72
References.....	74

Chapter 4. Mechanism of Noncovalent Ligand Adsorption.....	78
4.1. Introduction.....	78
4.2. Experimental.....	79
4.3. Results and Discussion	81
4.3.1. Nature of Noncovalent Interactions	81
4.3.2. Effect of PPX Morphology on Pyridine Adsorption.....	84
4.3.3. Effect of Annealing on Pyridine Adsorption and Metallization	94
4.4. Summary	102
References.....	104
Chapter 5. Applications.....	106
5.1. Catalyst for Hydrogen Production	106
5.1.1. Introduction.....	106
5.1.2. Preparation of Co Catalyst.....	110
5.1.3. Hydrogen Release Rate Measurement	111
5.1.4. Summary	117
5.2. Surface-Enhanced Raman Spectroscopy Substrates	119
5.2.1. Introduction.....	119
5.2.2. Preparation of NanoPPX-Templated SERS Substrates	122
5.2.3. Preparation of Molecular Probes	124
5.2.4. Characterization of SERS Substrates.....	125
5.2.5. Mechanism of Metal Growth.....	126
5.2.6. Structure of SERS Substrates.....	127
5.2.7. SERS Properties.....	132
5.2.8. Influence of Metal Structure on EF	135
5.2.9. RSV Gene Detection.....	137
5.2.10. Summary	139
5.3. Orthopaedic Implant Coatings	141
5.3.1. Introduction.....	141
5.3.2. Experimental Procedure.....	144
5.3.3. Results and Conclusions	146
References.....	149
Chapter 6. Conclusions and Recommendations for Future Work	155
References.....	158
Appendix A. Statistical Analysis of Ni Film Roughness Variations	159
Appendix B. Gas Physisorption: Background and Theory	168
Appendix C. Quartz Crystal Microbalance: Background and Theory.....	175
Appendix D. Nontechnical Abstract	180

List of Figures

2-1. Effect of variation of deposition parameters, namely, the incidence flux angle (α) and the axial substrate rotation speed (ω) on the cross-sectional morphology of PPX film.....	25
2-2. Co metallization on (A) nanoPPX and (B) planar PPX <i>via</i> noncovalent pyridine functionalization.	33
2-3. (A) Contact mode AFM image of pristine nanoPPX film. (B) Contact mode AFM image of Ni film deposited on nanoPPX functionalized using aqueous pyridine treatment.	33
2-4. SEM image showing cross-section of the Ni/nanoPPX composite film etched using FIB..	34
2-5. High resolution XPS spectra of N 1s region.....	36
2-6. High resolution XPS spectra of Pd 3d region.....	38
2-7. High resolution XPS spectra of Ni 2p region.	41
2-8. Contact mode AFM image of Ni layer deposited on nanoPPX films functionalized using (A) aqueous pyridine treatment and (B) vapor pyridine treatment..	46
3-1. FESEM image of TiO ₂ deposited on PPA-functionalized (A) nanoPPX film, and (B) planar PPX film.	58
3-2. TiO ₂ adhesion tape test results. SEMs are shown for TiO ₂ films deposited onto nanoPPX films bearing PPA or TPH ligand before and after tape removal.....	62
3-3. TEM image of TiO ₂ particles deposited on PPA-functionalized nanoPPX film.	64
3-4. Dependence of thickness of TiO ₂ layer and contact angle on LPD bath time.....	66
3-5. XPS spectra of PPA-functionalized nanoPPX film in (a) P(2p) region, (b) O(1s) region.	67
3-6. XPS spectra of TiO ₂ deposited on PPA-functionalized nanoPPX film in (a) Ti(2p) region, (b) O(1s) region. XPS spectra of TiO ₂ deposited on TPH-functionalized nanoPPX film in (c) Ti(2p) region, (d) O(1s) region.....	69
3-7. XRD spectra of TiO ₂ films: (A) as-deposited; (B) after annealing (200°C, 24 h, Ar).....	71

4-1. SEM image of Ni layer deposited on nanoPPX film functionalized with 1 M aqueous solution of amylamine (left) and 0.1 M aqueous solution of 2,2'-bipyridine (right).....	82
4-2. Adsorption of pyridine (aq, 1 M) and amylamine (aq, 1 M) in a nanoPPX film monitored using a QCM	83
4-3. X-ray diffraction (XRD) patterns of nanoPPX and planar PPX films.....	85
4-4. Vapor phase adsorption of 10 mM pyridine on nanoPPX and planar PPX films monitored using QCM.	86
4-5. Vapor phase pyridine adsorption isotherm on nanoPPX and planar PPX films.....	86
4-6. N ₂ adsorption and desorption isotherms at 77.35 K on planar PPX and nanoPPX films.	88
4-7. Differential pore volume distribution obtained from BJH method using N ₂ isotherm data on planar and nanoPPX films at 77.35 K.....	90
4-8. CO ₂ adsorption isotherm on pristine and pyridine-functionalized nanoPPX film...	91
4-9. Linearized DA plot obtained from CO ₂ adsorption data.	93
4-10. Differential pore size distribution obtained from CO ₂ adsorption data on pristine and pyridine (aq)-functionalized nanoPPX.....	94
4-11. XRD pattern of four distinct nanoPPX films annealed at 388, 413, 443 and 493 K per the procedure described in Section 4.3.	95
4-12. Plot of (A) equilibrium frequency shifts (Δf_s) normalized with the film thickness (t), and (B) equivalent resistance change (ΔR) against pyridine (aq) concentration.....	97
4-13. Plot of frequency shifts (Δf_s) normalized with the film thickness (t) against equivalent resistance change (ΔR).	98
4-14. Plot of Co/C (at. % ratio) against annealing temperature of nanoPPX film.....	99
5-1. Effect of Co plating time on the hydrogen release rate	112
5-2. Plots showing Co weight percentage (from EDX) and surface roughness (from AFM) of Co membrane deposited on nanoPPX film with respect to Co plating time. First-order exponential decay fits for both plots are shown for visual assistance.	113
5-3. Hydrogen collected from catalytic decomposition of alkaline stabilized aqueous NaBH ₄ solution using Co film deposited on helical nanoPPX templates treated with aqueous and vapor pyridine.	115

5-4. FESEM images showing topography of Co film deposited on helical nanoPPX films treated with (A) aqueous and (B) vapor pyridine, respectively, after 1 min Co plating.	116
5-5. FESEM image of SERS-active Ag substrate prepared <i>via</i> (A ₁) Scheme A (<i>cf.</i> Sample 3 in Table 5-6); (B ₁) Scheme B (<i>cf.</i> Sample 7 in Table 5-6);	129
5-6. Contact mode AFM images of Scheme B substrates plated for 5, 30, 60 and 150 min in Ag bath..	130
5-7. Particle size distribution (right) obtained from TEM images (left) of scarped-off Ag particles deposited on nanoPPX film <i>via</i> (A) Scheme A (<i>cf.</i> Sample 3 in Table 5-6); and (B) Scheme B (<i>cf.</i> Sample 7 in Table 5-6).	131
5-8. SERS spectra of FBT on substrates prepared <i>via</i> (A) Scheme A, and (B) Scheme B. (C) Raman spectrum of pure FBT. (D) Plot of EF (calculated from $\nu(\text{C-F})$ peak at 1074 cm^{-1}) against Ag plating time.	133
5-9. SERS spectrum of non-hybridized (top) and hybridized (bottom) Cy5-MP-SC6 molecular probe immobilized on Ag/nanoPPX (<i>via</i> Scheme B) substrate.	139
5-10. Differentiation of hMSCs to osteoblasts on various substrates kept in differentiation medium for 14 days.	147
5-11. Differentiation of hMSCs to osteoblasts on TiO ₂ /NanoPPX surfaces (B to D) prepared by varying LPD bath time.	148

List of Schemes

2-1. Schematic of an unmodified version of a Labcoter™ 2 system used for depositing planar PPX films	18
2-2. Schematic of a modified version of a Labcoter™ 2 system used for depositing planar PPX films	19
2-3. Vapor phase deposition of poly(chloro- <i>p</i> -xylylene) (PPX) from dichloro-[2.2]-p-cylcophane (DCPC) <i>via</i> Gorham's method.	22
2-4. Schematic of the formation of conformal metal film on nanoPPX <i>via</i> the noncovalent electroless metallization process.	28
2-5. Surface effects model for metallization of poly(chloro- <i>p</i> -xylylene) (PPX) films ...	31
2-6. Cartoon showing effect of ligand adsorption condition on resulting metal surface morphology	48
3-1. Schematic showing preparation of hybrid TiO ₂ /nanoPPX nanostructures using a two-step procedure.....	56
4-1. Cartoon showing effect of annealing on metal deposition rate.....	101
5-1. NanoPPX-templated SERS substrates prepared <i>via</i> (A) commercial Pd/Sn catalyst treatment; (B) noncovalent pyridine adsorption followed by PD1 treatment.....	126
5-2. Molecular structures of Cy5-MP (left) and SC6 linker (right).	138

List of Tables

2-1. Influence of morphology of PPX film on various physicochemical properties.....	27
2-2. Quantified metallization data.....	36
2-3. Summary of the 2 ⁴ factorial analysis for Ni deposited nanoPPX films. ¹⁵	44
3-1. TiO ₂ deposition on ligand-treated nanoPPX films ²³	61
4-1. Surface area and porosity data from N ₂ and CO ₂ adsorption isotherm.....	89
5-1. DOE-established targets for on-board hydrogen storage systems. ⁶	107
5-2. Comparison of hydrogen release rates from catalytic decomposition of NaBH ₄ on various catalysts.....	117
5-3. Designed RSV Probes.....	124
5-4. Modifications and Synthesis	125
5-5. Comparison of the SERS substrates.	128

Acknowledgements

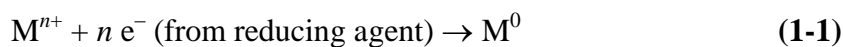
Foremost, I owe my deepest gratitude to my thesis adviser, Prof. Melik Demirel, for his invaluable advice, support, and motivation throughout my doctoral research at Penn State. His passion for exploring novel research ideas has been and will be a great motivating force in my research career. I am indebted to Dr. Walter Dressick for his thorough review of all my research papers, which has immensely improved my critical thinking and scientific writing skills. I am also grateful to Prof. David Allara for allowing access to the Raman equipment in his lab and to Prof. Henry Donahue (Penn State Hershey Medical School) for the cell-growth experiments. I also thank other committee members, Prof. Ivica Smid and Prof. Mirna U-Macdonald, for their insightful reviews and suggestions to improve my thesis. I am thankful to my fellow group members: Murat Cetinkaya, Hui Wang, Eric So, Ping Kao, Koray Sekeroglu, Gökhan Demirel and others for their assistance and the wonderful conversations we had on various research topics. I also thank the MCL technical personnel: Josh Maier, Nichole Wonderling, Mark Angelone, John Cantolina, Magda Salama, and Vince Bojan for instrument training, and assistance in data collection. My parents and my brother deserve my profound gratitude for their encouragement and patience throughout my education. Finally, I gratefully acknowledge the financial support from the Office of Naval Research, without which this research would not have been possible.

Chapter 1. Thesis Overview

1.1. Background

1.1.1. Electroless Metallization of Polymer Surfaces

Electroless metallization, as the name suggests, is an autocatalytic metal-ion reduction reaction used for metallizing insulating (*e.g.*, polymer) surfaces without application of an external electric source.¹⁻⁵ Unlike vapor-phase deposition methods, the process is simple, does not require sophisticated equipment, and can be performed in ambient conditions. In electroless metallization, electrons required for reducing the metal ions are provided by a reducing agent present in the plating bath. Typically, noble metals (*e.g.*, Pt, Au and Ag) and first-row transition metals (*e.g.*, Ni, Co, and Fe) can be deposited *via* electroless metallization because the half-cell potentials for the metal reduction reaction for these metals are lower compared to half-cell potentials for oxidation of typical reducing agents, resulting in a negative Gibbs free-energy that drives the redox reaction forward. In general, an insulating surface requires surface conditioning and catalyzation prior to electroless metallization (*vide infra*). The overall metal reduction reaction can be written as:



Metallized polymer surfaces prepared by electroless metallization have applications in a wide variety of areas, including microelectronics,⁶⁻¹⁰ biomedical devices,^{11,12} catalysis,¹³ automotive,¹⁴ and food packaging.¹⁵ The metal/polymer interface properties are therefore an important consideration during manufacturing of such

components. Obtaining a good metal/polymer interface is often a challenge due to the chemical incompatibilities between many metals and polymers, especially low-energy polymers.^{9,16-18} Poor adhesion of metal layers to polymer surfaces limits the usage of electroless metallization for many practical applications. Attaining acceptable metal/polymer interface adhesion usually requires prior chemical pretreatment of the polymer surfaces through techniques such as excimer UV,¹⁹⁻²¹ laser ablation,²² plasma,²³ and wet chemical treatments²⁴ and/or microscopic roughening to promote metal anchoring to the film.² The roughening is usually carried out by techniques such as mechanical roughening,²⁵ laser treatment,²⁶ low-energy ion treatment,²⁷ chemical etching,²⁸ phase separation induced roughening,³¹ silver nanopowder coating,³² or photolithography.³³ These surface conditioning steps are often harsh and degrades the desirable physicochemical properties of the surface, thereby limiting the material selection for electroless metallization.

The roughened polymer films are then chemically functionalized by a catalytic species that seeds the electroless metallization process. Typically, the functional species consists of a commercial bimetallic colloid with a low-valent Pd-core and a β -stannic shell.^{34,35} While the low-valent Pd-core promotes the initiation of the metallization process, the β -stannic shell allows binding the colloid to the roughened polymer surface.³⁶ In order to initiate the metallization reaction, the Pd-core needs to be exposed after the adsorption of the bimetallic colloid on the polymer surface. This procedure entails careful control of the treatment time and acid concentration, so as to ensure not to remove any part of the β -stannic shell that is bound to the polymer surface.

Metallization is generally carried out using commercially available baths. The composition of these electroless baths consists of a source of metal ions, reducing agent, complexing agent, and stabilizer or inhibitor.² For example, in many commercial nickel baths, nickel sulfate is used as the nickel source while sodium hypophosphite is the reducing agent. Complexing agents such as NH_4^+ ions are added to exert a buffering action that maintains the pH of the solution and reduces the concentration of free nickel ions that helps in preventing rapid precipitation of nickel. Stabilizers or inhibitors such as Sn^{+2} , Sb^{+2} are also added to prevent the decomposition of the bath. Bath decomposition occurs due to the formation of finely divided metal precipitate that acts as catalysts for the self-accelerating reduction chain reaction. Although electroless metallization processes in an industrial scale are highly optimized, it is always advantageous to reduce the number of processing step without compromising the quality of the metal layer and the interface strength.

Besides its scalability and ease of operation, there are two advantageous properties of electroless metallization, namely its selectivity and the conformal nature of the resulting metal surface. Since electroless metallization occurs on catalytic sites on the surface, metal deposition can be patterned by patterning the catalytic sites. Nanoscale metal patterning has numerous applications, especially in the microelectronic industry due to the ever-increasing demand for miniaturization of devices. Patterning at nanoscale can be achieved by means of lithographic techniques⁵ or using non-lithographic templates such as block copolymers,³⁷ polyelectrolyte multilayers,³⁸ phospholipid microtubules³⁹ *etc.* In non-lithographic templates, the catalytic species can be preferentially attached to sites within the template, thereby generating the pattern. For instance, charge bearing

catalytic colloids can preferentially bind at the seams of the helical phospholipid microtubules due to the higher electrostatic attraction at that location.³⁹

Conformal nature of electroless metallization, on the other hand, is the ability of the method to coat a surface uniformly irrespective of the geometry of the surface, provided the surface possesses a uniform surface coverage of the catalytic sites. Electroless metallization is therefore suitable for thin and uniform coating of macro and micro-geometries, allowing replication of the surface topology. In contrast, electroplating is relatively non-conformal, but has a higher rate of metal deposition; it is therefore applicable for depositing thicker coatings. Physical vapor deposition (PVD) methods too suffer from “line-of-sight” metallization, resulting in a metal layer that cannot completely infiltrate intricate geometries such as surface pores or undercuts. Continuous catalyzation inside sub-100 nm pores, high aspect ratio features, however, is a challenge due to surface tension and transport issues at such length scales. Blackburn *et al.* demonstrated the use of supercritical CO₂ (≥ 31.1 °C and ~ 73 atm) as the solvent for metal-ions and reducing agent as a means to circumvent the transport issues.⁴⁰ The supercritical CO₂ approach necessitates the use of high pressure reactors, thereby limiting it to small-batch manufacturing. In order to be industrially attractive, the entire metallization process, including surface catalyzation, has to be carried in the ambient without any special equipment.

1.1.2. Ordered Nanomaterials

Preparation of nanomaterials having specific order or alignment, rather than a randomly ordered/oriented or isolated synthesis, has received growing popularity due to

the enlarged scope of envisioned applications of such nanomaterials. Examples of such nanomaterials include metal-organic frameworks, superstructures of nanoparticles, anodic alumina membranes and aligned nanorods. Preparation of this class of nanomaterials is accompanied by the formation of ordered nano-porosity within adjacent nano-moieties. Aligned nanomaterials can therefore perform as ideal nano-templates or nano-frameworks on which other aligned nanomaterials could be synthesized.

One of most versatile, bottom-up techniques to create aligned nanomaterials is the oblique angle deposition (OAD), which has gained tremendous popularity in recent years. History of OAD, however, dates back to more than a century ago when physical vapor deposition using non-normal incidence of vapor flux on stationary substrate were studied. These studies include, works by Kundt on light birefringence on sputtered metal,⁴¹ Smith on anisotropy in permalloy film,⁴² Knorr and Hoffmann on magnetic anisotropy of Fe films,⁴³ and Holland on anisotropic Al film⁴⁴. Most of these studies observed anisotropic properties of films grown *via* non-normal incidence vapor flux and attributed this to the tendency of the metal grains in the film to grow towards the incident vapor flux. To date, several materials including metals,⁴⁵ ceramics,⁴⁶ semiconductors,⁴⁷ and organometallics⁴⁸ have been deposited by OAD using sophisticated deposition algorithms creating complex and exotic nanostructures.

Deposition of polymeric films possessing ordered nanostructures by oblique angle polymerization (OAP), a term used to denote simultaneous surface polymerization and oriented crystallite growth, was first demonstrated by Pursel *et al.*⁴⁹ The morphology of a polymeric film consists of obliquely aligned, parallel assemblies of polymer nanorods on a Si substrate. Later, Murat Cetinkaya, in his doctoral thesis, highlighted the

controllability and versatility of the OAP method for ordered polymeric nanostructured films with tunable physicochemical properties.⁵⁰ These advantageous properties of OAP-prepared polymeric nanostructured film can be employed in cutting-edge applications provided functionalization of the surface with metals, ceramics or other polymers is possible.

1.1.3. Noncovalent Strategy for Surface Functionalization

Noncovalent interactions are ubiquitous in nature, yet are responsible for some of the most complex molecular structures (*e.g.*, DNA, proteins *etc.*) and biological processes (*e.g.*, antibody–antigen association, enzyme–substrate binding, self-healing phenomenon *etc.*). Given the low binding energies of noncovalent interactions, biomolecules held together by such interactions are surprisingly stable. The stability of these biomolecules is the result of the cooperative binding effect exhibited by such interactions.⁵¹ Analogous strategy exploiting the cooperative binding effect of noncovalent interactions can be adopted in fabricating composites, chemically-modified templates and molecular superstructures *etc.* For instance, carbon nanotubes-based templates were prepared by noncovalent functionalization of its surface *via* hydrophobic interactions,⁵² π – π stacking with a polynuclear moiety (*e.g.*, pyrene),⁵² cation– π interactions,⁵³ or even charge transfer interactions⁵⁴. The noncovalent functionalization strategy was successfully implemented by Dressick *et al.* in fabricating patterned metal surfaces.⁵⁵⁻⁶⁰ In this work, aromatic ligand molecules were stabilized *via* π – π interactions in solvent-templated “nanocavities” created on self-assembled monolayer (SAM)-modified silicon substrates. Subsequently, the surface was treated with a catalytic Pd-based colloidal dispersion that selectively

attaches to the ligand sites, thereby generating a patterned seed layer for the subsequent electroless metallization step. Unlike covalent grafting methods, the noncovalent functionalization strategy is a benign and reversible means to chemically modify a surface, which preserves the desirable physicochemical properties of the underlying material.

1.2. Research Objectives

A concept paper by Demirel *et al.*, initiated the work for this thesis.⁶¹ In this paper, porous Ni membranes were grown *via* electroless metallization on OAP-grown nanostructured poly(chloro-*p*-xylylene) (nanoPPX) films. Physisorbed pyridine functionalized the nanoPPX surface that then ligated to a Pd(II)-based catalyst that seeded the electroless metallization process. A preliminary model was proposed for the Ni film growth which states that π - π interaction occurs when pyridine is physisorbed onto the nanoPPX film resulting in noncovalently bonded, but highly stable, ligand-sites. The paper also reported the lack of metallization of a conventionally deposited, planar PPX film using analogous functionalization and plating procedure. The poor metallization was attributed to the “compact” arrangement of PPX chains at the surface thereby restricting the amount of ligand adsorbed.

The aim of this thesis is two-fold: (1) to extend the concept of noncovalent ligand functionalization for the synthesis of nanoPPX-templated hybrid nanostructures of metals (besides Ni) and ceramics in order to enlarge the scope of applications of this methodology, and (2) to test the various hypotheses and conjectures proposed in the concept paper, which will further the understanding of the mechanism for noncovalent

functionalization. Specifically, the chemistry of the metal growth model, *i.e.*, the noncovalent interaction of pyridine with PPX and the covalent ligation of pyridine with Pd(II) will be analyzed using XPS. A systematic study will be carried out to evaluate the effect of various metallization parameters on the morphology of the deposited metal film using statistical design of experiments. The preliminary model described in the concept paper will be refined by incorporating the results of the statistical investigation and structural characterization of the metal layer. Further, the generality of the noncovalent functionalization approach will be appraised by depositing other metals (*e.g.*, Co, Ag, Cu *etc.*) and ceramic layers (*e.g.*, TiO₂) on the nanoPPX surface. A comparative study on the structure and porosity of a planar and nanoPPX film will be performed along with real-time *in situ* monitoring of pyridine adsorption to understand the mechanism of noncovalent functionalization. Finally, applications of these hybrid nanostructures will be explored in areas such as catalysis, SERS platforms and bioimplant coatings.

1.3. Thesis Organization

Chapter 2 introduces the concept of oblique angle polymerization (OAP) used for preparing nanoPPX films and some of its important aspects such controllability and tunability of nanoPPX morphologies. Further, the noncovalent functionalization methodology for preparing metal nanostructures on nanoPPX templates is explained in context to PPX–aromatic ligand systems. The chemistry of the metal growth model postulated in the concept paper is tested using XPS analyses. A two-level factorial analysis on the effect of metallization parameters establishes the importance of ligand adsorption conditions on the morphology of the metal layer. Finally, the preliminary

metal growth model is refined by incorporating the observed structural differences due to changes in the ligand adsorption condition.

Chapter 3 demonstrates the versatility of the noncovalent functionalization methodology by describing growth of a ceramic layer on a nanoPPX film. Ceramization is achieved by means of liquid phase deposition (LPD) of TiO₂ on nanoPPX film functionalized with aromatic ligands such as phenylphosphonic acid. Further, the physicochemical properties (*e.g.*, thickness of TiO₂, contact angle, surface coverage *etc.*) of TiO₂/nanoPPX are evaluated against the ligand functionality and LPD bath time. Finally, chemical and crystal structure analysis by XPS and XRD, respectively, provide further insight concerning the nature of TiO₂ deposits on nanoPPX.

Chapter 4 focuses on understanding the mechanism of pyridine incorporation into the nanoPPX structure. The study of pyridine adsorption mechanism entails a detailed analysis of the nanoPPX structure and porosity, which is achieved using XRD and gas physisorption studies, respectively. Pyridine adsorption is measured using an ultra-sensitive mass-balance approach called quartz crystal microbalance (QCM). Finally, the effect of crystallinity of the nanoPPX (modified by annealing) on the pyridine adsorption and subsequent metallization is evaluated.

Chapter 5 discusses two applications of these hybrid nanostructures in detail: 1. Co/nanoPPX as catalyst and 2. Ag/nanoPPX as SERS platform. Co/nanoPPX catalysts prepared using noncovalent functionalization route show excellent catalytic activity for hydrogen production from alkaline-stabilized NaBH₄ solution. Improvement in the catalyst stability and activity is achieved by varying the porosity at the metal and/or the nanoPPX deposition stages. SERS activity of Ag/nanoPPX films is studied using 4-

fluorobenzenethiol (FBT) as the probe analyte. A metal growth model correlating the observed variation in the SERS enhancement with the metal morphology is proposed. Further, these SERS platforms are employed for RSV gene detection using fluorescent molecular probes. In addition to these two applications, a preliminary study demonstrating the potential of TiO₂/nanoPPX films as orthopaedic implant coatings is also discussed in this chapter.

Chapter 6 summarizes the thesis and suggests directions for future work.

1.4. Representative Publications

1. Cetinkaya, M., Malvadkar, N. & Demirel, M. C. Power-law scaling of structured poly(p-xylylene) deposited by oblique angle. *Journal of Polymer Science Part B-Polymer Physics* **46**, 640-648 (2008).
2. Malvadkar, N. A., Sekeroglu, K., Dressick, W. J. & Demirel, M. C. Noncovalent Mechanism for the Conformal Metallization of Nanostructured Parylene Films. *Langmuir* **26**, 4382-4391 (2010).
3. Malvadkar, N., Dressick, W. J. & Demirel, M. C. Liquid phase deposition of titania onto nanostructured poly-p-xylylene thin films. *Journal of Materials Chemistry* **19**, 4796-4804 (2009).
4. Malvadkar, N., Park, S., Urquidi-MacDonald, M., Wang, H. & Demirel, M. C. Catalytic activity of cobalt deposited on nanostructured poly(p-xylylene) films. *Journal of Power Sources* **182**, 323-328 (2008).

5. Kao, P., Malvadkar, N., Cetinkaya, M., Wang, H., Allara, D. L. & Demirel, M. C. Surface-enhanced Raman detection on metalized nanostructured poly(p-xylylene) films. *Advanced Materials* **20**, 3562-3565 (2008).

References

1. Lowenheim, F. A. *Modern electroplating* (John Wiley & Sons, New York, 1974).
2. Mallory, G. O. *Electroless Plating: Fundamentals & Applications* (American Electroplaters and Surface Finisher's Society, Orlando, FL, 1990).
3. Gavrilov, G. G. *Chemical (electroless) nickel-plating* (Portcullis Press, 1979).
4. Duffy, J. I. *Electroless and other nonelectrolytic plating techniques: recent developments* (Noyes Data Corp, Park Ridge, NJ, 1980).
5. Zabetakis, D. & Dressick, W. J. *ACS Applied Materials & Interfaces* **1**, 4-25 (2009).
6. Cheng, K. et al. *Macromolecular Rapid Communications* **26**, 247-264 (2005).
7. Wu, S. Y., Kang, E. T., Neoh, K. G. & Tan, K. L. *Langmuir* **16**, 5192-5198 (2000).
8. Shafeev, G. A., Themlin, J. M., Bellard, L., Marine, W. & Cros, A. *Journal of Vacuum Science & Technology a-Vacuum Surfaces and Films* **14**, 319-326 (1996).
9. Sacher, E. *Progress in Surface Science* **47**, 273-300 (1994).
10. Shachamdiamand, Y., Dubin, V. & Angyal, M. *Thin Solid Films* **262**, 93-103 (1995).
11. Gray, J. E., Norton, P. R. & Griffiths, K. *Thin Solid Films* **484**, 196-207 (2005).
12. Sipaut, C. S., Ibrahim, M. N. M. & Izat, M. E. *Journal of Applied Polymer Science* **103**, 1554-1565 (2007).

13. Malvadkar, N., Park, S., Urquidi-MacDonald, M., Wang, H. & Demirel, M. C. *Journal of Power Sources* **182**, 323-328 (2008).
14. McCaskie, J. & Redding, S. *Metal Finishing* **106**, 25-27 (2008).
15. Zhao, Q., Wang, C., Liu, Y. & Wang, S. *International Journal of Adhesion and Adhesives* **27**, 85-91 (2007).
16. Mittal, K. L. *Journal of Vacuum Science & Technology* **13**, 19-25 (1976).
17. Wu, S. Y., Kang, E. T., Neoh, K. G., Han, H. S. & Tan, K. L. *Macromolecules* **32**, 186-193 (1999).
18. Bou, M., Martin, J. M. & Lemogne, T. *Applied Surface Science* **47**, 149-161 (1991).
19. Charbonnier, M., Romand, M., Esrom, H. & Seebock, R. *Journal of Adhesion* **75**, 381-404 (2001).
20. Beil, S., Horn, H., Windisch, A., Hilgers, C. & Pochner, K. *Surface & Coatings Technology* **116**, 1195-1203 (1999).
21. Weichenhain, R., Wesner, D. A., Pfleging, W., Horn, H. & Kreutz, E. W. *Applied Surface Science* **110**, 264-269 (1997).
22. Niino, H. & Yabe, A. *Applied Surface Science* **69**, 1-6 (1993).
23. Charbonnier, M., Romand, M., Harry, E. & Alami, M. *Journal of Applied Electrochemistry* **31**, 57-63 (2001).
24. Kang, E. T. & Zhang, Y. *Advanced Materials* **12**, 1481-1494 (2000).
25. Yu, W. X., Hong, L., Chen, B. H. & Ko, T. M. *Journal of Materials Chemistry* **13**, 818-824 (2003).

26. Horn, H., Beil, S., Wesner, D. A., Weichenhain, R. & Kreutz, E. W. *Nuclear Instruments & Methods in Physics Research Section B-Beam Interactions with Materials and Atoms* **151**, 279-284 (1999).
27. Zaporojtchenko, V., Zekonyte, J. & Faupel, F. *Nuclear Instruments & Methods in Physics Research Section B-Beam Interactions with Materials and Atoms* **265**, 139-145 (2007).
28. Siau, S., Vervaeet, A., Van Calster, A., Swennen, I. & Schacht, E. *Journal of the Electrochemical Society* **151**, J54-J61 (2004).
29. Ge, J., Turunen, M. P. K. & Kivilahti, J. K. *Journal of Polymer Science Part B-Polymer Physics* **41**, 623-636 (2003).
30. Vorobyova, T. N. *Journal of Adhesion Science and Technology* **11**, 167-182 (1997).
31. Saraf, R. F., Roldan, J. M. & Derderian, T. *Ibm Journal of Research and Development* **38**, 441-456 (1994).
32. Chung, C. K. et al. *Sensors and Actuators B-Chemical* **117**, 367-375 (2006).
33. Vaeth, K. M. & Jensen, K. F. *Chemistry of Materials* **12**, 1305-1313 (2000).
34. Cohen, R. L. & West, K. W. *Journal of the Electrochemical Society* **120**, 502-508 (1973).
35. Holderer, O., Epicier, T., Esnouf, C. & Fuchs, G. *Journal of Physical Chemistry B* **107**, 1723-1726 (2003).
36. Cohen, R. L. & West, K. W. *Journal of the Electrochemical Society* **119**, 433-438 (1972).
37. Zehner, R. W. & Sita, L. R. *Langmuir* **15**, 6139-6141 (1999).

38. Wang, T. C., Chen, B., Rubner, M. F. & Cohen, R. E. *Langmuir* **17**, 6610-6615 (2001).
39. Goren, M., Qi, Z. G. & Lennox, R. B. *Chemistry of Materials* **12**, 1222-1228 (2000).
40. Blackburn, J. M., Long, D. P., Cabanas, A. & Watkins, J. J. *Science* **294**, 141-145 (2001).
41. Kundt, A. *Annalen der Physik und Chemie* **263**, 59-71 (1886).
42. Smith, D. O. *Journal of Applied Physics* **30**, S264-S265 (1959).
43. Knorr, T. G. & Hoffman, R. W. *Physical Review* **113**, 1039-1046 (1959).
44. Holland, L. *Journal of the Optical Society of America* **43**, 376-380 (1953).
45. He, Y. & Zhao, Y. *Crystal Growth & Design* **10**, 440-448 (2009).
46. Wolcott, A., Smith, W. A., Kuykendall, T. R., Zhao, Y. & Zhang, J. Z. *Small* **5**, 104-111 (2009).
47. Ma, Y. et al. *Nanotechnology* **20** (2009).
48. Zheng, Y., Bekele, R., Ouyang, J. & Xue, J. *Organic Electronics* **10**, 1621-1625 (2009).
49. Pursel, S., Horn, M. W., Demirel, M. C. & Lakhtakia, A. *Polymer* **46**, 9544-9548 (2005).
50. Cetinkaya, M. in *Synthesis and Characterization of Nanostructured Poly(p-xylylene) Films* (Doctoral Dissertation, Pennsylvania State University, Engineering Science and Mechanics, University Park, 2008).
51. Williams, D. H., Stephens, E., O'Brien, D. P. & Zhou, M. *Angewandte Chemie-International Edition* **43**, 6596-6616 (2004).

52. Chen, R. J. et al. *Proceedings of the National Academy of Sciences of the United States of America* **100**, 4984-4989 (2003).
53. Kim, J. B., Premkumar, T., Lee, K. & Geckeler, K. E. *Macromolecular Rapid Communications* **28**, 276-280 (2007).
54. Bradley, K., Briman, M., Star, A. & Gruner, G. *Nano Letters* **4**, 253-256 (2004).
55. Dressick, W. J., Chen, M. S. & Brandow, S. L. *Journal of the American Chemical Society* **122**, 982-983 (2000).
56. Chen, M. S., Brandow, S. L., Schull, T. L., Chrisey, D. B. & Dressick, W. J. *Advanced Functional Materials* **15**, 1364-1375 (2005).
57. Dressick, W. J. et al. *Applied Physics Letters* **78**, 676-678 (2001).
58. Chen, M.-S., Dressick, W. J., Schull, T. L. & Brandow, S. L. in *Nanostructure Science, Metrology, and Technology* (eds. Peckerar, M. C. & Postek, M. T.) 155-159 (SPIE, 2002).
59. Dressick, W. J., Nealey, P. F. & Brandow, S. L. in *Emerging Lithographic Technologies V* (ed. Dobisz, E. A.) 294-305 (SPIE, 2001).
60. Brandow, S. L., Chen, M. S., Dulcey, C. S. & Dressick, W. J. *Langmuir* **24**, 3888-3896 (2008).
61. Demirel, M. C., Cetinkaya, M., Singh, A. & Dressick, W. J. *Advanced Materials* **19**, 4495-4499 (2007).

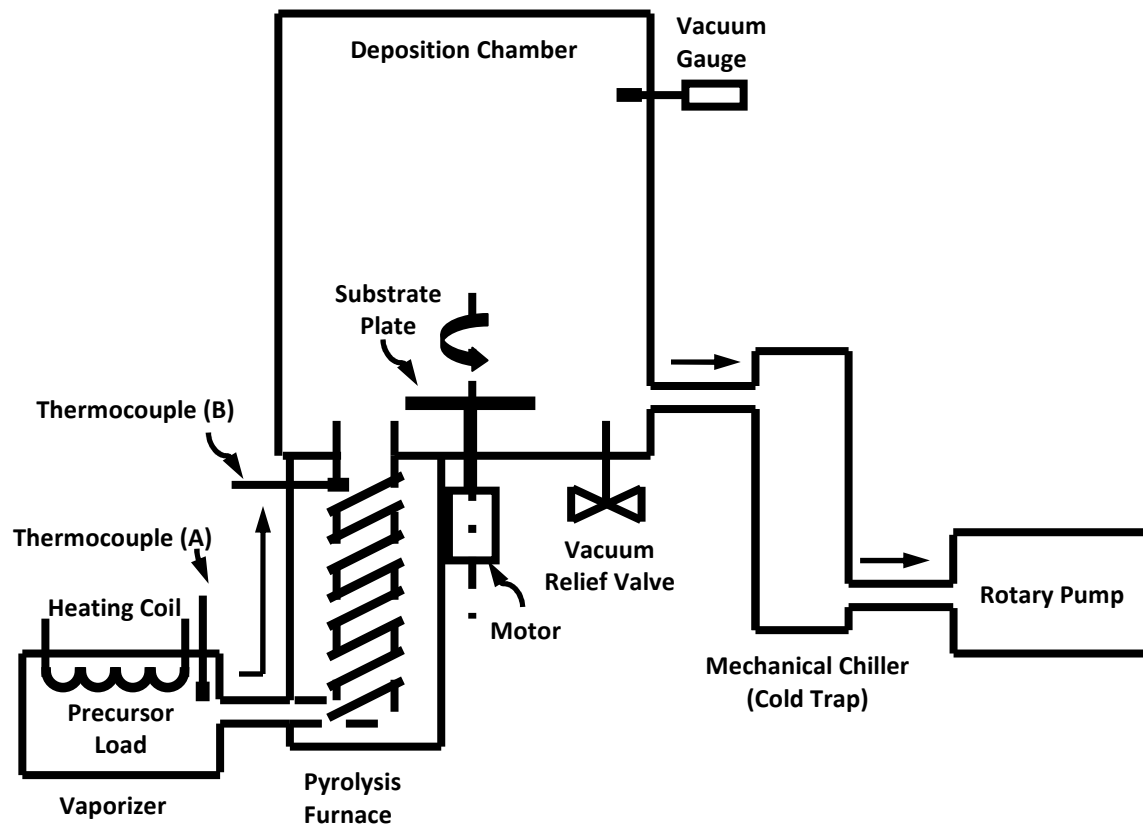
Chapter 2. Metal/NanoPPX Hybrid Nanostructures*

2.1. NanoPPX

2.1.1. NanoPPX Deposition

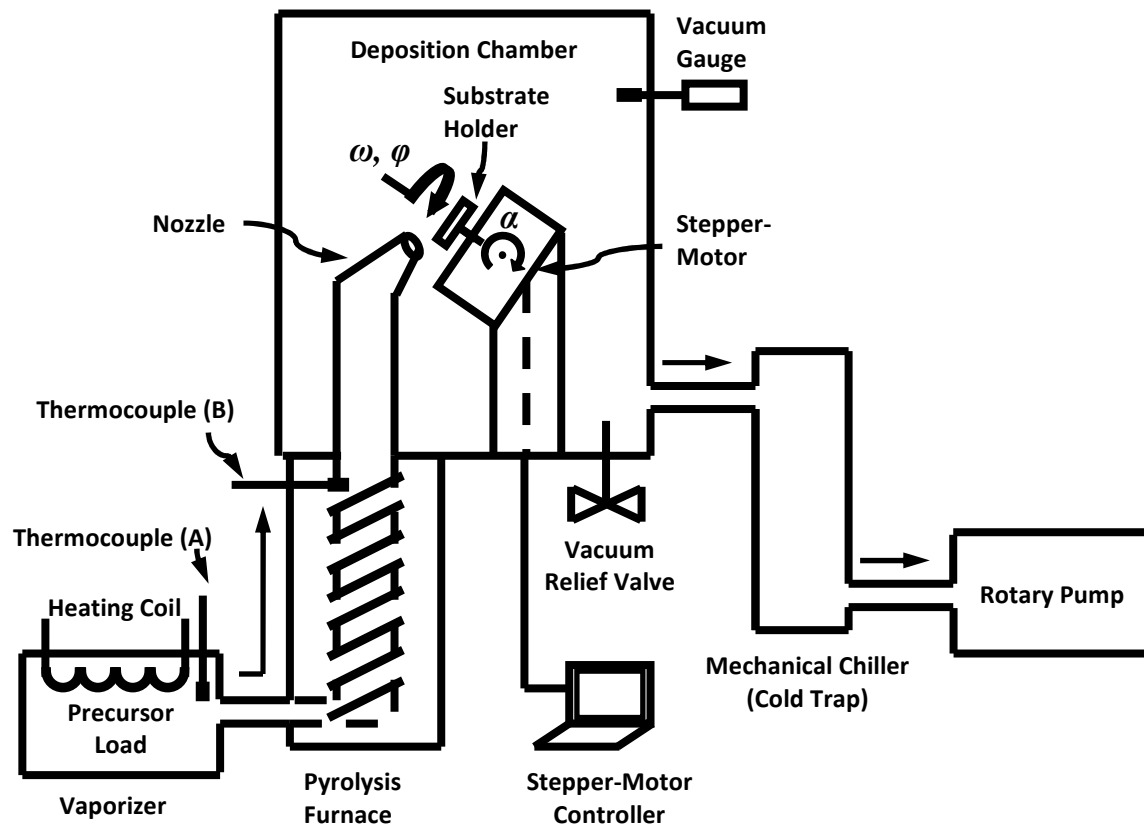
Scheme 2-1 shows the schematic of an unmodified Labcoter™ 2 (PDS2010, SCS Inc., IN) deposition unit, which can deposit conventional PPX films that are devoid of any distinct morphologically features. The deposition unit consists of three sections: (i). a vaporizer, (ii). a pyrolysis furnace and (iii). a deposition chamber. Substrates are kept inside the deposition chamber on a horizontal plate affixed to a motor shaft that allows rotation for uniform film deposition. The PPX precursor is loaded in the vaporizer equipped with a heating coil that allows temperature in the vaporizer to reach as maximum of 200 °C. This temperature facilitates sublimation of the precursor and subsequent transportation of the precursor vapors into the pyrolysis chamber. The pyrolysis chamber is a ~30 cm long tube furnace and can reach a maximum temperature of ~700 °C, enough for the formation of monomeric radical from the precursor vapors. A detailed chemical process involved in the conversion of the precursor to the PPX film is presented in Section 2.1.2.

* Some contents of this chapter are reproduced in part with permission from Malvadkar *et al.*, *Langmuir* **26**, 4382–4391 (2010). DOI: 10.1021/la9034529. Copyright 2010 American Chemical Society.



Scheme 2-1. Schematic of an unmodified version of a Labcoter™ 2 system used for depositing planar PPX films.

For nanoPPX deposition, modifications were made in the deposition chamber to incorporate OAP during PPX film growth, as shown in Scheme 2-2. The modifications include a nozzle with a 45° bend installed at the outlet of the tube furnace and a substrate holder connected to a stepper motor allowing axial rotation (ω) and an angular motion (α) to vary the direction of the incidence flux. The resulting film (nanoPPX) has a unique nanorod morphology (see Section 2.1.3 for details) with the same chemistry as that of a planar film.



Scheme 2-2. Schematic of the modified (OAP) version of Labcoter™ 2 system used for depositing nanoPPX films.

For planar PPX or nanoPPX deposition, the following steps are followed in the order presented:

1. The vaporizer is loaded with PPX precursor. The substrate is affixed on the substrate holder. α and ω values are adjusted using the stepper-motor controller (in the modified version).
2. The vaporizer, pyrolysis furnace, and the deposition chamber are evacuated to a pressure less than 25 mtorr.
3. The pyrolysis furnace is preheated to 690 °C and the cold trap is pre-cooled to less than -90 °C.

4. The vaporizer is slowly heated to 175 °C. The vaporizer power switch also powers the shaft motor for planar deposition.
5. PPX film is allowed to deposit on the substrate for 10 min after vaporizer reaches 175 °C.
6. Power to vaporizer and pyrolysis furnace is turned off.
7. When the pyrolysis furnace is cooled to less than 300 °C, the complete system can be brought to atmospheric pressure *via* a vacuum relief valve.

In actuality, steps 3 to 6 are automated in the LabcoaterTM-II deposition unit through appropriate set points for vaporizer temperature, pyrolysis furnace temperature and the deposition chamber pressure. 0.3 g and 3.64 g of the precursor, corresponding to ~7 μm film thickness, is used to deposit nanoPPX and planar PPX, respectively, for all studies reported in this thesis (unless otherwise specified). Values for α and ω are 10° and 5 rpm (for helical morphology only), unless otherwise specified.

2.1.2. Chemistry of PPX Formation

Due to the inherent hydrophobic nature of PPX films, adhesion of a PPX film to silicon substrate requires modification of the silicon surface using an allyltrimethoxysilane self assembled monolayer (SAM). The allyl group ($\text{H}_2\text{C}=\text{CH}-\text{CH}_2-$) chemically binds with the PPX film. It should be noted that a PPX film can also grow on unmodified silicon substrate; however, due to the absence of any covalent bonding to the substrate and the hydrophobic nature of the polymer, the PPX films can easily delaminate in solvents such as water and ethanol. Since our work involves treating the films with aqueous solutions, it is necessary to establish good

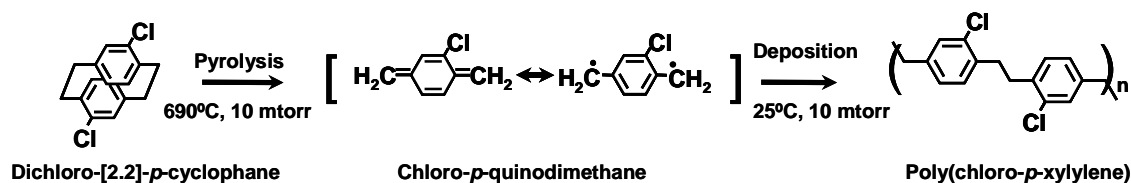
bonding between the PPX and the silicon substrate, which is achieved through the covalent binding of the PPX with the SAM.

To prepare allyl-functionalized silicon substrates, native oxide *p*-type Si (100) wafers are first sonicated in acetone, rinsed in water and dried using nitrogen gas to remove any physisorbed contaminants. Later, the wafers are transferred to 1/1 (v/v) solution of hydrochloric acid and anhydrous methanol. After 30 min. the wafers are removed, rinsed thoroughly in water, dried using nitrogen gas, and kept in sulfuric acid for another 30 min. Wafers are then removed and thoroughly washed in copious amounts of water and dried under nitrogen gas. Wafers are then transferred to an allyltrimethoxysilane self-assembled monolayer (SAM) solution that is prepared by adding 1% (v/v) allyltrimethoxysilane (Gelest, PA) in toluene containing 0.1% (v/v) acetic acid. The cleaned wafers are left in the SAM solution for 60 min. at 25 °C. The wafers are removed after 60 min. and sonicated in anhydrous toluene for 10 min. The wafers are then dried on a hot plate at 140 °C for 5 min to remove solvent and complete the chemisorption process. SAM treated silicon wafers are stored in a dark environment at 5 °C until needed for PPX deposition.

The chemistry of vapor-phase PPX film growth, developed by William F. Gorham in 1966,¹ is same under both deposition modes (*i.e.*, conventional and OAP). Gorham discovered that a stable dimer of the highly reactive *p*-xylylene molecule, di-*p*-xylylene or [2.2] *p*-cyclophane, can be pyrolyzed at temperatures greater than 550 °C and pressure less than 1 torr yielding two units of *p*-xylylene. The monomeric unit polymerizes spontaneously on a surface kept at relatively low temperatures, resulting in the formation of high molecular weight poly(*p*-xylylene) film. Similar chemistry applies

to derivatives of [2.2] *p*-cyclophane, including dichloro-[2.2]-*p*-cyclophane (DCPC) and dibromo-[2.2]-*p*-cyclophane (DBPC), among others.

A schematic of the chemistry involved during PPX formation in a modern parylene coating system, such as the Labcoater™-II, is shown in Scheme 2-3. The solid dimer, DCPC, is first sublimed at 175 °C in the vaporizer. Subsequently, pyrolysis of DCPC at 690 °C cleaves the methylene-methylene bridge bonds yielding monomeric chloro-*p*-quinodimethane (or chloro-*p*-xylylene) \leftrightarrow diradical. Upon reaching a low temperature (\sim 25 °C) surface, the highly reactive chloro-*p*-quinodimethane diradicals quickly polymerizes *via* radical-radical coupling resulting in the formation of a continuous poly(chloro-*p*-xylylene) film. The entire assembly is maintained at \sim 10 mtorr using a rotary pump throughout the deposition process.



Scheme 2-3. Vapor phase deposition of poly(chloro-*p*-xylylene) (PPX) from dichloro-[2.2]-*p*-cyclophane (DCPC) *via* Gorham's method.

2.1.3. Mechanism of NanoPPX formation

OAP induces a directional constraint (*i.e.*, incidence angle, $\alpha \ll 90^\circ$) to the diradical flux resulting in porous and low-density PPX film consisting of nanorods that are tilted away from the substrate normal.² In a conventional deposition (in an

unmodified LabcoaterTM-II unit), the absence of any directionality of the diradical flux results in a “planar” film that is devoid of any nanostructure.

The initial stage of growth of a planar and nanoPPX film is similar: a thin layer (~1–5 nm RMS roughness) of PPX is formed due to the high surface diffusion of the monomeric diradicals and/or PPX-oligomers on the substrate.³ Although this thin layer of PPX is devoid of any structure, it shows surface instabilities that act as nucleation sites for the subsequent growth of the PPX nanorods. The growth of a nanoPPX film is controlled by two opposing mechanisms: the self-shadowing effect and surface diffusion of adparticles. While the self-shadowing effect⁴ is entirely a physical phenomenon occurring due to the directional constraint of the monomeric radical flux and responsible for the oriented anisotropic growth of the PPX nanorods, surface diffusion of adparticles, on the other hand, is dependent on the temperature and the surface chemistry of the material deposited and the substrate and induces a “smoothing” effect on the film growth. The nanostructured morphology can therefore be tuned by controlling the deposition parameters³ and/or the functional groups² on PPX.

Figures 2-1 (A–D) show the FESEM (JEOL 6700F, 3 kV operating voltage) images of the various cross-section morphologies of PPX prepared by modifying the deposition parameters. To keep the morphology of the film intact, all FESEM samples were immersed in liquid nitrogen for 30 min prior to cleaving. In the conventional deposition mode, the resultant film does not possess any nanostructured morphology (Figure 2-1A) due to the absence of self-shadowing effect (*i.e.*, normal deposition, $\alpha = 90^\circ$). In the OAP mode, the final morphology consists of obliquely aligned PPX nanorods on the substrate with a density of approximately $\sim 40 \times 10^6$ nanorods/mm² (Figure 2-1B).²

The column inclination angle (β) depends on the side-group chemistry of the PPX and the angle of incidence of the monomer flux (α).² Helical morphologies (Figure 2-1D) can be prepared by introducing unidirectional substrate rotation (*i.e.*, $\omega > 0$), in addition to inclined diradical flux. If the substrate is rotated in both directions (*i.e.*, clockwise and counterclockwise) along a certain azimuthal sweep angle (φ), the resulting morphologies is known as chevrons (Figure 2-1C). Other hybrid nano-morphologies can be prepared by applying a combination of deposition parameters, including α , ω , φ and t_p (pause time between clockwise and counterclockwise rotation).

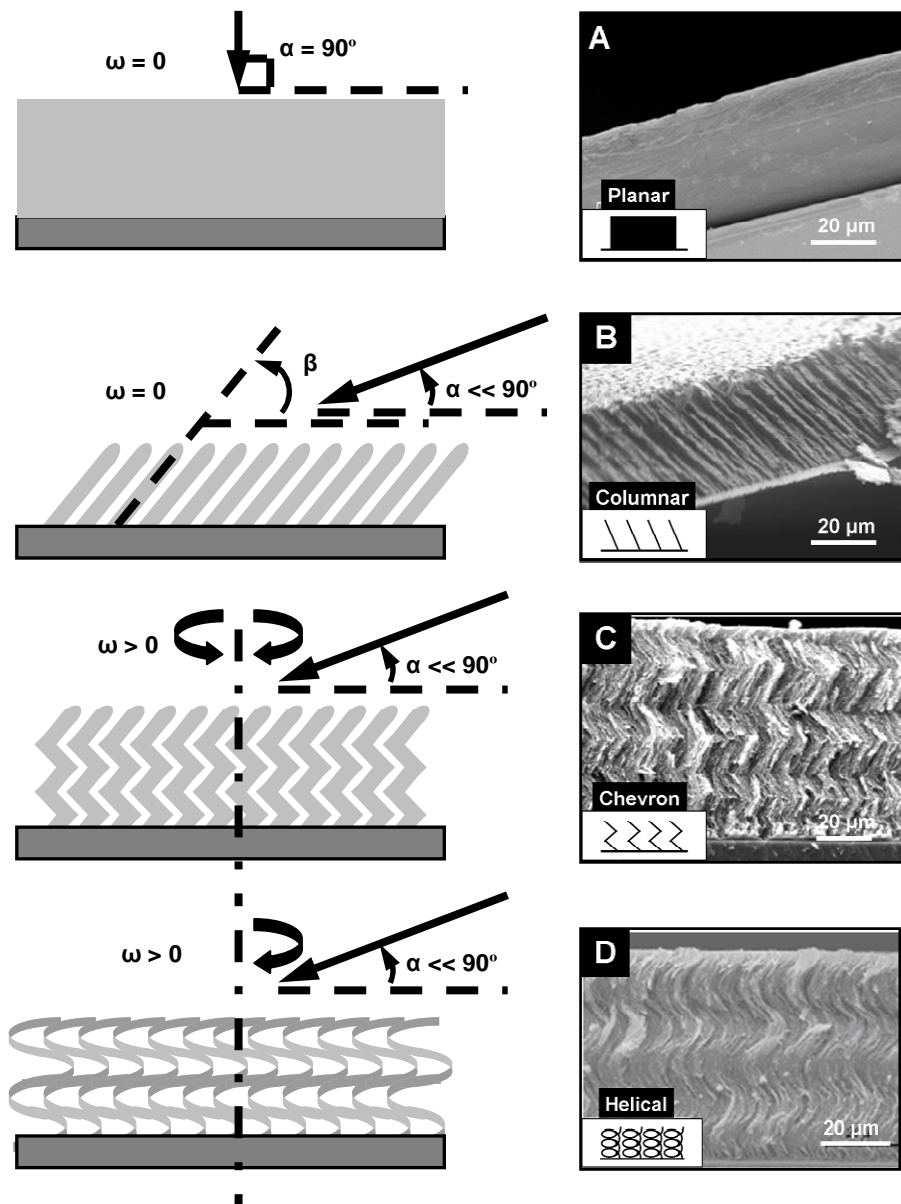


Figure 2-1. Effect of variation of deposition parameters, namely, the incidence flux angle (α) and the axial substrate rotation speed (ω) on the cross-sectional morphology of PPX film. Left images show the cartoon and right images show the corresponding cross-sectional SEM image. (A) Planar film ($\alpha = 90^\circ$, $\omega = 0$); (B) Columnar nanoPPX film ($\alpha \ll 90^\circ$, $\omega = 0$); (C) Chevron nanoPPX film ($\alpha \ll 90^\circ$, $\omega = \pm 5$ rpm, $\varphi = 30^\circ$); (D) Helical nanoPPX film ($\alpha \ll 90^\circ$, $\omega = 5$ rpm). SEM images are reprinted from *Colloids Surf., A* 321, 121–124, Copyright 2008 with permission from Elsevier.

2.1.4. Physicochemical Properties of NanoPPX

A detailed discussion on the various physicochemical properties of nanoPPX film, including surface energy, morphology, and column size, is presented in Murat Cetinkaya's doctoral thesis.⁵ Herein, we summarize some of the important physicochemical properties relevant to the formation of metallized nanoPPX hybrid nanostructures.

The growth of a columnar nanoPPX film follows a power-law scaling, *i.e.*, the size or the diameter of individual nanorods is a power function of the height of the column.³ Mathematically, this can be expressed as:

$$d = ch^p \quad (2-1)$$

where, d is the diameter and h is the height of the column. This implies that the column size and spatial distribution can be controlled by simply varying the thickness of the nanoPPX film. The single exponent, p , signifying isotropic growth of columns and the multiplying factor, c depends on the deposition parameters and the side-group chemistry of PPX. For example, the exponent, p , values of poly(chloro-*p*-xylylene), poly(bromo-*p*-xylylene), and poly(trifluoroacetyl-*p*-xylylene-co-*p*-xylylene) for a 10° deposition angle are estimated to be 0.11 ± 0.01 , 0.18 ± 0.01 , and 0.15 ± 0.01 , respectively.² A smaller exponent for PPX film implies that the columns grow quicker than for the other two films. It is observed that the power law is followed only till a critical thickness is reached h_c after which the column size remains constant as the deposition continues. Besides the side-group chemistry, column size can be modified by varying growth parameters, such as ω , as listed in Table 2-1.

Table 2-1. Influence of morphology of PPX film on various physicochemical properties.

PPX Morphology	Column Size (nm) ^a	RMS Roughness (nm) ^a	BET Surface Area (m ² g ⁻¹ μm ⁻¹) ^b	Contact Angle (degree) ^a
Planar	—	7.9 ± 0.8 ²	0.3757	87 ± 2 ⁵
Columnar	131 ± 18	46.3 ± 5.0 ²	1.9855 ^c	119 ± 1 ⁵
Helical	115 ± 13	44.8 ± 4.1	2.0948	124 ± 5

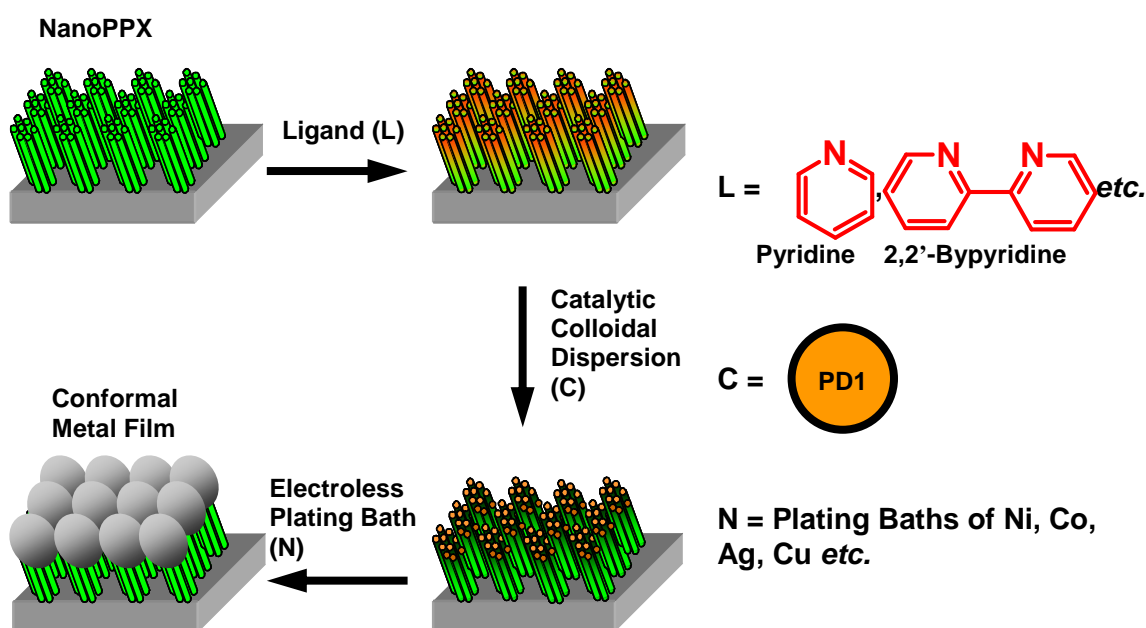
^a Values represent mean ± one standard deviation. ^b BET surface area is normalized with film thickness (in μm). ^c BET value was obtained from QCM-monitored N₂ adsorption per the procedure detailed in Kao *et al.*⁶

Surface topography was characterized by an atomic force microscope (AFM, Nanoscope[®] E, Veeco Inc.) using silicon nitride cantilevers (Veeco Metrology, CA) in contact mode. RMS roughness was recorded for 3–6 random area scans (5 μm × 5 μm) on each sample. The “Flatten” command in Nanoscope[®] was used before recording the RMS roughness to remove any effect due to large-scale surface corrugations on the sample. RMS Roughness data show that nanoPPX films prepared by OAP are profoundly rougher than the planar counterpart. The fibrous morphology exhibited by nanoPPX films also influence the BET surface area (Table 2-1), obtained from Micrometrics ASAP 2020 (see Chapter 4 for details). Introduction of periodic surface roughness has shown to enhance the sessile water contact angle of hydrophobic surfaces.⁷ Therefore, it is not surprising to see higher water contact angles on nanoPPX films compared to a planar PPX film (Table 2-1).

2.2. Preparation of Metal/NanoPPX Hybrid Nanostructures

In Sections 2.1.3 and 2.1.4, we discussed an OAP-based approach to prepare various controllable nano-morphologies of PPX by engineering different deposition

parameters. However, practical application of these nano-morphologies entails functionalization of its surface with metals, alloys, ceramics, and other polymers. In the concept paper (Demirel *et al.*), one such functionalization strategy, based on a noncovalent approach, was used to deposit porous Ni layer on nanoPPX.⁸ Herein, we describe a generalized method (depicted in Scheme 2-4) to deposit metal nanoparticles/membranes onto the nanoPPX films. The scheme consists of the following three steps described below.



Scheme 2-4. Schematic of the formation of conformal metal film on nanoPPX *via* the noncovalent electroless metallization process.

2.2.1. Noncovalent Ligand Functionalization

As a first step of metal deposition, nanoPPX films are treated with an aromatic ligand, typically pyridine, by means of either aqueous solution or vapor treatment. For

aqueous pyridine treatment, the PPX films are soaked in 1 M pyridine (aq) solution held in a tightly sealed vial for 30 or 48 h. The films are rinsed in water and then transferred to the Pd(II) based colloidal dispersion for surface catalysis. For vapor phase pyridine treatment, the PPX samples are suspended in a sealed vial with a few drops of pyridine (not contacting the samples). The vials are maintained at a temperature of 110 °C (pyridine *b.p.* = 115.2 °C) in an oil bath for ~48 h (unless specified otherwise). Unlike aqueous pyridine treated PPX films, vapor pyridine treated PPX films are directly transferred to the Pd(II) based colloidal dispersion after removing from the vials. Similar functionalization procedure (both, aqueous and vapor routes) could be carried out using other aromatic ligands such as thiophenol, catechol, phenylphosphonic acid *etc.*

2.2.2. Surface Catalyzation

PD1, a Pd(II) based catalyst system, is prepared as described in the literature.⁹ Briefly, 11.5 mg of $\text{Na}_2\text{PdCl}_4 \cdot 3\text{H}_2\text{O}$ is completely dissolved in 1 mL of 1.00 M NaCl (aq), followed by addition of 10 mL of pH 5, 0.10 M 2-(*N*-morpholino)ethanesulfonic acid (MES) buffer. The resulting solution is diluted to 100 mL by addition of water. This solution is incubated at 25 ± 0.1 °C in a temperature controlled water bath for 20 h, after which 10 mL aliquot was removed and replaced with 10 mL of the 1.00 M NaCl (aq) solution. The resultant PD1 catalyst dispersion is stable for up to at least one month in the water bath held at 25 ± 0.1 °C. NanoPPX films treated with pyridine are kept in the colloidal dispersion for 45 min (unless specified otherwise), after which they are gently rinsed in water for 5–10 s, dried in nitrogen gas, and immediately transferred to the metallization bath.

2.2.3. Electroless Metal Plating

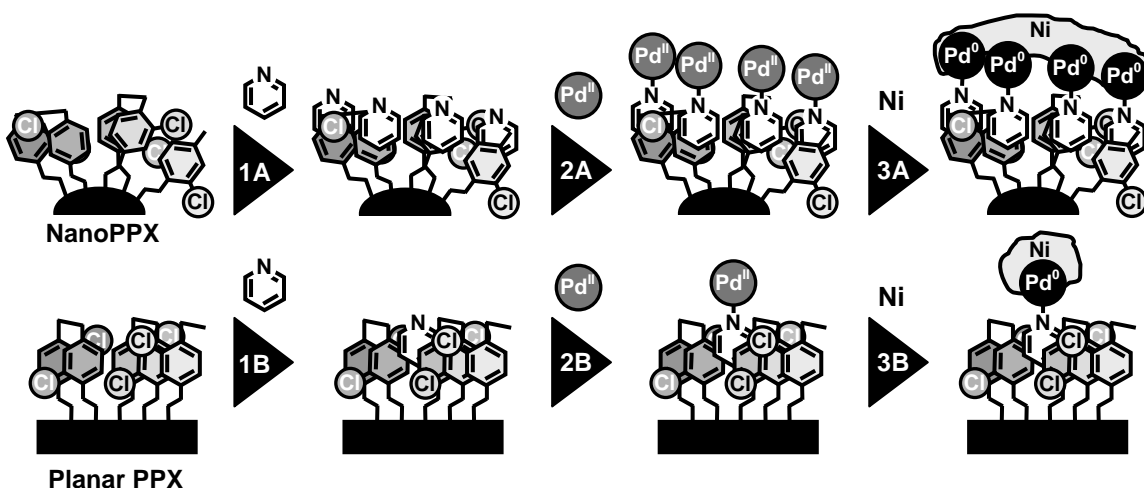
After PD1 catalyzation, the nanoPPX films are immersed in electroless plating bath. For Ni metallization, the stock solution of NIPOSIT™ 468B (prepared according to manufacturer's instructions) is diluted to 10% of the original concentration by addition of water. During Ni deposition the samples are gently agitated to remove any adhered hydrogen gas bubbles on the surface. Metal deposition is carried out for 5 to 60 min (as specified) at 25 °C, after which the films were rinsed in water, dried under nitrogen gas, and stored in Fluoroware® containers until they are used for characterization. Similar plating procedure can be carried for Co or Ag metallization using appropriate plating baths, as described in Chapter 5.

2.3. Preliminary Metal Growth Model

The concept paper (Demirel *et al.*)⁸ describes a preliminary metal growth model, summarized here, correlating the observed metallization to the ability of the nanoPPX surface to bind pyridine molecules. Electroless deposition of metal onto polymer surfaces usually requires prior treatment of the surface with a catalyst, which is often a colloidal Pd species.¹⁰ One such species, PD1,⁹ is a Pd(II) based colloid formed by the controlled hydrolysis of PdCl_4^{2-} species in aqueous solution. As a first step in our process we physisorb a π -acceptor ligand, such as pyridine, onto the surface of the nanoPPX polymer. Subsequently, PD1 binds covalently and selectively to the N-site of the pyridine molecule in both the Pd(II) state (*via* σ -bonding) and the catalytically active Pd(0) state

(*via* π -back-bonding) formed by reduction in an electroless plating bath.¹⁰⁻¹³ Covalent binding of the catalyst increases the adhesion strength of the deposited electroless metal and improves selectivity of the deposition compared to use of conventional Pd/Sn catalysts.¹⁰

For pyridine impregnation in the nanoPPX film, we adopted two methods: the direct vapor method and partitioning from aqueous solution. In the first method, nanoPPX films are held in a chamber containing pyridine vapor, which adsorbs into the outermost layers of the nanostructured polymer film. In the second method, nanoPPX films are soaked in aqueous pyridine solution to allow partition of the solvated pyridine molecules in the aqueous solution into the polymer. Due to the noncovalent nature of the adsorption interaction, the chemistry and favorable physicochemical properties of the nanoPPX polymer remain unaltered.



Scheme 2-5. Surface effects model for metallization of poly(chloro-*p*-xylylene) (PPX) films. Path A: nanostructured PPX films (nanoPPX). Path B: planar PPX film. Reproduced with permission from Malvadkar *et al.*, *Langmuir* **26**, 4382–4391 (2010).

DOI: 10.1021/la9034529. Copyright 2010 American Chemical Society.¹⁴

Scheme 2-5 illustrates our previously described model for pyridine physisorption, catalysis, and electroless metallization of nanoPPX films and planar PPX films.⁸ In this model, incorporation of pyridine in nanoPPX per path A, driven by the minimization of the free energy for stabilization, occurs *via* the formation of favorable π - π interactions with disordered aromatic groups comprising the polymer backbone at the largely amorphous surface regions of the PPX nanorods. Although π - π interactions are weak, an array of multiple interactions, combined with covalent binding of the Pd catalyst, can create significant interface strength. As a result, metallized nanoPPX films using the noncovalent route consistently pass the Scotch[®] tape adhesion test. Besides multiple noncovalent interactions, mechanical anchoring of the metal layer, due to the penetration of Ni into the spaces between the PPX nanorods, also contributes to the interface strength.⁸ While nanoPPX films exhibit excellent metallization (Figure 2-2A) with good interface strength, the conventionally deposited planar PPX films show no or poor metallization in a non-continuous or patchy nature (Figure 2-2B) per Scheme 2-5 (path B).^{15,39} The poor metallization has been attributed to lower levels of pyridine adsorption in conventionally deposited planar PPX films, which lack the high curvature surfaces that provide the disordered surface aromatic groups that facilitate pyridine incorporation in the nanoPPX films. Consequently, the lower concentration of pyridine molecules in planar PPX films simply cannot bind enough PD1 colloids to catalyze the Ni metallization.⁸

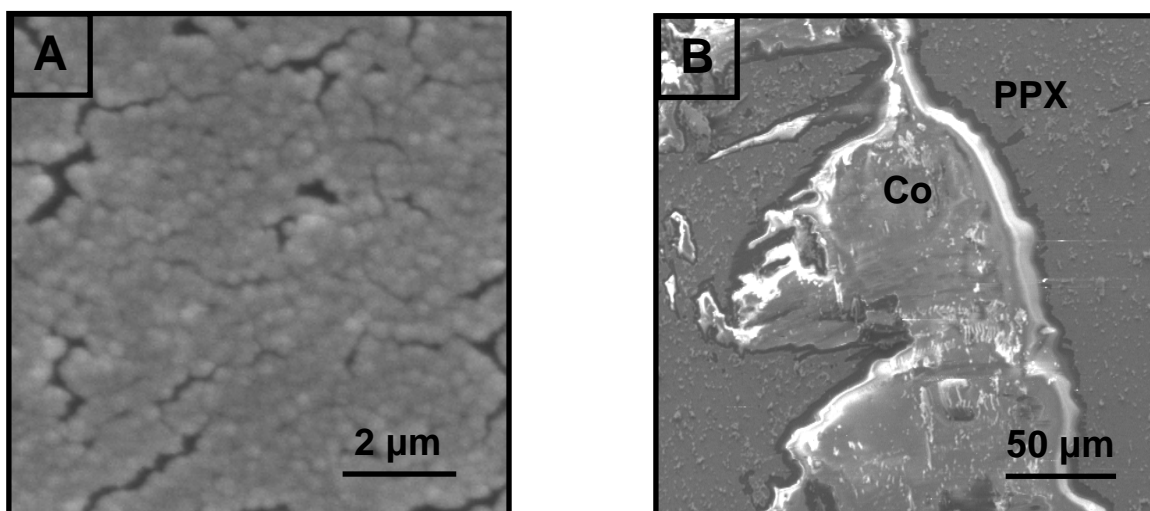


Figure 2-2. Co metallization on (A) nanoPPX and (B) planar PPX *via* noncovalent pyridine functionalization. Reprinted from *J. Power Sources* 182, 323–328, Copyright 2008 with permission from Elsevier.

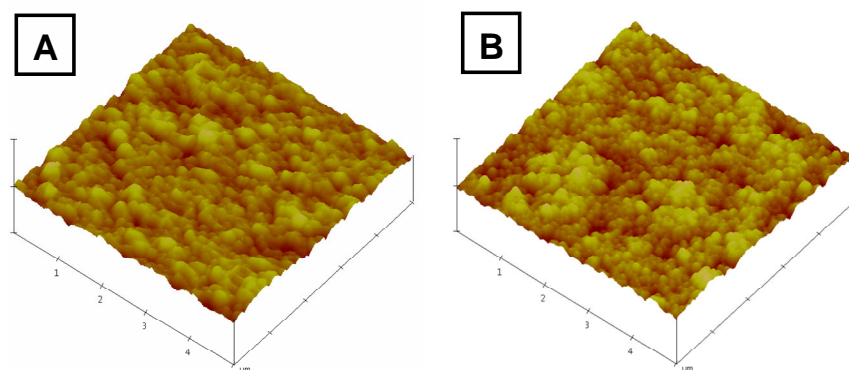


Figure 2-3. (A) Contact mode AFM image of pristine nanoPPX film. (B) Contact mode AFM image of Ni film deposited on nanoPPX functionalized using aqueous pyridine treatment. Metallization parameters used for preparing sample B – (i) Aqueous pyridine adsorption time: 48 h., (iii) PD1 treatment time: 45 min., (iv) Ni plating time: 60 min. For both AFM images the unit length in the x-y scale is 1 μm and the z scale unit is 800 nm. Reproduced with permission from Malvadkar *et al.*, *Langmuir* **26**, 4382–4391 (2010). DOI: 10.1021/la9034529. Copyright 2010 American Chemical Society.¹⁴

The AFM images of Figure 2-3 illustrate the conformal nature of metallization resulting in a metal layer that mimics the topology of the underlying polymer film. A SEM image (Figure 2-4) of the Ni film after Ga^+ focused ion beam (FIB) impingement shows a continuous Ni layer of thickness well under 100 nm (approximately 30 – 40 nm in thickness). Control samples of nanoPPX without ligand and/or PD1 treatment did not show any metallization, confirming that both ligand and PD1 treatments are necessary for metallization to occur.

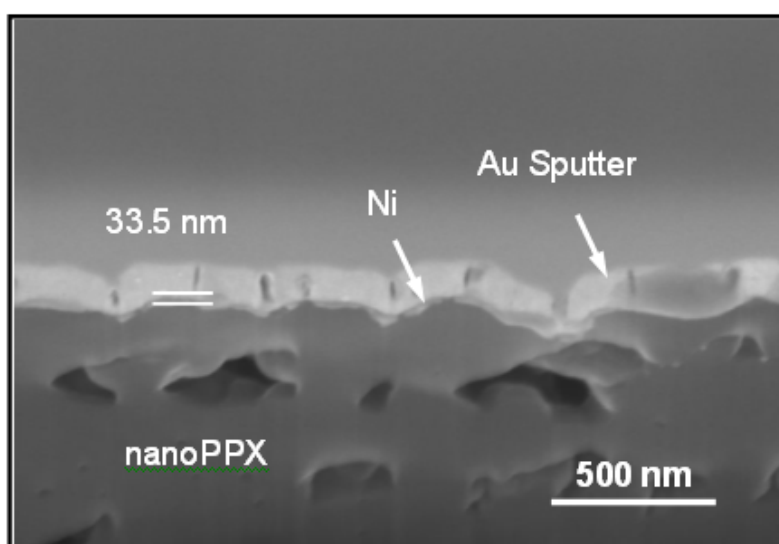


Figure 2-4. SEM image showing cross-section of the Ni/nanoPPX composite film etched using FIB. Metallization parameters used for preparing sample – (i) pyridine treatment condition: aqueous solution. (ii) pyridine adsorption time: 48 h., (iii) PD1 treatment time: 45 min., (iv) Ni plating time: 5 min. Reproduced with permission from Malvadkar *et al.*, *Langmuir* **26**, 4382–4391 (2010). DOI: 10.1021/la9034529. Copyright 2010 American Chemical Society.¹⁴

2.4. Chemical Analysis

XPS analyses provide further evidence supporting the growth model of Scheme 2-4 for the various chemical interactions in the system. To characterize the surface chemistry of the film after every chemical modification step, X-ray photoelectron spectroscopy (XPS) was performed using an Axis Ultra XPS system (Kratos) that uses a monochromatic Al K α X-ray source at 20 eV pass energy with a 700 $\mu\text{m} \times 300 \mu\text{m}$ hybrid sample spot size and 90° take-off angle. The sample chamber was maintained under ultra-high vacuum (10^{-9} torr). The C 1s peak at 284.6 eV was used as the reference to analyze all the collected spectra. The CasaXPS (version 2.3.14) software supplied by the manufacturer was used to analyze the data. The Pd 3d region was deconvoluted after a non-linear (Shirley-type) background subtraction and using a Gaussian / Lorentzian = 85/15 fit. To determine the photoelectric peak positions and concentrations, the following constraints were used: ratio of areas of Pd 3d_{5/2} : Pd 3d_{3/2} = 1.5; Binding energy difference: Pd 3d_{3/2} – Pd 3d_{5/2} = 5.25 eV; FWHM of all deconvoluted peaks within each spin orbit coupling doublet was held constant.

Figure 2-5 shows XPS spectra of N 1s region of nanoPPX film treated with 1 M pyridine (aq) solution for 40 h. A single peak at ~400 eV is observed, characteristic of the pyridyl-N chemical state. The XPS result establishes the noncovalent nature of the interactions between pyridine and PPX. The pyridine adsorption was quantified by XPS and quartz crystal microbalance (QCM) methods and the results are listed in Table 2-2. It is clear that pyridine adsorption increases with adsorption time. In addition, the XPS concentration, which is obtained from the top layer (~10 nm) of the polymer surface, show a smaller increase (*i.e.*, 0.53 to 0.61 at. %) from $t = 30$ min to $t = 40$ h compared to

the QCM concentration (67 to 109 nM/cm²), which represents the total amount of pyridine in the polymer. The above data suggests that pyridine infiltrates deeper into the PPX nanorods at longer adsorption times.

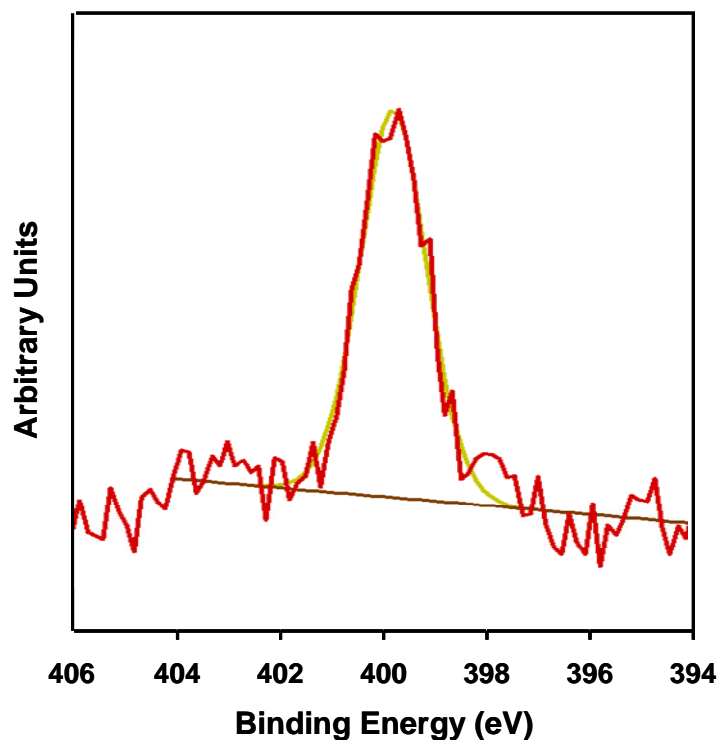


Figure 2-5. High resolution XPS spectra of N 1s region of aqueous pyridine-functionalized nanoPPX film. Pyridine concentration and adsorption time was 1 M and 40 h, respectively.

Table 2-2. Quantified metallization data.

Pyridine adsorption time ^a	Pyridine surface density in nanoPPX (nM/cm ²) ^b	N (at. %) ^c	Pd (at. %) ^d	Ni (at. %) ^e
0	0.00	—	0.43	—
30 min	67.12	0.51	0.72	0.28
40 h	106.83	0.63	2.48	5.90

^a 0.2 M aqueous pyridine treatment. ^b Estimated using a quartz crystal microbalance (QCM) and applying Sauerbrey's equation (see Chapter 4 for experimental details).¹⁶ ^c Obtained from samples after PD1 (30 min) treatment. ^d PD1 treatment time = 30 min. ^e 10% NIPOSIT™ bath time = 5 min (*cf.* Figures 2-7A–C).

Figure 2-6 shows the Pd 3d region of PD1 treated nanoPPX films under three different conditions. We used the Pd 3d_{5/2} signal to assign the chemical states of Pd in the sample. First, we treated nanoPPX films with PD1 catalyst for 30 min without any pre-treatment with pyridine ligand solution, then rinsed the films in H₂O and dried them under N₂ gas before examining them by XPS. After background subtraction, the Pd 3d_{5/2} region was deconvoluted to fit two peaks at binding energies 337.5 and 338.4 eV (Figure 2-6A). Because there is not ligand present in the structure of the PPX film, Pd(II) sites on the PD1 catalyst cannot covalently bind to the surface in this case. However, traces of PD1 are adsorbed to the surface in amounts insufficient to catalyze homogeneous electroless plating, consistent with behavior previously observed for this catalyst.¹⁷ Consequently, the PD1 deposited here retains its inherent chemical composition unperturbed by ligand binding. The peaks at 337.5 and 338.4 eV can be assigned to Pd–O and Pd–Cl of the oxo/hydroxo and chloro bridged Pd sites¹⁸ of PD1. Literature values for binding energy of Pd in PdO¹⁹ and PdCl₂²⁰ closely match the binding energies assigned to Pd–O and Pd–Cl species in this work.

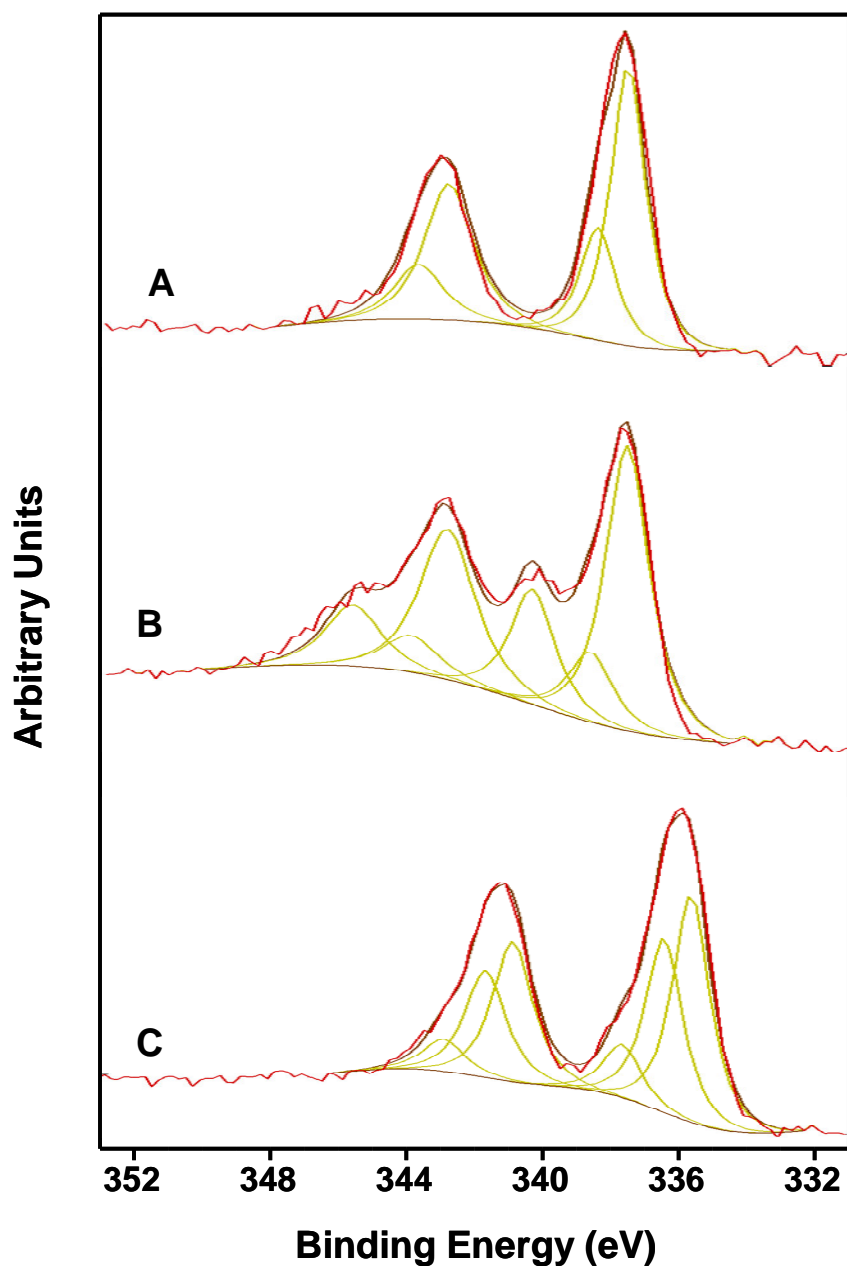


Figure 2-6. High resolution XPS spectra of Pd 3d region of (A) nanoPPX films treated with PD1 colloid for 30 min. (B) nanoPPX films treated with 0.2 M pyridine (aq) solution for 30 min and PD1 for 30 min (C) nanoPPX film treated with 0.2 M pyridine (aq) solution for 30 min and PD1 for 30 min and NIPOSIT™ 468B for 5 min. Reproduced with permission from Malvadkar *et al.*, *Langmuir* **26**, 4382–4391 (2010). DOI: 10.1021/la9034529. Copyright 2010 American Chemical Society.¹⁴

When nanoPPX films are treated with 0.2 M aqueous pyridine solution for 30 min prior to the treatment with PD1 for 30 min, the deconvoluted Pd 3d_{5/2} spectrum (Figure 2-6B) shows a strong peak at 340.3 eV in addition to the two peaks at 337.5 and 338.4 eV. The peak at 340.3 eV is an indication of Pd–N(pyridyl) interaction similar to the one observed in other studies.^{8,12} When the sample from Figure 2-6B is treated with 10% NIPOSIT™ 468B for 5 min, the entire Pd 3d spectrum shifts by ~2 eV towards lower binding energy (Figure 2-6C), indicating reduction of divalent Pd by dimethylamine-borane (DMAB) present in the NIPOSIT™ electroless metallization baths. This reduced Pd state is a necessary condition for electroless metallization to occur.¹⁸ However, the complexity of the signal, which requires three components to fit the band, indicates that other materials, such as Pd–O, unreduced Pd(II) species, and/or partially reduced Pd(I) species, in addition to metallic Pd(0) are likely present after reduction. Unfortunately, we are unable to unequivocally discern that nature of these species from our data.

A continuous Ni metallization requires catalyst density to be higher than a certain threshold limit, typically on the order of $\sim 10^{15}$ Pd(II) ions·cm⁻².¹² In order to test the presence of Ni layer on nanoPPX, a Ni 2p XPS spectrum was taken for three nanoPPX samples after plating. The first sample was treated with PD1 for 30 min and 10% NIPOSIT™ 468B for 5 min. The photoelectric spectrum shows no peaks in the Ni 2p region (Figure 2-7A) indicating absence of metallization. As explained previously, traces of PD1 (Pd = 0.43 at. %) adsorbed in absence of ligand are not dense enough to surpass the above threshold and therefore cannot sustain metallization. The second sample was treated with 0.2 M pyridine (aq) for 30 min prior to PD1 (30 min) and 10% NIPOSIT™

468B (5 min) treatments. The XPS data shows only a mild peak (Ni = 0.28 at. %) at 856.3 eV (Figure 2-7B) indicating a thin oxidized Ni layer. NanoPPX films treated with aqueous pyridine for a short time (30 min) can covalently bind PD1, evident from the XPS data in Figure 2-6C. While some portion of the surface did show metallization (visually), others did not, indicating that the surface is still deficient in PD1 for a *complete* Ni metallization. Results for the third Ni sample, prepared using nanoPPX films treated with 0.2 M pyridine (aq) for 40 h, PD1 for 30 min, and 10% NIPOSIT™ 468B for 5 min, are shown in Figure 2-7C. The XPS spectrum shows a distinct Ni 2p_{3/2} peak (Ni = 5.90 at. %) at 852.3 (Figure 2-7C) indicating the presence of metallic Ni formation on nanoPPX surface. Pyridine treatment time of ~40 h densely bind PD1 particles (Pd = 2.47 at. %) to support continuous Ni metallization. The Ni 2p_{3/2} peak position is in excellent agreement with values previously reported in literature.²¹⁻²⁵ The Ni 2p_{3/2} peak at 856.1 eV indicates the presence of divalent Ni layer formed due to reaction with oxygen during deposition and after exposure of the metallized sample to air. Several studies report similar peak position for oxidized Ni, including Li (856.3 eV),²⁶ Zafeiratos (856.3 eV),²⁷ Sygellou (856.1 eV),²⁵ and Chow (856.1 eV)²³, consistent with our assignment.

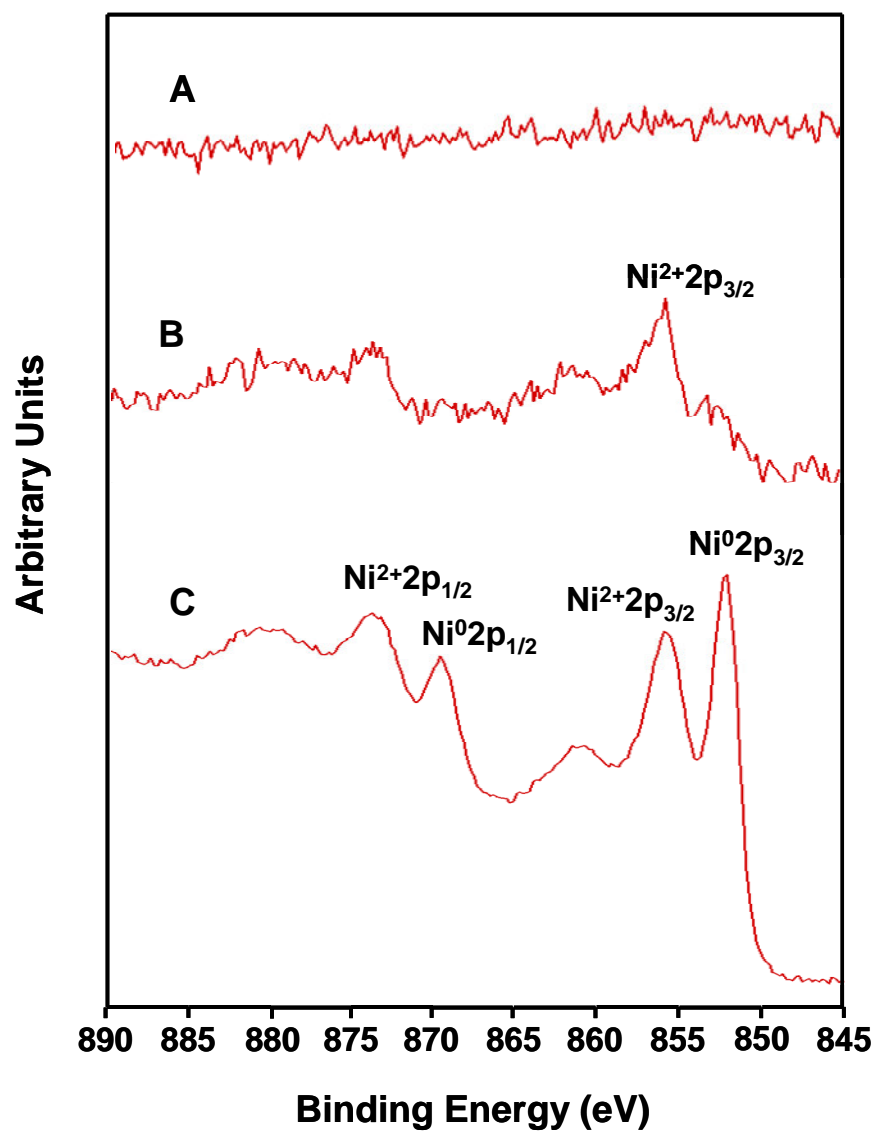


Figure 2-7. High resolution XPS spectra of Ni 2p region of (A) nanoPPX film treated with PD1 for 30 min and NIPOSIT™ 468B for 5 min (B) nanoPPX film treated with 0.2 M pyridine (aq) solution for 30 min and PD1 for 30 min and NIPOSIT™ 468B for 5 min. (C) nanoPPX film treated with 0.2 M pyridine (aq) solution for 40 h and PD1 for 30 min and NIPOSIT™ 468B for 5 min.

2.5. Factorial Analysis

In order to identify the important parameters that influence the evolution of the surface morphology, we carried out a systematic study using statistical designed experiments. We used a four factor two-level factorial design to analyze the effects due to the variables and their interactions in the metallization process. To perform factorial analysis the four factors: *Pyridine adsorption time (L)*, *PDI treatment time (C)*, *Ni plating time (N)* and the *Pyridine adsorption condition (F)* were assigned two levels (low and high) as listed in Table A-1 (Appendix A). Since the first three variables are quantifiable, the high and low values are simply the lower and higher treatment time. For *Pyridine adsorption condition (F)*, the two levels consisted of aqueous pyridine (liquid phase) and vapor phase pyridine treatment (note Section 2.2.1) at room temperature and 110 °C, respectively. Therefore, the complete experimental design consisted of $2^4 = 16$ samples. The nanoPPX properties and other metallization parameters such as bath concentration and temperature were kept constant for all the samples. RMS surface roughness obtained from AFM data was used as the response variable. For every sample, 3 to 6 AFM scans on randomly selected areas on the sample were used to record the surface roughness (Appendix A, Table A-2). Tables A-3 and A-4 (Appendix A) summarize the calculations used to determine the main and interaction effects for the response. Analysis of variance (ANOVA) was performed to determine the significance of each effect at the 99% confidence interval (Appendix A, Table A-5 and A-6). The effects were grouped as 99% significant or not significant. Effects that were grouped as not-significant were treated as random error that did not influence the response.

Table 2-3 lists the mean RMS roughness values (see Appendix A, Table A-2 for details) measured for all the 16 films along with the standard deviations. The roughness data was processed through a series of calculations (see Appendix A, Tables A-3 and A-4 for details) to determine the factor effects and interactions, which are also listed in Table 2-3. An analysis of variance (ANOVA) of the raw roughness data (see Appendix A, Tables A-5 and A-6 for details) was performed to identify variables and variable interactions that influence Ni roughness. The analysis was carried out at the 99% confidence level. Variables and their interactions exerting a significant effect at the 99% confidence level are identified in Table 2-3. As seen in Table 2-3, (Significance Level column) all factor effects are significant at the 99% confidence level. Likewise, all factor interactions, except *Ni plating time* × *PDI treatment time* (*NC*) and *PDI treatment time* × *Pyridine adsorption time* × *Pyridine adsorption condition* (*CLF*) interactions are significant at the 99% confidence level. From the ANOVA calculations, it is clear that not only these four variables but also most of their interactions significantly influence the surface morphology of the Ni film within the ranges of the variable specified here. Such behavior clearly suggests that the growth of the Ni on the nanoPPX is a complex serial process where the ligand adsorption time, PDI catalyst treatment time, Ni plating time, and the ligand adsorption conditions interdependently affect the measured roughness of the Ni films.

Table 2-3. Summary of the 2⁴ factorial analysis for Ni deposited nanoPPX films.¹⁴

Sample No.	Ni Plating Time, N(min) ^a	PD1 Treatment Time, C(min) ^b	Pyridine Adsorption Time, L(h)	Pyridine Condition, F ^c	Mean Roughness, R(nm) ^d	Effect ID	R Effect ^e	Significance Level ^f
1	30	45	30	Aq.	44.28	Ave	39.37	—
2	60	45	30	Aq.	39.07	<i>N</i>	2.99	99%
3	30	90	30	Aq.	29.77	<i>C</i>	-10.59	99%
4	60	90	30	Aq.	25.50	<i>NC</i>	-0.65	NS
5	30	45	48	Aq.	33.56	<i>L</i>	-1.59	99%
6	60	45	48	Aq.	29.98	<i>NL</i>	4.09	99%
7	30	90	48	Aq.	25.03	<i>CL</i>	3.67	99%
8	60	90	48	Aq.	32.85	<i>NCL</i>	5.96	99%
9	30	45	30	Vap.	47.74	<i>F</i>	13.26	99%
10	60	45	30	Vap.	59.29	<i>NF</i>	4.46	99%
11	30	90	30	Vap.	43.64	<i>CF</i>	-4.50	99%
12	60	90	30	Vap.	33.90	<i>NCF</i>	-2.32	99%
13	30	45	48	Vap.	48.31	<i>LF</i>	1.82	99%
14	60	45	48	Vap.	52.85	<i>NLF</i>	2.19	99%
15	30	90	48	Vap.	33.73	<i>CLF</i>	0.36	NS
16	60	90	48	Vap.	50.38	<i>NCLF</i>	4.88	99%

^a All films were rinsed in water and dried under N₂ gas after PD1 treatment. Ni bath consisted of freshly prepared 10% NIPOSITTM. ^b Aqueous pyridine treated nanoPPX films were rinsed in water and transferred to the PD1 colloidal dispersion (see Section 2.2.2 for details on preparation of PD1). Vapor pyridine treated nanoPPX films were directly transferred to the colloidal PD1 dispersion directly without the rinsing step. The PD1 treatment for all films was carried out in a temperature controlled water bath kept at 25 ± 1 °C. ^c Aq.: nanoPPX films treated with 1M aqueous pyridine solution. Vap.: nanoPPX films treated with vapor pyridine (see Section 2.2.1 for details). ^d RMS roughness was obtained using Nanoscope® software from 3 to 6 scans (5µm × 5µm) on randomly selected areas on each sample. ^e Refer to Appendix A (Tables A-3 and A-4) for details of the calculations. ^f Significance level obtained from ANOVA calculations (Appendix A: Tables A-5 and A-6). NS: not-significant.

Among the factor effects, the effect *Pyridine adsorption condition (F)* has the highest magnitude (13.26) as shown in Table 2-3 (R Effect column). To better understand the effect *F*, we studied the surface topography of samples 3 and 11 using AFM and FESEM. Sample 3 is a Ni layer deposited on nanoPPX treated with aqueous pyridine while sample 11 is a Ni layer deposited on nanoPPX treated with vapor pyridine. The remaining factors (*i.e.*, *N*, *C*, and *L*) are the same for both samples. Figures 2-8A and 2-8B show the contact-mode AFM images of sample 3 and 11 (from Table 2-3), respectively. It is clear from the AFM images that sample 11 has a higher roughness compared to sample 3. FESEM images of samples 3 and 11 (Figures 2-8C and 2-8D, respectively) provide further insight on the mechanism involved in the formation of their respective final morphologies. The magnified image (Figure 2-8C, inset) shows the presence of a smooth Ni nanoparticle decorating a PPX nanorod. On the other hand, Figure 2-8D inset, shows multiple Ni nanoparticles providing a rougher surface deposited onto a PPX nanorod. The difference in the two morphologies is translated into different AFM roughness values observed for the two adsorption conditions. The dependence of the morphology on the ligand adsorption condition suggests that the amount of ligand and the ligand molecule orientation in the polymer are factors that need further consideration.

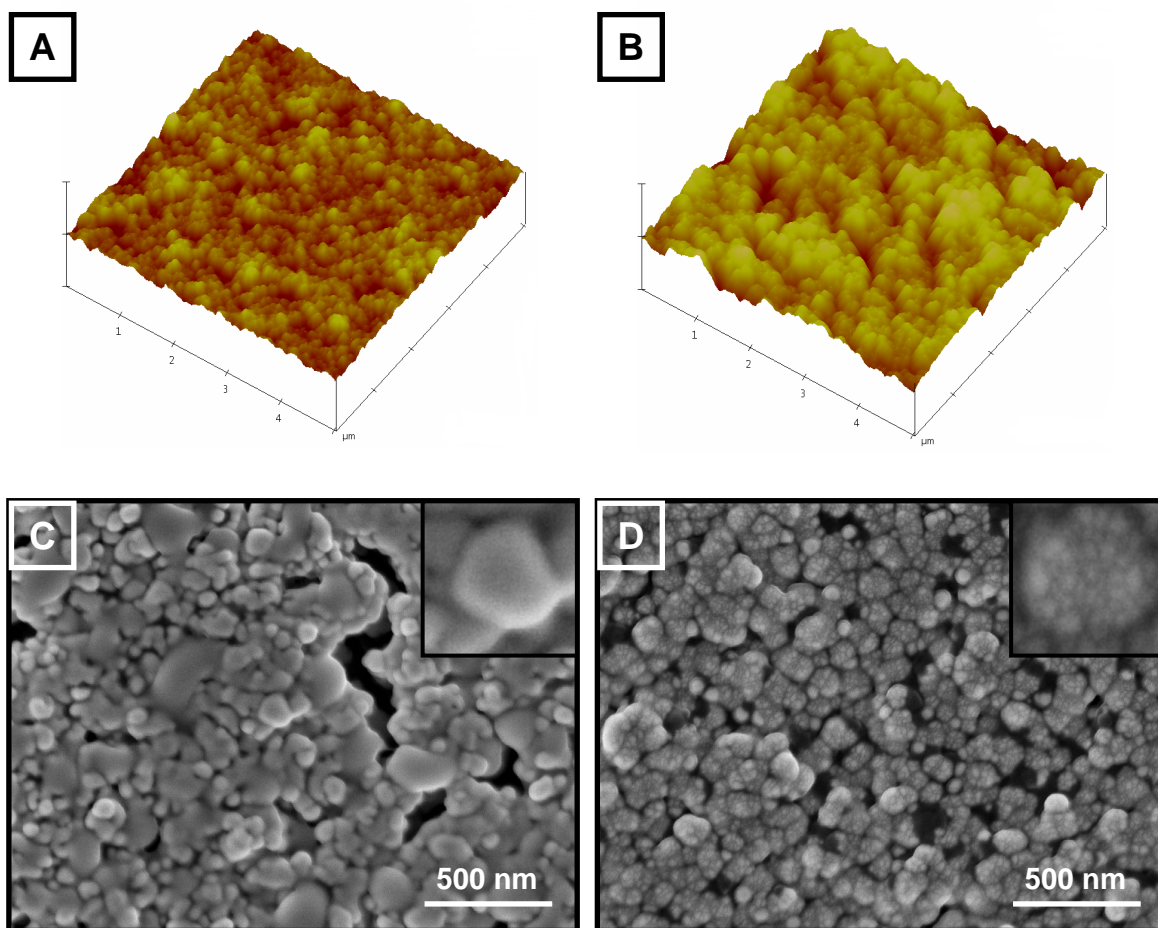
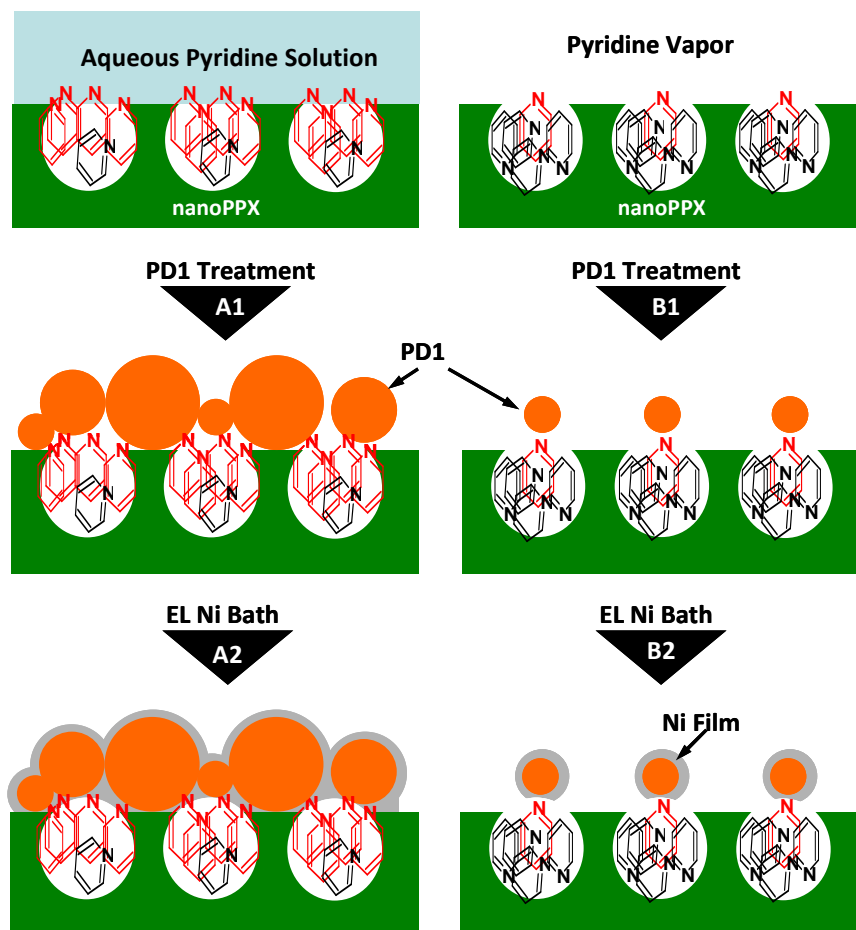


Figure 2-8. Contact mode AFM image of Ni layer deposited on nanoPPX films functionalized using (A) aqueous pyridine treatment and (B) vapor pyridine treatment. The unit length in the x-y scale is 1 μm and the z scale unit is 700 nm in each AFM image. FESEM image of Ni layer deposited on nanoPPX films functionalized using (C) aqueous pyridine treatment and (D) vapor pyridine treatment. For (C) and (D), inset images show magnified views of a single nanoPPX column with inset square side = 100 nm. For the samples in all images ligand adsorption time = 30 h, PD1 treatment time = 90 min., Ni plating time = 30 min. Reproduced with permission from Malvadkar *et al.*, *Langmuir* **26**, 4382–4391 (2010). DOI: 10.1021/la9034529. Copyright 2010 American Chemical Society.¹⁴

2.6. Model Refinement

In the concept paper a simple model, summarized in Section 2.3, relating ligand adsorption to noncovalent π - π interactions established between the ligand and disordered aromatic polymer chains present at the highly curved surfaces of the PPX nanorods.⁸ We now further refine this simple model, using the observed FESEM and AFM results from Figure 2-8, to account for the differences in Ni film morphology observed for the vapor and aqueous pyridine treatment conditions. A cartoon depicting the refined metal growth model is shown in Scheme 2-6. According to that model, partitioning of the pyridine molecules from the aqueous solution phase into the nanoPPX occurs primarily due to the difference in the chemical potential of pyridine in the two states and without any external activation, thereby limiting the amount of ligand entering the nanoPPX film. Under these conditions, the degree of penetration and the amount of pyridine adsorbed will be limited because energy is required to break the hydrogen bonds solvating the hydrophilic N-site of the pyridine molecule before it can fully enter the hydrophobic PPX film. The presence of a hydrated N-site is also expected to preferentially orient the ligand during insertion to keep the hydrophilic N ligand site in contact with the aqueous interface. The presence of this solvent shell may also provide a steric effect that limits the packing density of the ligand at the aqueous-PPX interface, countering the orientation effect. We observe attachment of PD1 having a broad particle size distribution in high surface coverage in our work (Scheme 2-6, Path A). Such behavior is consistent with the presence of ligand at high surface coverage,²⁸ suggesting that orientation rather than steric effects dominate in our system under aqueous conditions.



Scheme 2-6. Cartoon showing effect of ligand adsorption condition on resulting metal surface morphology. Path A and B show treatment of a nanoPPX film with aqueous pyridine solution and pyridine vapor, respectively. Pyridine molecules available for PD1 binding are shown in red (N-sites at the nanoPPX surface), while those which are unavailable for PD1 binding are shown in black (N-sites not at the nanoPPX surface).

In contrast, vapor deposition of pyridine is a thermally assisted process and therefore results in higher adsorption of pyridine molecules in the nanoPPX film. However, due to the absence of any solvent, the molecules can penetrate the PPX film more deeply and enter in more random orientations than for aqueous ligand adsorption.

Therefore, although larger quantities of pyridine may be incorporated *via* vapor deposition, fewer N-sites may be accessible at the aqueous–PPX interface to bind PD1. The lower density of available N ligand sites at the interface in this case is expected to lead to binding of less PD1 catalyst overall and preferential binding of the smaller catalyst particles from the PD1 particle distribution (Scheme 2-6, Path B).²⁸

Consequently, different Ni film morphologies are expected and observed for samples treated by aqueous pyridine compared to those treated by vapor pyridine. During electroless plating, metal growth initiates isotropically from the surface of each Pd(0) nanoparticle site on the surface. For the samples treated with aqueous pyridine, larger Pd(II) nanoparticles will be bound at higher densities due to the relatively high surface density of accessible pyridine N-sites present. As Ni metal fronts proceed outward from each Pd site, they will quickly encounter metal fronts from adjacent Pd nanoparticles and merge. As a result, voids between Pd sites will quickly fill with Ni metal, leading to a relatively smooth Ni surface consistent with our observations in Figures 2-8A and 2-8C.

In contrast, the lower density of pyridine N-sites accessible to the aqueous PD1 catalyst dispersion for the vapor deposited ligand is expected to bind fewer and smaller Pd(II) nanoparticles. Consequently, Ni deposition will be slower and Ni metal fronts will require longer times to meet and merge due to the increased average distance between surface Pd sites. Given a fixed Ni plating time as described for Figure 2-8, fewer Ni fronts will have merged for the samples prepared by the vapor pyridine deposition compared to the aqueous pyridine deposition. Consequently, a rougher Ni surface is expected as observed in Figures 2-8B and 2-8D. It should be noted that for longer plating time, the Ni surface on vapor pyridine treated nanoPPX film will and does eventually

smoothen as the electroless metal fronts merge consistent with the properties of the catalyst and electroless Ni bath.

2.7. Summary

In summary, we have employed noncovalent ligand functionalization on oblique angle polymerized nanoPPX templates to deposit metal nanoparticles and electroless metal films. Pyridine, physisorbed into the nanoPPX films, serves as the functional ligand, while a Pd(II) colloid that covalently binds to the pyridyl N-sites seeds the metallization process in our nanoPPX system. XPS data supports the noncovalent and covalent nature of interactions between pyridine–PPX and Pd(II)–pyridine, respectively. Although the polymer metal composite structure involves weak noncovalent interactions, the interface does not show any sign of adhesive weakness.⁸ Such behavior is ascribed to the expected mechanical interlocking between the deposited metal and the polymer nanostructure as well as the high density of noncovalent binding interactions noted elsewhere for analogous noncovalent based systems.²⁹ Furthermore, adsorption of pyridine into the nanoPPX film supports complete and conformal metallization of the surface.

A preliminary growth model correlating the adsorption of pyridine to the formation π – π interactions with the disordered aromatic entities of the PPX chains, formed by the high curvatures of the PPX surface, was suggested by Demirel *et al.*⁸ The preliminary model is refined taking into account the effect of ligand orientation at the nanoPPX surface, controlled primarily by the pyridine adsorption condition (aqueous solution *vs.* vapor phase), on the final morphology of the metal deposited. Other factors

such as ligand adsorption time, PD1 treatment time, and metal plating time are also shown to influence the morphology of the metal layer, as suggested by a statistical investigation conducted using a 2^4 factorial analysis. Although a certain level of control over the metal morphology is possible by modifying the deposition parameters at the polymer preparation and/or the metal plating stages, challenges lie in expanding the generality of this method to incorporating other functional ligands (besides pyridine) which can facilitate deposition of other metals and ceramics.

References

1. Gorham, W. F. *Journal of Polymer Science Part a-1-Polymer Chemistry* **4**, 3027-3039 (1966).
2. Cetinkaya, A., Boduroglu, S. & Demirel, M. C. *Polymer* **48**, 4130-4134 (2007).
3. Cetinkaya, M., Malvadkar, N. & Demirel, M. C. *Journal of Polymer Science Part B-Polymer Physics* **46**, 640-648 (2008).
4. Hawkeye, M. M. & Brett, M. J. *Journal of Vacuum Science & Technology A* **25**, 1317-1335 (2007).
5. Cetinkaya, M. in *Synthesis and Characterization of Nanostructured Poly(p-xylylene) Films* (Doctoral Dissertation, Pennsylvania State University, Engineering Science and Mechanics, University Park, 2008).
6. Kao, P. et al. *Advanced Materials* **20**, 3562-3565 (2008).
7. Wenzel, R. N. *Industrial and Engineering Chemistry* **28**, 988-994 (1936).
8. Demirel, M. C., Cetinkaya, M., Singh, A. & Dressick, W. J. *Advanced Materials* **19**, 4495-4499 (2007).
9. Dressick, W. J. et al. *Colloids and Surfaces a-Physicochemical and Engineering Aspects* **108**, 101-111 (1996).
10. Zabetakis, D. & Dressick, W. J. *ACS Applied Materials & Interfaces* **1**, 4-25 (2009).
11. Brandow, S. L., Schull, T. L., Martin, B. D., Guerin, D. C. & Dressick, W. J. *Chemistry-a European Journal* **8**, 5363-5367 (2002).

12. Dressick, W. J., Dulcey, C. S., Georger, J. H., Calabrese, G. S. & Calvert, J. M. *Journal of the Electrochemical Society* **141**, 210-220 (1994).
13. Ada, E. T. et al. *Journal of Vacuum Science & Technology B* **13**, 2189-2196 (1995).
14. Malvadkar, N. A., Sekeroglu, K., Dressick, W. J. & Demirel, M. C. *Langmuir* **26**, 4382-4391 (2010).
15. Malvadkar, N., Park, S., Urquidi-MacDonald, M., Wang, H. & Demirel, M. C. *Journal of Power Sources* **182**, 323-328 (2008).
16. Sauerbrey, G. *Zeitschrift Fur Physik* **155**, 206-222 (1959).
17. Chen, M. S. et al. *Journal of the Electrochemical Society* **146**, 1421-1430 (1999).
18. Charbonnier, M. et al. *Thin Solid Films* **515**, 1623-1633 (2006).
19. Militello, M. C. & Simko, S. J. *Surface Science Spectra* **3**, 395-401 (1994).
20. Militello, M. C. & Simko, S. J. *Surface Science Spectra* **3**, 402-409 (1994).
21. Kukula, P. & Cervený, L. *Applied Catalysis a-General* **223**, 43-55 (2002).
22. Shutthanandan, V., Saleh, A. A. & Smith, R. J. *Surface Science* **450**, 204-226 (2000).
23. Chow, Y. M., Lau, W. M. & Karim, Z. S. *Surface and Interface Analysis* **31**, 321-327 (2001).
24. Sirtori, V., Lombardi, L., Cavallotti, P. L. & Magagnin, L. *Applied Surface Science* **217**, 163-169 (2003).
25. Sygellou, L. et al. *Surface and Interface Analysis* **34**, 545-549 (2002).
26. Li, L. B., An, M. Z. & Wu, G. H. *Surface & Coatings Technology* **200**, 5102-5112 (2006).

27. Zafeiratos, S. & Kennou, S. *Surface Science* **482**, 266-271 (2001).
28. Brandow, S. L., Dressick, W. J., Marrian, C. R. K., Chow, G. M. & Calvert, J. M. *Journal of the Electrochemical Society* **142**, 2233-2243 (1995).
29. Chen, M. S., Brandow, S. L., Schull, T. L., Chrisey, D. B. & Dressick, W. J. *Advanced Functional Materials* **15**, 1364-1375 (2005).

Chapter 3. TiO₂/NanoPPX Hybrid Nanostructures*

3.1. Introduction

In the preceding chapter, we described a method to prepare conformal metal layer over nanoPPX film *via* a three-step deposition process: noncovalent ligand functionalization of PPX nanorods, followed by catalysis using Pd1 colloid, and finally electroless plating. To extend the generality of the noncovalent functionalization approach to fabricating ceramic nanostructures, we now demonstrate liquid phase deposition (LPD) of TiO₂ on nanoPPX films.

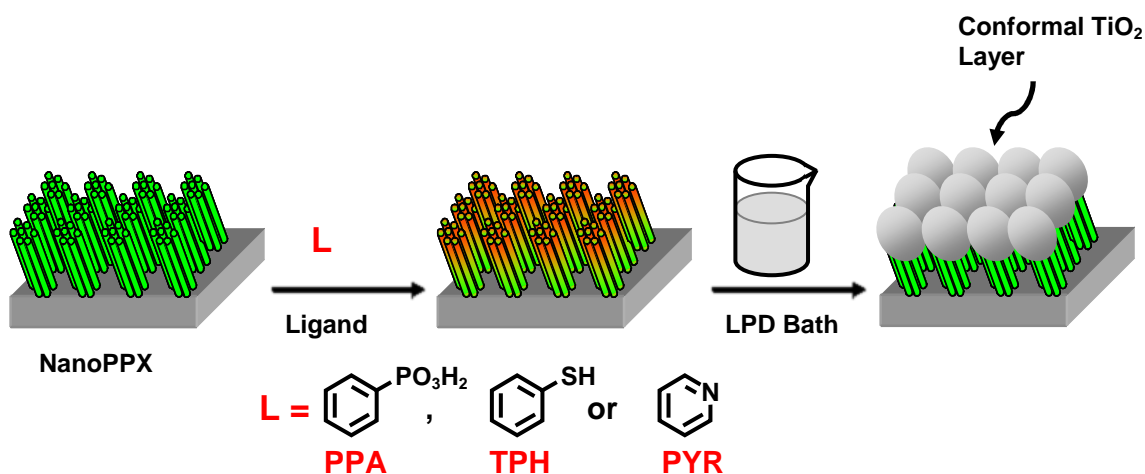
LPD is a process in which controlled hydrolysis of metal ions in aqueous solution generates oxide or related precursor species that are subsequently deposited onto various substrate surfaces.¹ The process differs from electroless deposition in that no change in redox state occurs during the deposition process so that no reductant or catalyst is required. A variety of metal oxides, including TiO₂,²⁻⁸ can be deposited in this manner, with oxide composition and morphology determined primarily by the precursor metal species, hydrolysis conditions, and substrate surface chemistry.¹ Oxide nucleation and growth can occur directly at the substrate surface through a heterogeneous nucleation and growth process to form a conformal oxide coating and within the aqueous solution to generate oxide nanoparticles.⁹ The latter process is increasingly favored in highly

* Some contents of this chapter are reproduced in part with permission from Malvadkar *et al.*, *Journal of Materials Chemistry* **19**, 4796–4804 (2009) DOI: 10.1039/b902882j. Copyright 2009 The Royal Society of Chemistry.

supersaturated solutions and ultimately leads to inclusion of the resulting nanoparticles in the oxide film growing at the substrate surface.^{1,9}

In this chapter, we demonstrate, *via* a two-step deposition procedure, that LPD of TiO₂ on nanoPPX film, using (NH₄)₂TiF₆ as the precursor and an appropriate noncovalent ligand, leads to conformal ceramization of the PPX nanorods. Furthermore, the physicochemical properties of such hybrid nanostructures are profoundly influenced by the functionality of the ligand used.

3.2. Preparation of TiO₂/NanoPPX Hybrid Nanostructures



Scheme 3-1. Schematic showing preparation of hybrid TiO₂/nanoPPX nanostructures using a two-step procedure: (1) noncovalent ligand adsorption in nanoPPX, and (2) LPD of TiO₂.

Scheme 3-1 depicts the simple two-step procedure used for deposition of TiO₂ films onto our nanoPPX substrates. Planar or nanoPPX coated Si wafers were incubated in 0.5 M aqueous phenylphosphonic acid (PPA), 0.5 M aqueous pyridine (PYR), or 0.5

M thiophenol (TPH) in ethanol solutions in closed glass containers in a fume hood for 48 h. The wafers were then rinsed in their respective solvents and transferred to the TiO₂ bath. The LPD bath⁹ was prepared immediately prior to use and consisted of an aqueous solution containing 0.05 M (NH₄)₂TiF₆ and 0.15 M H₃BO₃. Dilute aqueous hydrochloric acid, HCl, was added to adjust the pH to 2.88. The PPX coated wafers were submerged vertically in the bath held at 50 °C for 3 to 24 h to deposit the TiO₂ films. The wafers were then removed from the bath, sonicated in water for 30 s (VWR Scientific Model 75 HT Aquasonic Bath), rinsed in water, and dried in a stream of N₂ gas (compressed N₂ tank, water-pumped). Wafers were stored in sealed Fluoroware[®] containers until needed for characterization.

3.3. Mechanism for Ceramization of NanoPPX Film

Figures 3-1A and 3-1B show FESEM images of TiO₂ layer deposited *via* Scheme 3-1 (phenylphosphonic acid as the ligand) on nanoPPX and planar PPX surfaces, respectively. While TiO₂ deposition on a nanoPPX surface is continuous and conformal, analogous ceramization of a planar PPX surface shows non-continuous (*i.e.*, patchy) TiO₂ deposits (Figure 3-1A and 3-1B, respectively). Such a behavior is congruent with that observed after electroless metallization of the two films functionalized *via* the noncovalent route (Ref. Chapter 2), attributed to the poor adsorption of ligand molecules in a planar structure.

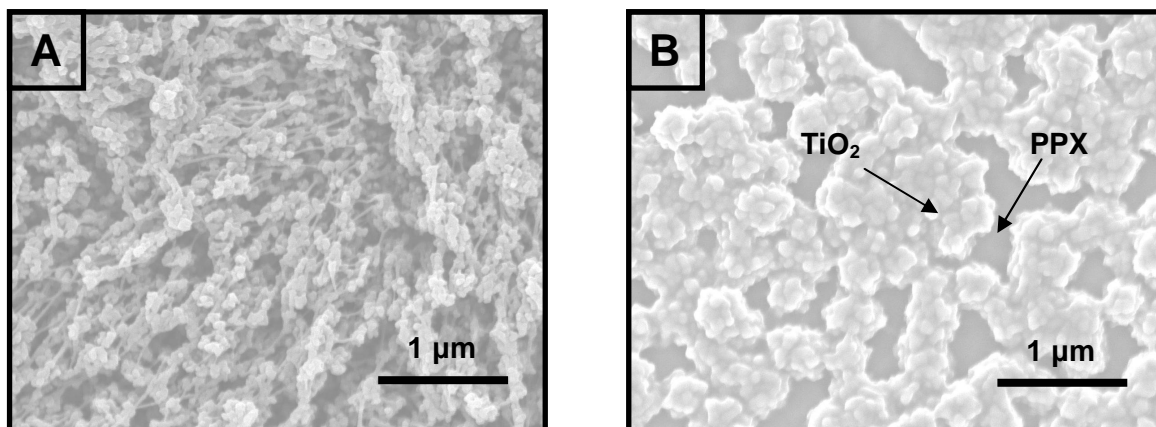
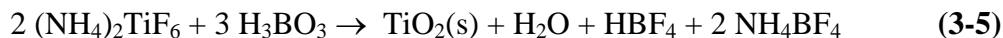
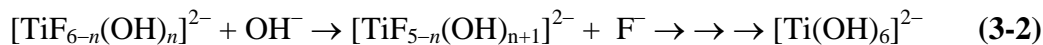
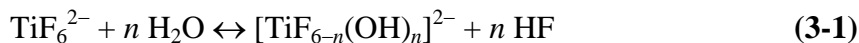


Figure 3-1. FESEM image of TiO_2 deposited on PPA-functionalized (A) nanoPPX film, and (B) planar PPX film. Reproduced with permission from Malvadkar *et al.*, *Journal of Materials Chemistry* **19**, 4796–4804 (2009) DOI: 10.1039/b902882j. Copyright 2009 The Royal Society of Chemistry.

Ligand physisorption and stabilization in a nanoPPX film occurs *via* the noncovalent mechanism described in Chapter 2. Briefly, formation of favorable π – π interaction and/or van der Waals interactions occur between hydrophobic portions of the ligand structure and aromatic residues of the PPX chains in a process analogous to that described for ligand adsorption into solvent-templated “nanocavities” in aromatic organosiloxane SAMs.¹⁰⁻¹⁵ For the nanoPPX films, however, the corresponding “nanocavities” are templated by the anisotropic growth conditions present during the vapor-phase OAP process, rather than a solvent. Ligand adsorption is facilitated by the amorphous nature and high curvature of the PPX nanorods formed, while corresponding planar PPX films exhibit negligible ligand binding.¹⁶ The three-dimensional nature of the PPX polymer chains in nanoPPX films provides added conformational flexibility in binding ligand molecules compared to the more rigid two-dimensional aromatic siloxane

SAMs, permitting dissolution and successful binding of a wider range of ligands *via* the use of small hydrophilic alcohols such as ethanol, in addition to water, as ligand solvents.

To prepare the LPD bath for TiO₂ deposition, we have utilized aqueous hexafluorotitanate solutions containing boric acid as a fluoride ion scavenger at pH 2.88 and ~50°C to control the TiF₆²⁻ hydrolysis rate, as illustrated in Equations 3-1–3-4, with the net oxide deposition reaction shown in Equation 3-5:



Under these deposition conditions, the solution is highly supersaturated and TiO₂ nucleation and growth both directly at the substrate surface and in the solution occur, with subsequent incorporation of TiO₂ nanoparticles formed in the solution into the surface TiO₂ film.⁹

3.4. Effect of Ligand Functionality

We tested three species, namely phenylphosphonic acid (PPA), thiophenol (TPH) and pyridine (PYR), which spans a range of TiO₂ binding strengths, as ligands. Because Ti(IV) preferentially binds oxygen-, rather than nitrogen-containing ligands, it binds

strongly to phosphonate-containing species such as PPA but interacts only weakly with aromatic N-containing species such as PYR.¹⁷ The selection of TPH represents a ligand of intermediate binding strength due to the presence of the –SH site, rather than the more strongly interacting –OH site of the PPA. After incorporation of ligand into the nanoPPX film, treatment with the aqueous hexafluorotitanate-boric acid LPD bath in the second process step of Scheme 3-1 initiates TiO₂ film deposition at the ligand sites.

Table 3-1 summarizes our TiO₂ deposition results as functions of (1) LPD bath treatment time for PPA-impregnated PPX films, and (2) type of ligand for nanoPPX films separately treated by each ligand (48 h) and the LPD bath (24 h). Ligand functionality significantly affects the deposition of TiO₂ onto the PPX film. TiO₂ coverage decreases from > 95% when PPA ligand is present to ~50–90% for TPH and < 10–20% for PYR in Table 3-1. The Ti EDX signal of 19.8% noted for PPA is reduced to 14.7% for TPH and just ~1% for PYR. Both trends correspond to the expected TiO₂-ligand binding strength of PPA > TPH >> PYR. Although PYR adsorbs well to the PPX nanostructures,¹⁶ its weaker interactions with Ti^{IV} species severely limits TiO₂ deposition. However, adsorbed pyridyl N-sites typically exhibit surface pK_a's of ~3.3–5.9^{18,19} and will be substantially protonated under our TiO₂ deposition conditions (*i.e.*, 72.5–99.9% protonation, respectively, at pH 2.88). Therefore, the minimal TiO₂ deposition observed in this case more likely results from weaker electrostatic, rather than covalent, interactions between anionic TiO₂ precursors shown in Equations 3-1–3-3 and accessible protonated pyridyl sites on the PPX surface. In the absence of prior ligand treatment, only traces of TiO₂ are observed, consistent with expectation for the model of Scheme 3-1.

Table 3-1. TiO₂ deposition on ligand-treated nanoPPX films. Reproduced with permission from Malvadkar *et al.*, *Journal of Materials Chemistry* 19, 4796–4804 (2009)

DOI: 10.1039/b902882j. Copyright 2009 The Royal Society of Chemistry²⁰

Ligand Type ^a	LPD Bath ^c Time (h)	Initial TiO ₂ Coverage (%) ^d	% C (EDX)	% Ti (EDX)	TiO ₂ Thickness (μm)	Contact Angle (degrees) ^e
PPA	1	—	—	—	0.21 ± 0.1	 88 ± 2°
PPA	3	> 95%	74.3%	4.3%	0.76 ± 0.1	 43 ± 5°
PPA	6	> 95%	53.0%	9.2%	1.19 ± 0.5	 < 3°
PPA	24	> 95%	19.2%	19.8%	2.26 ± 0.4	 < 3°
TPH ^b	24	~50–90%	34.8%	14.7%	2.03 ± 0.2	 < 3°
PYR	24	< 10–20%	67.5%	~1.0%	0.69 ± 0.2	 51 ± 5°
None	24	< 5%	—	—	< 0.15	 103 ± 2°
Control Polymer	0	0%	—	—	0	 124 ± 5°

^a Treatment with 0.5 M aqueous ligand solution for 48 h unless noted otherwise. ^b Ethanol as the solvent. ^c pH 2.88 at 50°C. ^d Visually estimated from scanning electron micrographs of substrates after TiO₂ deposition. ^e Average ± 3σ (6 measurements).

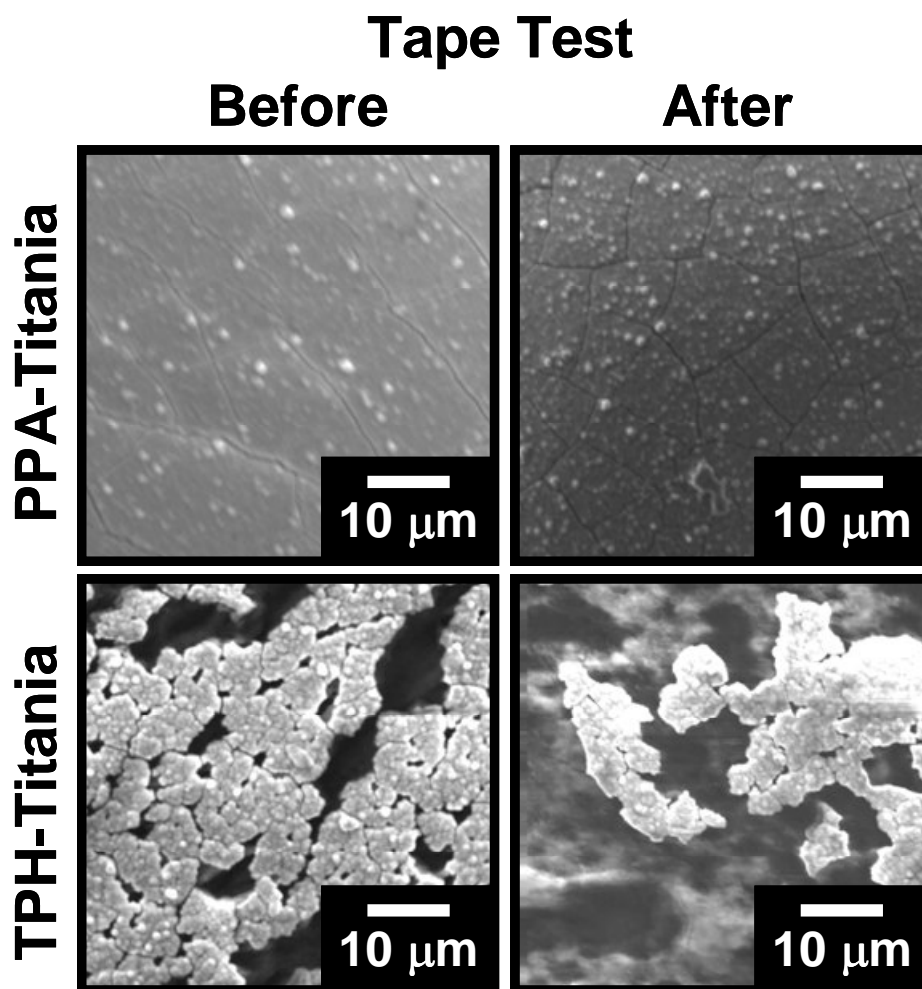


Figure 3-2. TiO₂ adhesion tape test results. SEMs are shown for TiO₂ films deposited onto nanoPPX films bearing PPA or TPH ligand before and after tape removal. Samples were treated with ligand for 48 h followed by TiO₂ LPD for 24 h (note Section 3.2). Reproduced with permission from Malvadkar *et al.*, *Journal of Materials Chemistry* 19, 4796–4804 (2009) DOI: 10.1039/b902882j. Copyright 2009 The Royal Society of Chemistry.²⁰

Surface effects are also manifested in the adhesive behavior of the as-deposited TiO₂ films. Figure 3-2 illustrates Scotch[®] tape adhesion test results for TiO₂ films deposited onto the PPA- and TPH-impregnated nanoPPX films. Although some faint cracks appear after removal of the tape, negligible quantities (< 5%) of the TiO₂ film are removed from the surface when PPA ligand is present during the LPD process. TEM images (Figure 3-3) clearly reveal the presence of the ~100–150 nm diameter TiO₂ nanoparticles preferred for enhanced adhesion properties that are ideal for bioimplant composite applications.²¹ In addition, coiling of the PPX nanorods during the TiO₂ deposition, leading to enhanced adhesion *via* mechanical interlocking of the TiO₂ and the PPX components, is also observed. The excellent adhesion and high coverage of the TiO₂ in this case is consistent with its strong binding towards phosphonic acid OH groups over a large pH range (*i.e.*, 0–9).^{22,23} In contrast, at least 50% of the TiO₂ film (light areas, Figure 3-2) is removed from the PPX surface when the TPH ligand is used. Unfortunately, the incomplete and variable initial TiO₂ coverage (*i.e.*, 50–90%) associated with the TPH-impregnated PPX film precludes a more quantitative comparison of its adhesive properties at this time. Nevertheless, the results shown in Figure 3-2 clearly illustrate the importance of proper ligand selection in controlling the adhesion of the as-deposited TiO₂ film.

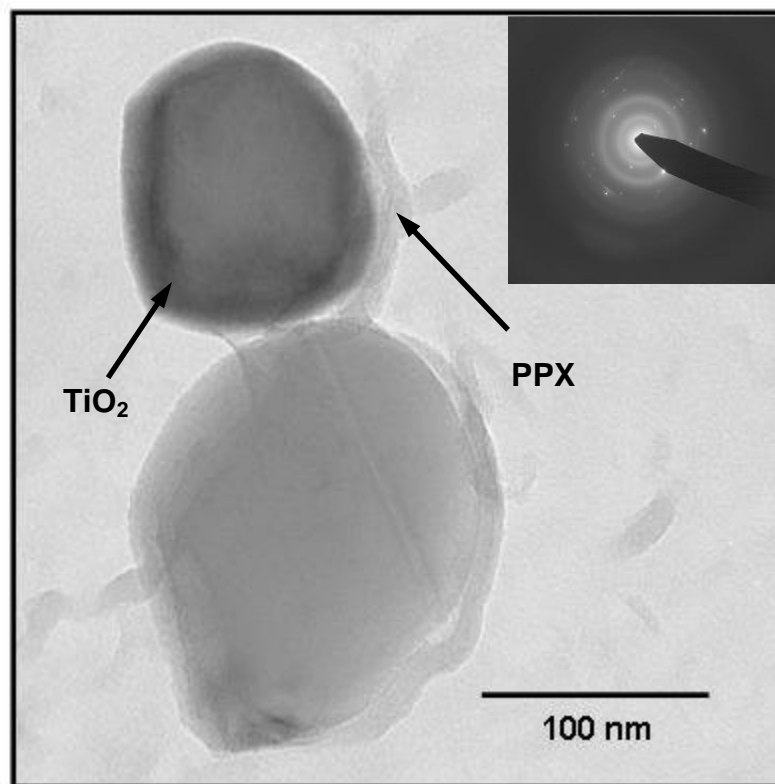


Figure 3-3. TEM image of TiO_2 particles deposited on PPA-functionalized nanoPPX film. PPX fibers are also visible. Inset shows electron diffractogram of the TiO_2 showing both ring and spot patterns. Reproduced with permission from Malvadkar *et al.*, *Journal of Materials Chemistry* **19**, 4796–4804 (2009) DOI: 10.1039/b902882j. Copyright 2009 The Royal Society of Chemistry.²⁰

3.5. Effect of LPD Bath Time

The growth of TiO_2 , measured using a profilometer, is summarized in Table 3-1 (thickness column) and depends on the type of the ligand present in the PPX film. While PPA and TPH treated PPX films show the highest growth rates, the PYR treated PPX film shows sluggish growth. The growth on untreated PPX film is relatively slower and

takes place primarily due to the physical entrapment of the TiO₂ nanoparticles in the porous PPX. The initial rapid TiO₂ growth rate eventually slows at longer bath treatment times, as shown in Figure 3-4 for the PPA-impregnated PPX film. This behavior reflects the diminished surface area available for TiO₂ deposition as filling of the interstitial regions between the PPX nanorods by TiO₂ is completed and the TiO₂ completely covers the PPX film.

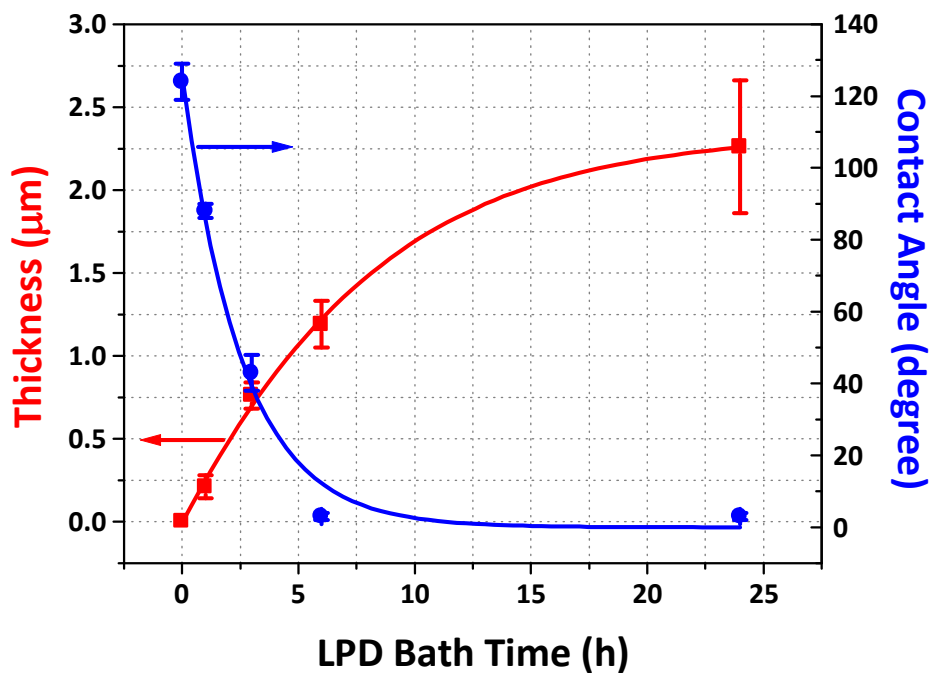


Figure 3-4. Dependence of thickness of TiO₂ layer and contact angle on LPD bath time. Samples were functionalized with PPA for 48 h prior to TiO₂ deposition. First-order exponential decay curves are shown for visual assistance.

The corresponding contact angles of the TiO₂/nanoPPX composites from Table 3-1 also drop steadily as the deposition proceeds, as shown in Figure 3-4. An unmodified

nanoPPX film possesses a hydrophobic surface with a contact angle of $124 \pm 5^\circ$ due to the inherent low surface energy of the PPX combined with the enhanced hydrophobicity due to the nanostructured morphology. As the TiO_2 covers the nanoPPX, the composite film exhibits a higher surface energy and therefore a lower contact angle. It is clear that after 6 h of TiO_2 deposition, the PPX surface is essentially completely covered with TiO_2 and therefore exhibits superhydrophilicity (*i.e.*, contact angle $\approx 0^\circ$). In general, higher coverage and thickness of the TiO_2 layer lowers the contact angle for the composite film, consistent with expectations based on the model of Scheme 3-1 and our TiO_2 growth rate and coverage observations.

3.6. Chemical Analysis

XPS analyses provide further insight concerning the nature of the TiO_2 deposits and support for the LPD method shown in Scheme 3-1. For example, the XPS spectra shown in Figure 3-5 illustrate the incorporation of the PPA ligand into the nanoPPX film after treatment with aqueous PPA solution but prior to TiO_2 film deposition. The single P(2p) peak at 133.5 eV (100.0%) in Figure 3-5A is identical to that observed elsewhere for analogous aromatic phosphonate species.²⁴ The corresponding O(1s) peaks due to P=O and P–OH are observed after deconvolution in Figure 3-5B at 531.6 eV (46.0%) and 533.1 eV (54.0%), respectively. These are in excellent agreement with values of 531.7 eV and 533.2 eV observed by Adolphi and coworkers²⁵ and 531.3 eV and 533.0 eV reported by Cabeza and coworkers,²⁶ respectively, for analogous phosphonic acid species.

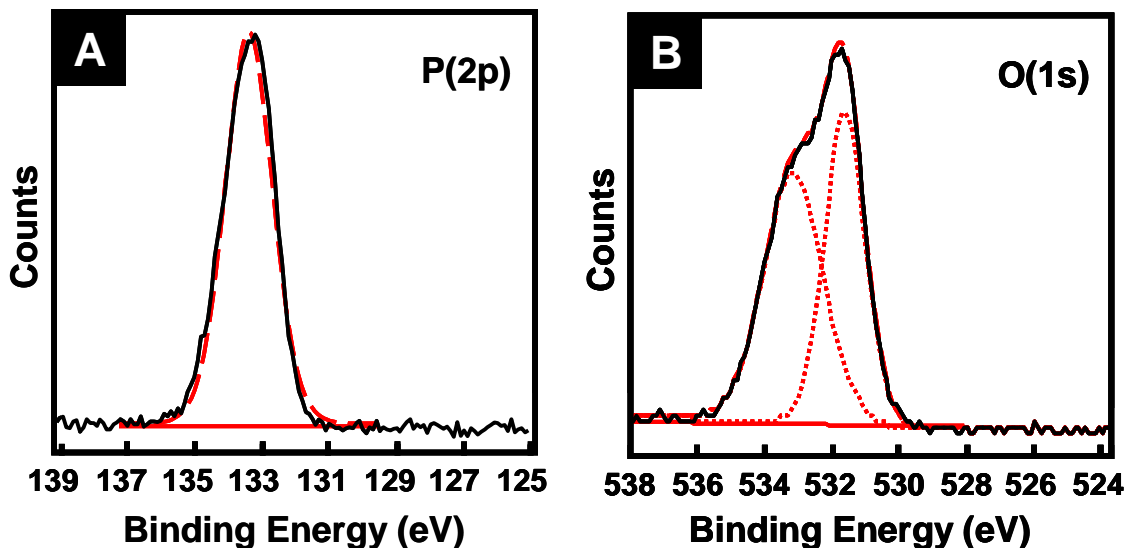


Figure 3-5. XPS spectra of PPA-functionalized nanoPPX film in (a) P(2p) region, (b) O(1s) region. Key: Black line = XPS spectrum; Red solid line = baseline; Red dotted line = deconvoluted XPS peaks; Red dashed line = fitted XPS spectrum. Reproduced with permission from Malvadkar *et al.*, *Journal of Materials Chemistry* **19**, 4796–4804 (2009) DOI: 10.1039/b902882j. Copyright 2009 The Royal Society of Chemistry.²⁰

Figure 3-6 shows the XPS results for the TiO₂ film of Figure 3-1A prepared by LPD using the PPA-impregnated nanoPPX film analyzed in Figure 3-5. The Ti(2p_{3/2}) signal shown in Figure 3-6A comprises two components after deconvolution at energies of 459.1 eV (87.7%) and 460.1 eV (12.3%). Identical values (± 0.1 eV uncertainty) of 459.1 eV (88.5%) and 460.2 eV (11.5%) are observed for TiO₂ films deposited onto the TPH-treated PPX substrate (note Figure 3-6C). These peak components occur at or just beyond the edge of the 458.4–459.0 eV Ti(2p_{3/2}) energy range usually associated with crystalline anatase and rutile titanium dioxide,^{2,27,28} complicating interpretation of the spectra. In fact, our spectra are consistent with the presence of both crystalline and

amorphous TiO_x ($x \leq 2$) phases. For example, mixed titanium oxides prepared using a sol-gel method²⁹ display a $\text{Ti}(2p_{3/2})$ peak at 459 eV analogous to the major peak component at 459.1 eV in Figure 3-6A. In addition, Bhaumik and coworkers²⁴ have previously observed a $\text{Ti}(2p_{3/2})$ peak at 460.4 eV, assigned to tetragonal coordination of Ti^{IV} by oxygen in a local crystalline environment, in porous disordered open-framework titanium oxophosphonate compounds. The appearance of a similar peak at 460.1 eV in Figure 3-6A (and ~ 460.2 eV in Figure 3-6C) is consistent with the presence of a corresponding crystalline component in our material. The selected area electron diffraction (SAED) (Figure 3-3 inset) too shows a combined diffuse ring and spot pattern which is typically associated with a mixed amorphous and polycrystalline structure. At least two mechanisms exist for incorporation of such material during our deposition process, including: (1) capture of crystalline TiO_2 nanoparticles independently nucleated in solution by the growing TiO_2 surface film, and (2) ligand-templated tetragonal coordination of Ti^{IV} , at least during the direct nucleation and growth of TiO_2 from the ligand-modified PPX surface that predominates during the initial stages of the LPD process. Unfortunately, our data are currently insufficient to ascertain which of these pathways, if any, contribute to the structure of our TiO_2 films.

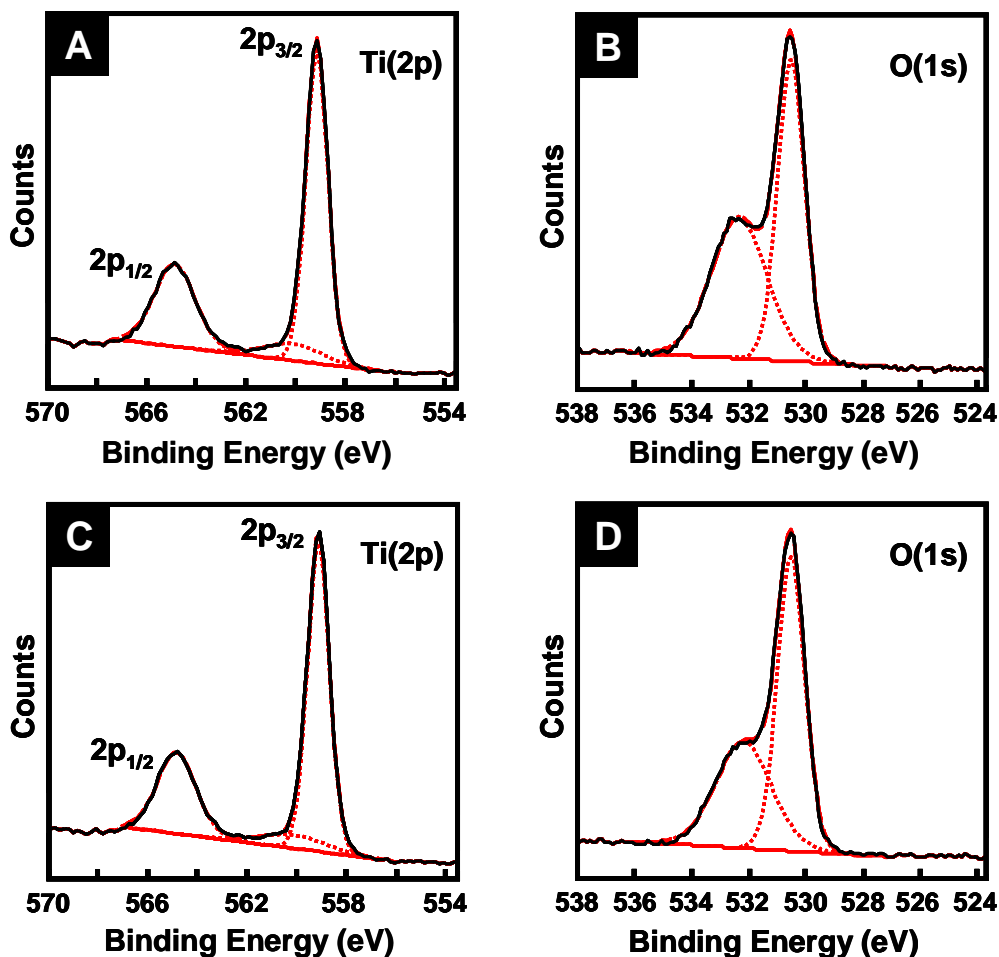


Figure 3-6. XPS spectra of TiO₂ deposited on PPA-functionalized nanoPPX film in (a) Ti(2p) region, (b) O(1s) region. XPS spectra of TiO₂ deposited on TPH-functionalized nanoPPX film in (c) Ti(2p) region, (d) O(1s) region. Key is identical to that used in Figure 3-5. Reproduced with permission from Malvadkar *et al.*, *Journal of Materials Chemistry* **19**, 4796–4804 (2009) DOI: 10.1039/b902882j. Copyright 2009 The Royal Society of Chemistry.²⁰

The O(1s) spectrum of the as-deposited TiO₂ film in Figure 3-6B exhibits component peaks after deconvolution at 530.4 eV (50.9%) and 532.3 eV (49.1%). Analogous O(1s) components are observed for TiO₂ films deposited onto TPH-

impregnated PPX films (*i.e.*, 530.4 eV (57.9%) and 532.1 eV (42.1%), note Figure 3-6D). The differences between the O(1s) spectra of Figures 3-6B and 3-6D (*i.e.*, the +0.2 eV shift of the higher energy O(1s) component for TiO₂ film deposited using PPA compared to TPH and its larger area relative to its 530.4 eV component) likely reflect minor differences in composition and/or structure between the deposited TiO₂ films, rather than contributions due to the phosphonate oxygen atoms of the PPA ligand for Figure 3-6B. The latter are excluded because no Cl(2p) signal due to the underlying PPX is observed during XPS analysis, indicating that the TiO₂ film of Figure 3-6B is sufficiently thick to attenuate any O(1s) signal due to physisorbed PPA ligands on the nanoPPX surface.

Examination of the O(1s) spectra further supports the presence of both crystalline and amorphous components in the as-deposited TiO₂ films. For example, Gonbeau and coworkers²⁸ attribute a Ti=O O(1s) peak at 530.4 eV to tetragonally coordinated Ti^{IV} in an ionic O²⁻ crystalline environment, with Ti-OH O(1s) peaks at 532.1–532.3 eV assigned to Ti^{IV} in a formal O⁻ environment comprising weakly adsorbed species and/or subsurface oxide deficiencies more characteristic of amorphous TiO_x ($x \leq 2$) films. In similar fashion, the component peak positions in Figure 3-6B (and Figure 3-6D) are in good agreement with those observed at 530.4 eV for Ti=O and 532.3 eV for Ti-OH in amorphous TiO_x ($x \leq 2$) films previously prepared using peroxotitanate solutions.³⁰

3.7. Nature of Crystallinity

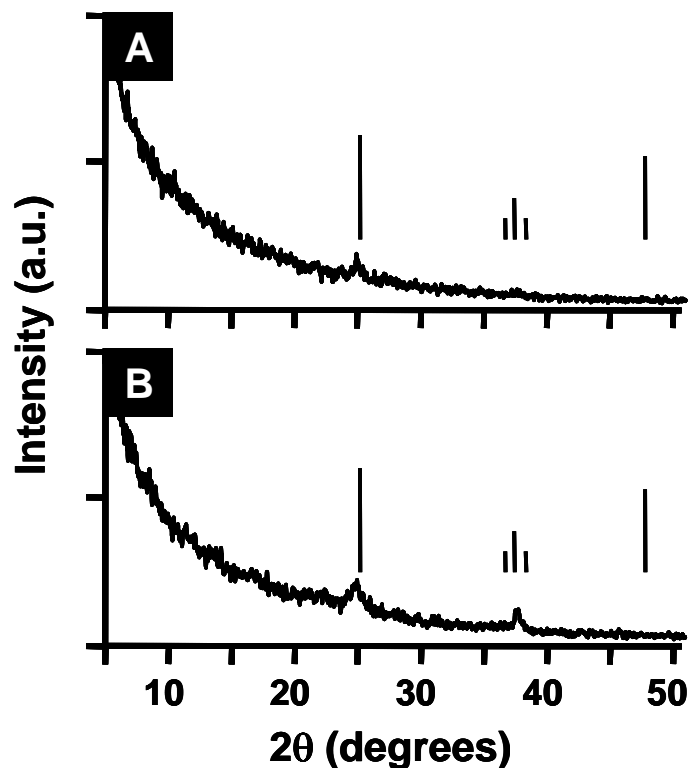


Figure 3-7. XRD spectra of TiO₂ films: (A) as-deposited; (B) after annealing (200°C, 24 h, Ar). Vertical bars identify the calculated positions and intensities for X-ray reflections due to anatase. Reproduced with permission from Malvadkar *et al.*, *Journal of Materials Chemistry* 19, 4796–4804 (2009) DOI: 10.1039/b902882j. Copyright 2009 The Royal Society of Chemistry.²⁰

XRD results shown in Figure 3-7 confirm the mixed structure of the TiO₂ films, supporting our interpretation of the XPS spectra in Figure 3-6. The XRD spectrum of the as-deposited TiO₂ film from Figure 3-1A is illustrated in Figure 3-7A. The absence of a diffraction peak at $2\theta = \sim 22^\circ$ associated with the underlying nanoPPX³¹ substrate is consistent with the essentially non-porous, conformal nature of the TiO₂ film. The small

diffraction peak observed at $2\theta = \sim 25^\circ$ in an otherwise featureless spectrum is characteristic of anatase, indicating deposition of a TiO_2 film containing both crystalline and amorphous phases under our LPD conditions. This behavior contrasts with the deposition of crystalline anatase films usually noted for TiF_6^{2-} -based LPD baths^{1,9} and clearly illustrates the ability of our ligand-impregnated nanoPPX substrates to influence the structure of the deposited TiO_2 .

Crystallization of amorphous TiO_2 can be induced *via* thermal annealing at temperatures $> \sim 400^\circ\text{C}$.^{32,33} However, these temperatures clearly exceed the $\sim 290^\circ\text{C}$ melting point of our PPX film.³⁴ Therefore, we have examined the annealing behavior of our composites at a temperature of 200°C . The XRD result in Figure 3-7B indicates growth of XRD peaks characteristic of anatase at $\sim 25^\circ$ and $\sim 37^\circ$ after annealing the sample of Figure 3-7A at 200°C for 24 h. Because direct transformation of amorphous TiO_2 to anatase is inhibited at this temperature,^{32,33} our results suggest a mechanism involving consolidation of nanocrystalline domains within the composite during the annealing step. Although the PPX melting point certainly limits the annealing temperature in this work, PPX derivatives exhibiting melting points as high as 420°C ³⁴ are available *via* changes in the nature and number of functional groups present in the [2.2]-*p*-cyclophane precursor, permitting the use of even higher temperatures when necessary for annealing such composites.

3.8. Summary

In summary, we have extended the scope of noncovalent functionalization of nanoPPX films to the fabrication of TiO_2 /nanoPPX hybrid nanostructures using

hexafluorotitanate-boric acid liquid phase deposition (LPD) bath. The key process step involves physisorption onto the nanoPPX surface of a TiO₂-binding aromatic ligand species prior to TiO₂ deposition. The functionality of the ligand controls the physicochemical properties of TiO₂/nanoPPX nanocomposites such as TiO₂ surface coverage, interface adhesion, contact angle *etc.* The presence of a physisorbed ligand in combination with the nanostructured morphology of the nanoPPX film also influences the structure of TiO₂ film deposited. TiO₂ films containing both crystalline anatase and amorphous TiO_x ($x \leq 2$) phases are observed using the LPD bath employed in our experiments. Annealing of the nanocomposites, facilitated by the thermal stability of the underlying nanoPPX films, allows consolidation of the nanocrystalline components of the TiO₂ films.

References

1. Gao, Y. F. & Koumoto, K. *Crystal Growth & Design* **5**, 1983-2017 (2005).
2. Huang, D., Xiao, Z. D., Gu, J. H., Huang, N. P. & Yuan, C. W. *Thin Solid Films* **305**, 110-115 (1997).
3. Shin, H., Agarwal, M., De Guire, M. R. & Heuer, A. H. *Acta Materialia* **46**, 801-815 (1998).
4. Masuda, Y., Sugiyama, T., Lin, H., Seo, W. S. & Koumoto, K. *Thin Solid Films* **382**, 153-157 (2001).
5. Masuda, Y., Jinbo, Y., Yonezawa, T. & Koumoto, K. *Chemistry of Materials* **14**, 1236-1241 (2002).
6. Masuda, Y., Sugiyama, T. & Koumoto, K. *Journal of Materials Chemistry* **12**, 2643-2647 (2002).
7. Masuda, Y., Sugiyama, T., Seo, W. S. & Koumoto, K. *Chemistry of Materials* **15**, 2469-2476 (2003).
8. Yamabi, S. & Imai, H. *Chemistry of Materials* **14**, 609-614 (2002).
9. Koumoto, K., Seo, S., Sugiyama, T., Seo, W. S. & Dressick, W. J. *Chemistry of Materials* **11**, 2305-2309 (1999).
10. Dressick, W. J., Chen, M. S. & Brandow, S. L. *Journal of the American Chemical Society* **122**, 982-983 (2000).
11. Martin, B. D., Brandow, S. L., Dressick, W. J. & Schull, T. L. *Langmuir* **16**, 9944-9946 (2000).

12. Dressick, W. J., Nealey, P. F. & Brandow, S. L. in *Emerging Lithographic Technologies V* (ed. Dobisz, E. A.) 294-305 (SPIE, 2001).
13. Brandow, S. L., Schull, T. L., Martin, B. D., Guerin, D. C. & Dressick, W. J. *Chemistry-a European Journal* **8**, 5363-5367 (2002).
14. Chen, M. S., Dressick, W. J., Schull, T. L. & Brandow, S. L. in *Nanostructure Science, Metrology, and Technology* (eds. Peckerar, M. C., Postek, M. T. & Jr.) 155-159 (SPIE, 2002).
15. Brandow, S. L., Chen, M. S., Dulcey, C. S. & Dressick, W. J. *Langmuir* **24**, 3888-3896 (2008).
16. Demirel, M. C., Boduroglu, S., Cetinkaya, M. & Lakhtakia, A. *Langmuir* **23**, 5861-5863 (2007).
17. Cotton, F. A., G., W., Murillo, C. A. & Bochmann, M. *Advanced Inorganic Chemistry* (John Wiley & Sons, Inc., New York, 1999).
18. He, H. X., Zhang, H. A., Wang, Y. C. & Liu, Z. F. *Molecular Crystals and Liquid Crystals Science and Technology Section a-Molecular Crystals and Liquid Crystals* **337**, 301-304 (1999).
19. Mengistu, T. Z., Goel, V., Horton, J. H. & Morin, S. *Langmuir* **22**, 5301-5307 (2006).
20. Malvadkar, N., Dressick, W. J. & Demirel, M. C. *Journal of Materials Chemistry* **19**, 4796-4804 (2009).
21. Kay, S., Thapa, A., Haberstroh, K. M. & Webster, T. J. *Tissue Engineering* **8**, 753-761 (2002).

22. Pechy, P. et al. *Journal of the Chemical Society-Chemical Communications*, 65-66 (1995).
23. Zhang, X. J., Ma, T. Y. & Yuan, Z. Y. *Journal of Materials Chemistry* **18**, 2003-2010 (2008).
24. Sarkar, K., Laha, S. C., Mal, N. K. & Bhaumik, A. *Journal of Solid State Chemistry* **181**, 2065-2072 (2008).
25. Adolphi, B., Jahne, E., Busch, G. & Cai, X. D. *Analytical and Bioanalytical Chemistry* **379**, 646-652 (2004).
26. Cabeza, A. et al. *Microporous and Mesoporous Materials* **114**, 322-336 (2008).
27. Wagner, C. D., Riggs, W. M., Davis, L. E. & Moulder, J. F. *Handbook of X-ray photoelectron Spectroscopy* (The Perkin-Elmer Corporation, Eden Prairie, MN, 1979).
28. Dupin, J. C., Gonbeau, D., Vinatier, P. & Levasseur, A. *Physical Chemistry Chemical Physics* **2**, 1319-1324 (2000).
29. Goncalves, J. E., Castro, S. C., Ramos, A. Y., Alves, M. C. M. & Gushikem, Y. *Journal of Electron Spectroscopy and Related Phenomena* **114**, 307-311 (2001).
30. Gao, Y. F., Masuda, Y. & Koumoto, K. *Chemistry of Materials* **16**, 1062-1067 (2004).
31. Cetinkaya, M., Malvadkar, N. & Demirel, M. C. *Journal of Polymer Science Part B-Polymer Physics* **46**, 640-648 (2008).
32. Terwilliger, C. D. & Chiang, Y. M. *Journal of the American Ceramic Society* **78**, 2045-2055 (1995).

33. Hague, D. C. & Mayo, M. J. *Journal of the American Ceramic Society* **77**, 1957-1960 (1994).
34. Frados, J. *Modern Plastics Encyclopedia* (McGraw Hill, 1968).

Chapter 4. Mechanism of Noncovalent Ligand Adsorption*

4.1. Introduction

In the previous two chapters, a generalized methodology to prepare nanoPPX-templated hybrid nanostructures *via* noncovalent ligand functionalization was discussed. Based on the structural and chemical characterization of these hybrid nanostructures, a model relating ligand adsorption to noncovalent π - π interactions between the ligand and disordered aromatic polymer chains present at the highly curved surfaces of the PPX nanorods was proposed. It was also established that the morphology of these hybrid nanostructures is profoundly affected by the ligand functionality and/or the adsorption conditions (*i.e.*, aqueous solution *vs.* vapor treatments). Further, it was hypothesized that the conformal nature of metallization of nanoPPX and its high interface strength were due to the deep penetration (along film thickness) of ligand molecules into the nanoPPX structure and the cooperative ligand binding effect, respectively. Analogous metallization (or ceramization) on a conventionally deposited planar PPX film, on the other hand, results in non-continuous patchy deposition, which was attributed to poor ligand adsorption in such a structure due to its compact polymer chain arrangement. As a bottom-line, the metal (or ceramic) growth models, discussed in preceding chapters, suggest that the ligand adsorption phenomenon forms the basis of all the observed characteristics of the hybrid nanostructures and hence demands a closer look.

* Some contents of this chapter are reproduced in part with permission from Malvadkar *et al.*, *Langmuir* **26**, 4382–4391 (2010). DOI: 10.1021/la9034529. Copyright 2010 American Chemical Society.

In this series of studies, we attempt to address the following questions in order to further our understanding of the mechanism for ligand adsorption and metal growth: (1) What is the nature of noncovalent interaction between pyridine and PPX (Section 4.3.1)? (2) What is the effect of PPX morphology (*i.e.*, planar *vs.* nanorod) on pyridine adsorption (Section 4.3.2)? and (3) How does crystallinity of nanoPPX affect pyridine adsorption and subsequent metallization (Section 4.3.3)? Specifically, we contrast the metallization behavior of a nanoPPX film functionalized with an aromatic ligand (*e.g.*, pyridine) with that of a nanoPPX film functionalized with an aliphatic ligand (*e.g.*, amylamine). Next, we study the crystallinity differences between a planar PPX and nanoPPX film using X-ray diffraction (XRD) and relate it to the *in situ* pyridine adsorption data measured by means of a quartz crystal microbalance (QCM). We then closely analyze the nanoPPX and planar PPX structures (*i.e.*, surface area and porosity) by gas physisorption study in order to determine the sites where pyridine adsorption occurs. Finally, pyridine adsorption and subsequent metallization are quantified for nanoPPX films with varying crystallinities using QCM and energy dispersive X-ray spectroscopy (EDX), respectively. Brief discussions on the models used for analyzing the gas physisorption and QCM data are presented in Appendices B and C, respectively.

4.2. Experimental

XRD data was obtained using a Scintag X2 X-ray diffractometer with a Cu K α radiation source and a Si(Li) Peltier cooled detector. The diffraction patterns were taken using grazing angle incidence (incidence angle of 2 degrees) while the detector was scanned from 5 to 45 degrees at a rate of 0.02 degree \cdot s $^{-1}$.

A Micrometrics ASAP 2020 fully-automated volumetric adsorption analyzer was used for N₂ and CO₂ adsorption study on planar and nanoPPX film. Planar and nanoPPX (helical morphology, $\omega = 5$ rpm) films were deposited on glass slides and later delaminated from the substrate. The delaminated films were outgassed in the vacuum degas port of the analyzer for ~ 4 h at 298 K before recording adsorption/desorption data.

QCM experiments were conducted using Maxtek RQCM (Inficon Inc., NY) controller that allows simultaneous resonance frequency (f_s) and resistance (R) monitoring. Pristine quartz crystals coated with Cr/Au electrodes (Appendix C, Figure C-1A) and 5 MHz resonance were purchased from SRS Inc., CA. A layer of octadecanethiol (C18-thiol) self-assembled monolayer (SAM)¹ was grown on the gold electrode before depositing the PPX film onto it. We assume that shear wave generated during oscillation of the crystal pass through the entire thickness of the PPX film.

Pyridine adsorption isotherms were measured for planar and nanoPPX films in vapor phase or aqueous solution phase conditions at 298 K using the experimental setup shown in Figure C-1C in Appendix C. For vapor phase adsorption measurements, a PPX-coated QCM crystal coated with nanoPPX or planar film was horizontally suspended above an aqueous pyridine solution in a tightly sealed vial. During aqueous solution adsorption measurements, the PPX-coated QCM crystal was completely immersed in the solution. The entire assembly was kept in a vibration/acoustic-free isolation chamber. Pyridine was incrementally dosed in the vial to increase the concentration step-wise from 0 M to 1.5 M. The frequency and resistance were allowed to stabilize for at least 2 h before the addition of subsequent dose. The corresponding stabilized frequency (f_s) and

resistance (R) at each dosing step were recorded to plot the adsorption isotherm and $\Delta f_s - \Delta R$ plot.

Annealing of four as-deposited nanoPPX films was carried out in N_2 atmosphere at temperatures 115, 140, 170 and 220 °C on a hot plate for 1 h. Subsequent metallization was carried out using the procedure detailed in Chapter 2. Briefly, samples were treated with 1 M pyridine (aq) for ~48 h and soaked in water for 4 min. PD1 treatment was carried out for 45 min followed by plating in Co bath for 1 min (see Section 5.1.2 in Chapter 5 for preparation procedure for Co plating bath). All treatment steps were timed precisely using a digital stop-watch. After Co plating, the samples were rinsed in water and stored in a vacuum desiccator until required for EDX characterization.

4.3. Results and Discussion

4.3.1. Nature of Noncovalent Interactions

In the preliminary metal growth model, summarized in Chapter 2, it was hypothesized that the primary mode of noncovalent interaction is due to the π - π interactions between pyridine and the aromatic moieties of the PPX film. Unfortunately, the low pyridine levels in the PPX film preclude any direct evidence for the existence of π - π interactions in the system through spectroscopic analysis.² Therefore, our assignment of π - π interactions as the basis for favorable binding of ligand by nanoPPX films is rationalized by the chemical nature of the participating species and experimental observation. We eliminate electrostatic and hydrogen bonding as possible modes of interaction since the PPX structure does not contain functional groups that could support

such interactions with the pyridine ligand. Conventional van der Waals interactions, though certainly present, are too weak in our system to support the strong binding evidenced by the adhesion tests that we observe. Specifically, we tested aliphatic ligands such as amylamine, which are capable of adsorption *via* conventional van der Waals interactions but not π - π interactions. NanoPPX films treated with amylamine did show metallization indicative of adsorption at the nanoPPX surface but could not pass the Scotch[®] tape adhesion test (Figure 4-1, left image). In comparison, nanoPPX films treated with aromatic ligands such as pyridine, 4,4'-diphenyl-2,2'-dipyridyl and 2,2'-bipyridine consistently metallized the nanoPPX surface and exhibited excellent interface strength manifested by the Scotch[®] tape adhesion test (Figure 4-1, right image).

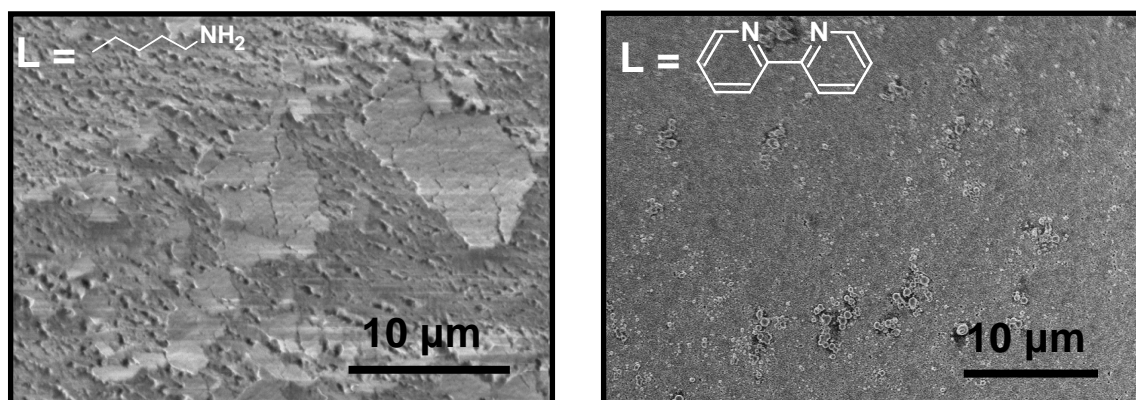


Figure 4-1. SEM image of Ni layer deposited on nanoPPX film functionalized with 1 M aqueous solution of amylamine (left) and 0.1 M aqueous solution of 2,2'-bipyridine (right). Other metallization parameters: PD1 treatment time = 45 min. Ni plating time = 15 min. The Ni layers on both films were subjected to the Scotch[®] tape test before SEM characterization. Left image reproduced with permission from Malvadkar *et al.*, *Langmuir* **26**, 4382–4391 (2010). DOI: 10.1021/la9034529. Copyright 2010 American Chemical Society.³

Ligand adsorption studies conducted using a quartz crystal microbalance (QCM) show the frequency change for pyridine adsorption is two orders of magnitude higher compared to amylamine adsorption (Figure 4-2). Since frequency shift scales directly to the surface mass density of adsorbent (Equation C-1 in Appendix C),⁴ the quantity of pyridine entering the PPX film is two orders of magnitude higher than amylamine. This again suggests that the stronger π - π interaction between the aromatic ligand such as pyridine and the aromatic backbone of the PPX polymer is the primary mode of the noncovalent interaction that binds the ligand molecules, resulting in a stable metal layer.

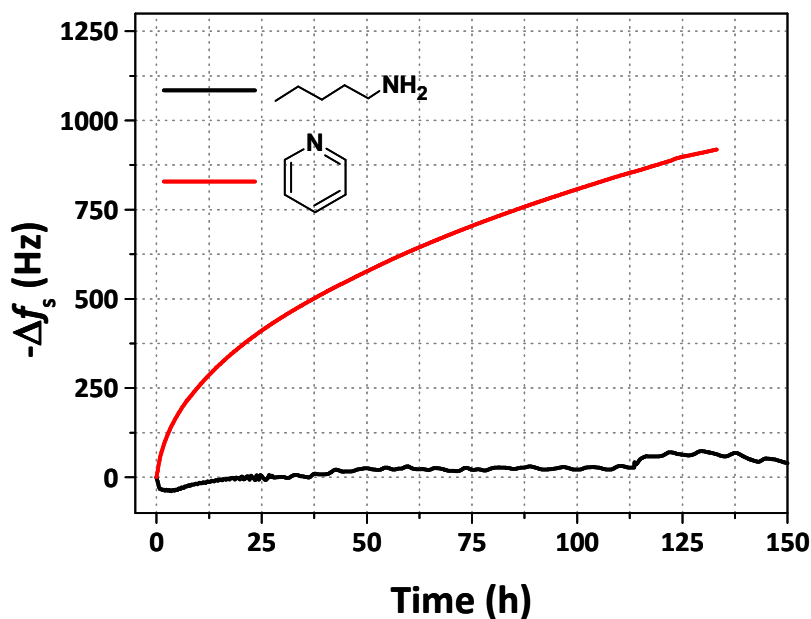


Figure 4-2. Adsorption of pyridine (aq, 1 M) and amylamine (aq, 1 M) in a nanoPPX film monitored using a QCM. Reproduced with permission from Malvadkar *et al.*, *Langmuir* **26**, 4382–4391 (2010). DOI: 10.1021/la9034529. Copyright 2010 American Chemical Society.³

4.3.2. Effect of PPX Morphology on Pyridine Adsorption

The preliminary metal growth model postulated that the high curvature of the PPX nanorods in a nanoPPX film results in larger number of sites for pyridine adsorption relative to a planar PPX film.⁵ Subsequently, a nanoPPX film has larger number of N-sites on the surface where PD1 particles can bind in sufficient quantities to support continuous metal growth, whereas the low surface density of N-sites on a planar PPX surface cannot bind enough PD1 leading to the contrasting metallization behavior. We now undertake X-ray diffraction (XRD), *in situ* pyridine adsorption (using QCM) and gas physisorption studies to further understand the mechanism for pyridine incorporation into these polymer films.

PPX at room temperature exhibits a monoclinic α -phase with $a = 596$ pm, $b = 1269$ pm, c (chain axis) = 666 pm, and $\beta = 135.2$.⁶ As the distance between two adjacent aromatic groups of the monoclinic PPX chain is 4.17 Å,⁷ while the stacking distance between the pyridine and benzene group is 3.7 Å,^{8,9} it is unlikely that a pyridine molecule forms π - π stacking interactions in the crystalline regime. Although both planar PPX and nanoPPX films possess crystalline regions, XRD experiments (Figure 4-3) signify the largely amorphous nature of the nanoPPX film. The large surface area and the high curvature of the PPX nanorods in a nanoPPX film result in polymer chains that are highly disordered at the surface. Specifically, the disordered polymer chains at the surface provide a mechanism to increase the accessibility of pyridine molecules into the nanoPPX polymer, consistent with the preliminary metal growth model.

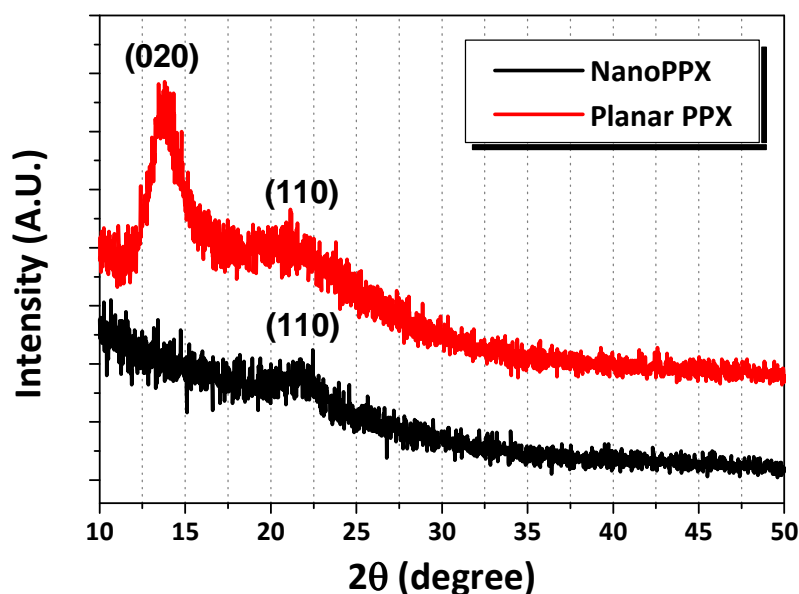


Figure 4-3. X-ray diffraction (XRD) patterns of nanoPPX and planar PPX films. Reproduced with permission from Malvadkar *et al.*, *Langmuir* **26**, 4382–4391 (2010). DOI: 10.1021/la9034529. Copyright 2010 American Chemical Society.³

In contrast, the XRD pattern of planar PPX film (Figure 4-3) shows a distinct peak at $2\theta = 13.95^\circ$ indicative of a (020) reflection from the monoclinic α -phase. The XRD pattern of planar PPX film indicates higher crystallinity compared to a nanoPPX film and preferential orientation of the monoclinic crystallites with the b -axis perpendicular to the surface of the substrate. A planar PPX film has lower surface area and a more compact and regular arrangement of the polymer chains compared to the chains in a nanoPPX film. Consequently, the pyridine adsorption rate in a planar PPX film is much lower compared to the rate of adsorption in a nanoPPX film, as illustrated by QCM adsorption kinetics curves (Figure 4-4).

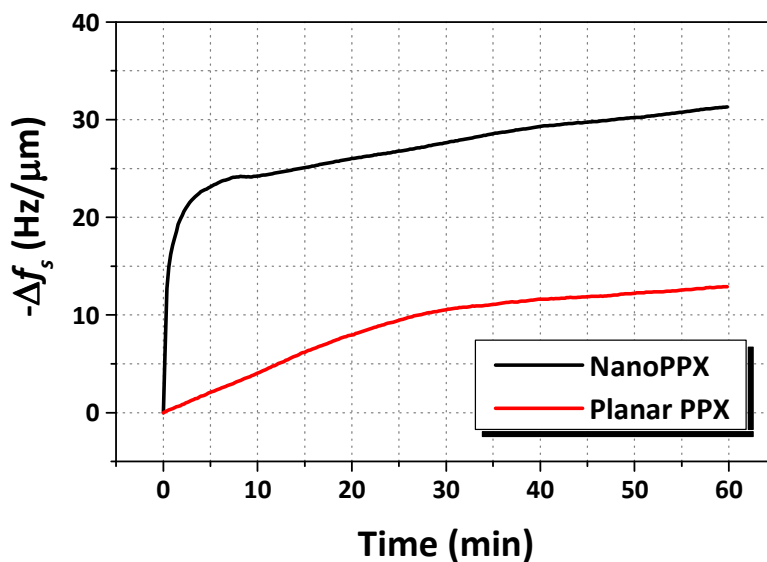


Figure 4-4. Vapor phase adsorption of 10 mM pyridine on nanoPPX and planar PPX films monitored using QCM.

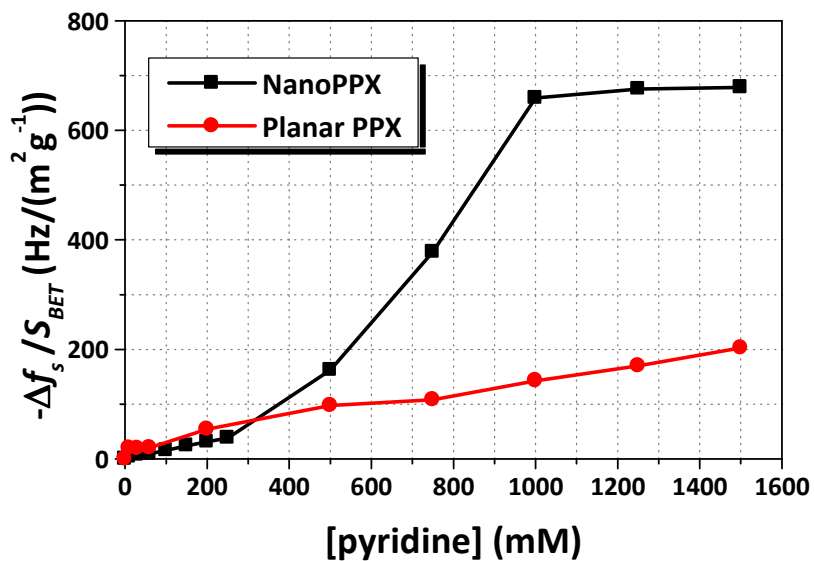


Figure 4-5. Vapor phase pyridine adsorption isotherm on nanoPPX and planar PPX films. The frequency change, Δf_s , was normalized with the BET surface area, S_{BET} , of the two films.

The higher rate of adsorption of pyridine in a nanoPPX film also results in a higher equilibrium concentration, evident in the vapor phase adsorption isotherm shown in Figure 4-5. The pyridine adsorption isotherms were obtained by normalizing the frequency shifts (Δf_s) with the BET surface areas of the respective films, which were calculated from Equation B-1 in Appendix B using N_2 adsorption isotherm data (Figure 4-6). The pyridine adsorption isotherm of a nanoPPX film shows three distinct segments, while that of a planar PPX film exhibits a continuous monotonic increase of pyridine coverage. The initial segment ($0 \text{ mM} < [\text{pyridine}] < 412 \text{ mM}$) of the adsorption isotherm of a nanoPPX film is nearly linear and coincides with the isotherm of a planar PPX film, implying adsorption on the surface. At $[\text{pyridine}] \approx 412 \text{ mM}$, a steep increase in pyridine adsorption is observed in the nanoPPX film, which can be attributed to the condensation of pyridine in the porous structures of nanoPPX.¹⁰ In contrast, no such a behavior is observed for planar PPX film due to the lack of such pores for pyridine condensation. The final segment ($[\text{pyridine}] > 1\text{M}$) of the adsorption isotherm on the nanoPPX film is nearly linear as a result of the build-up of pyridine molecules on the outermost surface of the film culminating in adsorption saturation.

The saturated Δf_s is equivalent to $0.46 \text{ cm}^3/\text{g}$ of pyridine in the nanoPPX film obtained by applying the Sauerbrey's equation (Equation C-1 in Appendix C). The contrasting features of the pyridine adsorption isotherms of the two films stem from the difference in their pore structures, resulting in the observed difference in the metallization behavior, as described by the preliminary metal growth model. We now present a gas

physisorption study of the two films in order to unequivocally determine the precise sites where pyridine adsorption occurs in the two films.

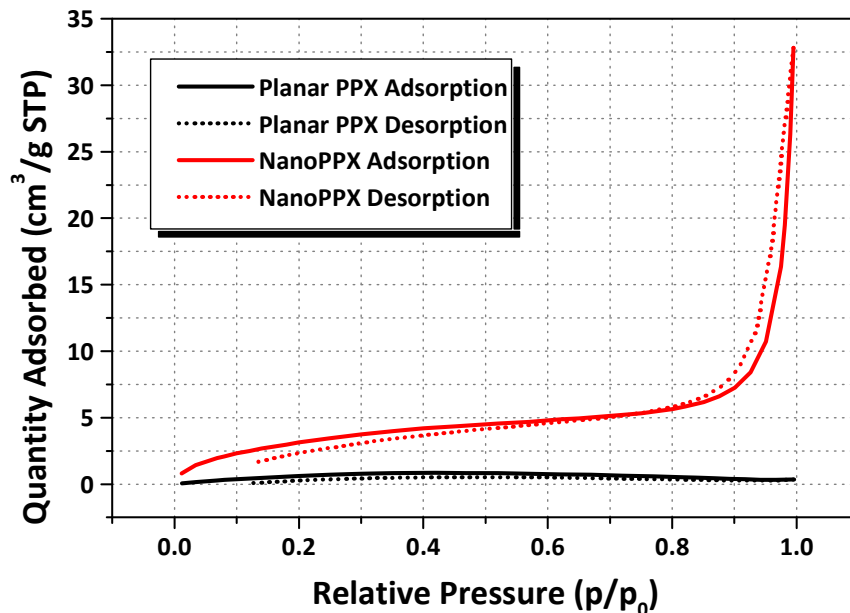


Figure 4-6. N₂ adsorption and desorption isotherms at 77.35 K on planar PPX and nanoPPX films.

N₂ adsorption and desorption isotherms of planar PPX and nanoPPX films (Figure 4-6) were used to calculate BET surface area and mesopore size distribution in the two films. The cumulative surface area and pore volume data obtained from the N₂ isotherms are summarized in Table 4-1. Mesopore size distribution (Figure 4-7) using BJH algorithm¹¹ is obtained directly from the ASAP 2020 operating software. A planar PPX film exhibits a cumulative mesopore volume of 2.0×10^{-4} cm³/g, while a nanoPPX film, on the other hands, shows a broad size distribution of mesopores centered at ~35 nm resulting in a cumulative mesopore volume of 0.0476 cm³/g. The mesopores in a

nanoPPX film are, most likely, the inter-nanorod spacing created by the aligned nanorod morphology and are responsible for the observed hysteresis due to capillary condensation at $p/p_0 \sim 0.85$ in the N_2 isotherm (Figure 4-6). In addition, the mesopore size distribution shows a steep increase near the micropore regime (~ 3 nm) signifying the presence of micropores in a nanoPPX film. However, due to the inapplicability of the Kelvin equation (Equation B-3 in Appendix B), on which the BJH algorithm is based, in the micropore regime (*i.e.*, ≤ 2 nm), pore size distribution for size less than 2 nm cannot be calculated using the BJH method. We therefore have to resort to CO_2 adsorption isotherm to evaluate the microporosity in the nanoPPX film.

Table 4-1. Surface area and porosity data from N_2 and CO_2 adsorption isotherm.

	BET surface area (S_{BET}, m^2/g)^a	BJH total mesopore volume (cm^3/g)^a	Micropore limiting volume (Q_0, cm^3/g)^b	Micropore limiting area (m^2/g)^b
Pristine Planar PPX	3.1574	0.0002	— ^c	— ^c
Pristine NanoPPX	12.6835	0.0476	0.433	1129.7
PYR(aq)-NanoPPX	—	—	0.021	51.503
PYR(vap)-NanoPPX	—	—	— ^c	— ^c

^a Calculated from the adsorption branch of the N_2 isotherm. ^b Obtained by applying DA equation on CO_2 adsorption isotherm. ^c No adsorption data could be obtained from these samples, *i.e.*, no CO_2 adsorption occurs.

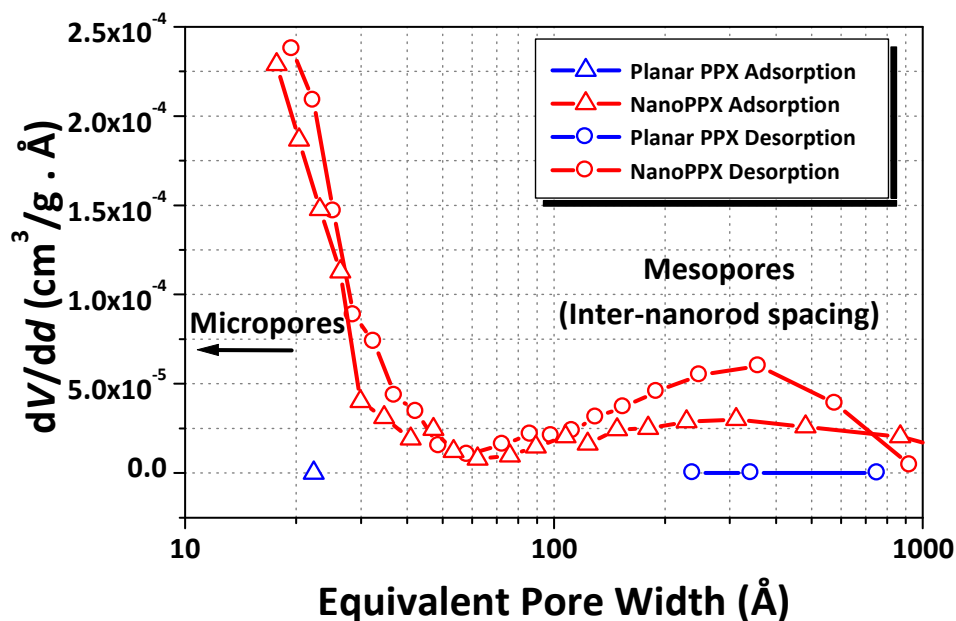


Figure 4-7. Differential pore volume distribution obtained from BJH method using N₂ isotherm data on planar and nanoPPX films at 77.35 K.

CO₂ adsorption at 273.15 K was measured in the range $0.00 \leq p/p_0 \leq 0.01$ (corresponding to $p = 0$ to 266 torr) on four films: pristine nanoPPX, pristine planar PPX, nanoPPX film functionalized with aqueous pyridine and nanoPPX film functionalized with vapor pyridine. In this pressure range, the primary mode of adsorption occurs *via* the micropore filling mechanism. Two of these four films, namely pristine planar and nanoPPX film functionalized with vapor pyridine did not show any CO₂ adsorption, indicating absence of micropores available in these samples. CO₂ adsorption isotherms of pristine nanoPPX and pyridine(aq)-functionalized nanoPPX are shown in Figure 4-8. CO₂ adsorption in a pristine nanoPPX film is clearly higher compared to that in pyridine(aq)-functionalized nanoPPX indicating larger cumulative micropore volume in a

pristine film. The data also suggests that pyridine molecules are able to infiltrate the micropores in a nanoPPX film thereby reducing the cumulative micropore volume. Besides, reduced adsorption in pyridine(aq)-functionalized nanoPPX and the absence of adsorption in pyridine(vap)-functionalized nanoPPX imply that pyridine is able to resist (completely in pyridine(vap)-functionalized nanoPPX and partially in pyridine(aq)-functionalized nanoPPX) vacuum degassing performed prior to CO₂ adsorption, consistent with previously reported observation.⁵

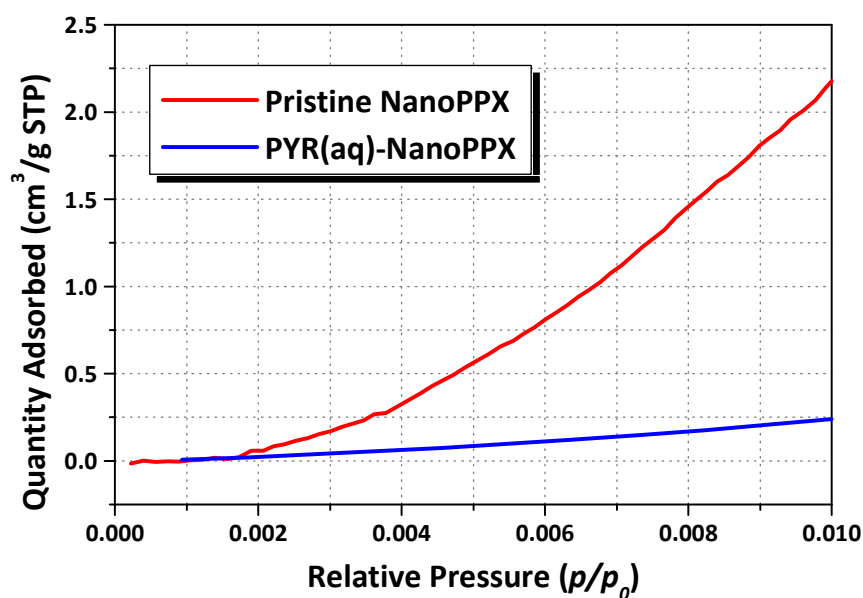


Figure 4-8. CO₂ adsorption isotherm on pristine and pyridine-functionalized nanoPPX film. Pyridine functionalization was carried out by treatment with 1 M pyridine (aq) solution for ~48 h.

A plausible explanation for the lack of CO₂ adsorption in pyridine(vap)-functionalized nanoPPX can be based upon the pyridine orientation at the nanoPPX surface. In the refined metal growth model described in Chapter 2, we argued that

pyridine in pyridine(vap)-functionalized nanoPPX randomly orients itself during adsorption, while the alignment of pyridine in pyridine(aq)-functionalized nanoPPX is non-random such that the pyridyl N-sites preferentially orient themselves at the nanoPPX surface.³ Assuming the accuracy of the model, surface basicity induced by pyridine adsorption is higher in pyridine(aq)-functionalized nanoPPX due to the presence of larger number of pyridyl N-sites at the nanoPPX surface compared to that in pyridine(vap)-functionalized nanoPPX. CO₂ is known to have a preferential affinity towards basic sites on the surface and is routinely used as a probe molecule for characterizing surface basicity of heterogeneous catalysts.¹²⁻¹⁴ The occurrence of CO₂ adsorption in pyridine(aq)-functionalized nanoPPX and the lack thereof in pyridine(vap)-functionalized nanoPPX therefore corroborates the assumptions of the refined metal growth model.

In order to calculate the cumulative micropore volume in the nanoPPX film, the Dubinin–Astakhov (DA) model (see Section B.3. in Appendix B) was applied to the CO₂ adsorption data. Figure 4-9 shows the linearized DA plot for pristine and pyridine(aq)-functionalized nanoPPX films. The y-intercept of the extrapolated linearized DA plot yields the limiting micropore volume (Q_0) of the two films. As expected, the pristine nanoPPX film exhibits a higher Q_0 value compared to a pyridine(aq)-functionalized nanoPPX film (Table 4-1) due to pyridine-occupied micropores in a pyridine(aq)-functionalized nanoPPX film. The limiting micropore volume of a pristine nanoPPX film (0.433 cm³/g) is close to the pyridine condensate volume (0.46 cm³/g, see Section 4.3.2) and an order of magnitude higher compared to the cumulative BJH mesopore volume (0.0476 cm³/g, Table 4-1), which confirms that pyridine adsorption proceeds *via* the micropore filling mechanism.

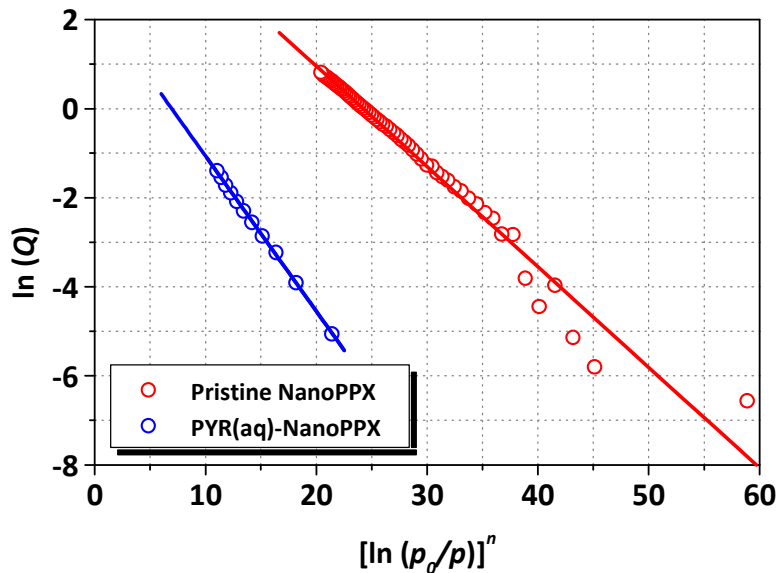


Figure 4-9. Linearized DA plot obtained from CO₂ adsorption data. Exponent, n , was determined empirically and equals 1.9800 and 1.5796 for pristine and pyridine (aq)-functionalized nanoPPX films, respectively.

Differential pore size distribution from CO₂ adsorption data on the two films, shown in Figure 4-10, is obtained by solving the inverse Stoeckli integral equation (Equation B-9 in Appendix B) and assuming Gaussian pore size distribution.¹⁵ The differential pore size distribution obtained from CO₂ adsorption data juxtaposes well with that obtained from the BJH model (Figure 4-7), verifying the accuracy of the two methods. As a bottom line, we can conclude that the structure of a nanoPPX film is dominated by micropores of ~1–2 nm width; these micropores, designated by various terminologies such as open-pore structure, “nanocavities”, surface disorder *etc.* in our previous publications,^{3,5,16} are sites where pyridine adsorption occurs.

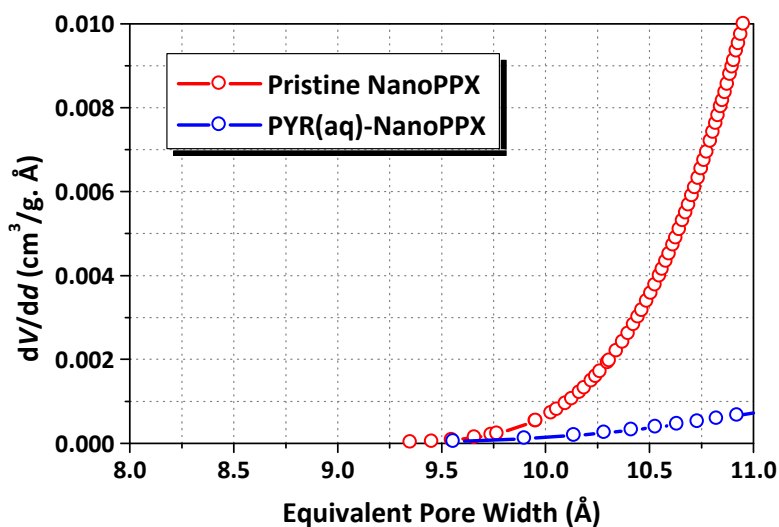


Figure 4-10. Differential pore size distribution obtained from CO₂ adsorption data on pristine and pyridine (aq)-functionalized nanoPPX.

4.3.3. Effect of Annealing on Pyridine Adsorption and Metallization

In the previous section, we concluded that the amorphous regions, characterized by the presence of micropores, are sites where pyridine adsorption occurs. In this section, we extend our present understanding of the relationship between the crystallinity of a nanoPPX film and pyridine intake by including the effect of annealing on pyridine adsorption and subsequent metal growth. QCM is used to monitor aqueous pyridine adsorption in nanoPPX films with varying crystallinities. We then metallize these films by electroless Co plating and quantify the plating rate using EDX. Thereafter, we correlate the two quantifications by presenting an extended metal growth model to explain the experimental data.

Figure 4-11 shows XRD patterns of annealed and as deposited samples of nanoPPX. A progressive increase in the magnitude of the peaks from (110) and (020) reflections from monoclinic α -phase of PPX can be observed as the annealing temperatures increase. Annealing at temperatures less than the melting temperature of PPX ($T_m = 563$ K) on planar counterparts also show similar increase in the peak magnitude of the Bragg reflections.¹⁷ Such increase in the magnitude of Bragg peaks is the consequence of enlargement of crystalline domains in the polymer film due to chain reorganization at higher temperatures. The enlargement in the crystalline domains is also associated with a decrease in the micropore size, as noted in Section 4.3.2.

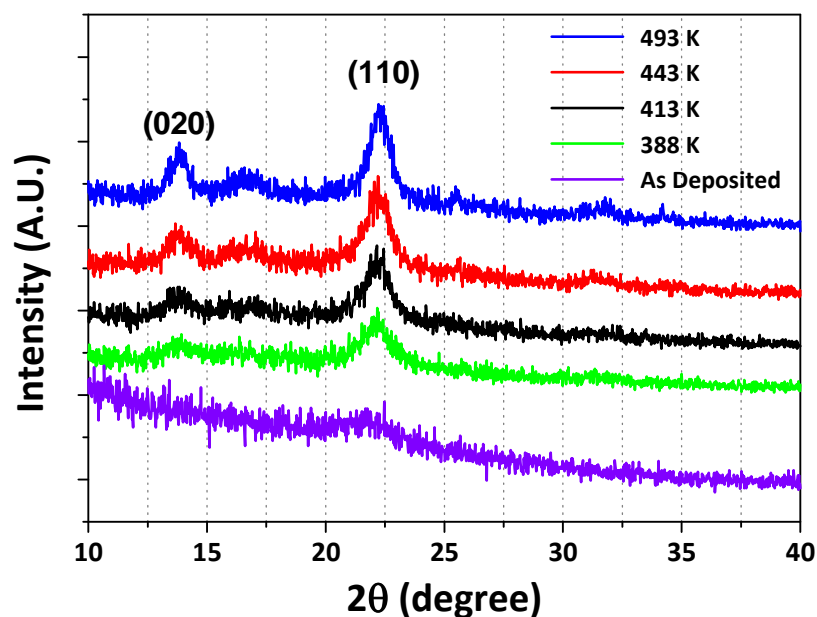


Figure 4-11. XRD pattern of four distinct nanoPPX films annealed at 388, 413, 443 and 493 K per the procedure described in Section 4.2. XRD pattern of an as-deposited nanoPPX film is shown for comparison.

Figure 4-12A shows frequency shifts (Δf_s) for annealed and as-deposited nanoPPX samples submerged step-by-step in pyridine (aq) solutions with progressively higher concentrations. In this case, Δf_s measured by the QCM monitor arises from two components, as noted in Equation C-3 in Appendix C. The first component is the contribution from the rigid or stable mass adsorption on the nanoPPX surface. The pyridine adsorption in micropores can be assumed to resonate in unison with the crystal-nanoPPX assembly; this pyridine can therefore be considered as a rigid mass bound on the surface. In addition, there is a viscous component to the frequency shift due to contact of the surface with a Newtonian liquid (*cf.* pyridine solution). The plot of Δf_s versus [pyridine] (Figure 4-12A) for all samples closely resembles with analogous plot for vapor pyridine adsorption (Figure 4-5), illustrating adsorption by the pore-filling mechanism. Furthermore, the point at which an abrupt increase in Δf_s occurs varies with the annealing temperature. For instance, as-deposited nanoPPX sample exhibits the abrupt increase in Δf_s at [pyridine] \approx 495 mM, while a similar increase in Δf_s occurs at [pyridine] \approx 350 mM for a nanoPPX sample annealed at 493 K. The concentration (or relative pressure) at which such an inflection point occurs is a relative measure of the size of the micropores; inflection point at lower concentration (or relative pressure) values indicates smaller micropore size, and *vice versa*.¹⁸ Therefore, the higher crystallinity induced by annealing is accompanied by a decrease in the microporosity in a nanoPPX film. In addition to Δf_s , equivalent resistance change (ΔR) was measured simultaneously to gauge the dissipation loss of the QCM vibration arising from the liquid contact (Figure 4-12B). The ΔR versus [pyridine] plots clearly suggest higher dissipation losses for annealed samples, signifying the presence of weakly bound pyridine or pyridine build-up on the external surface.

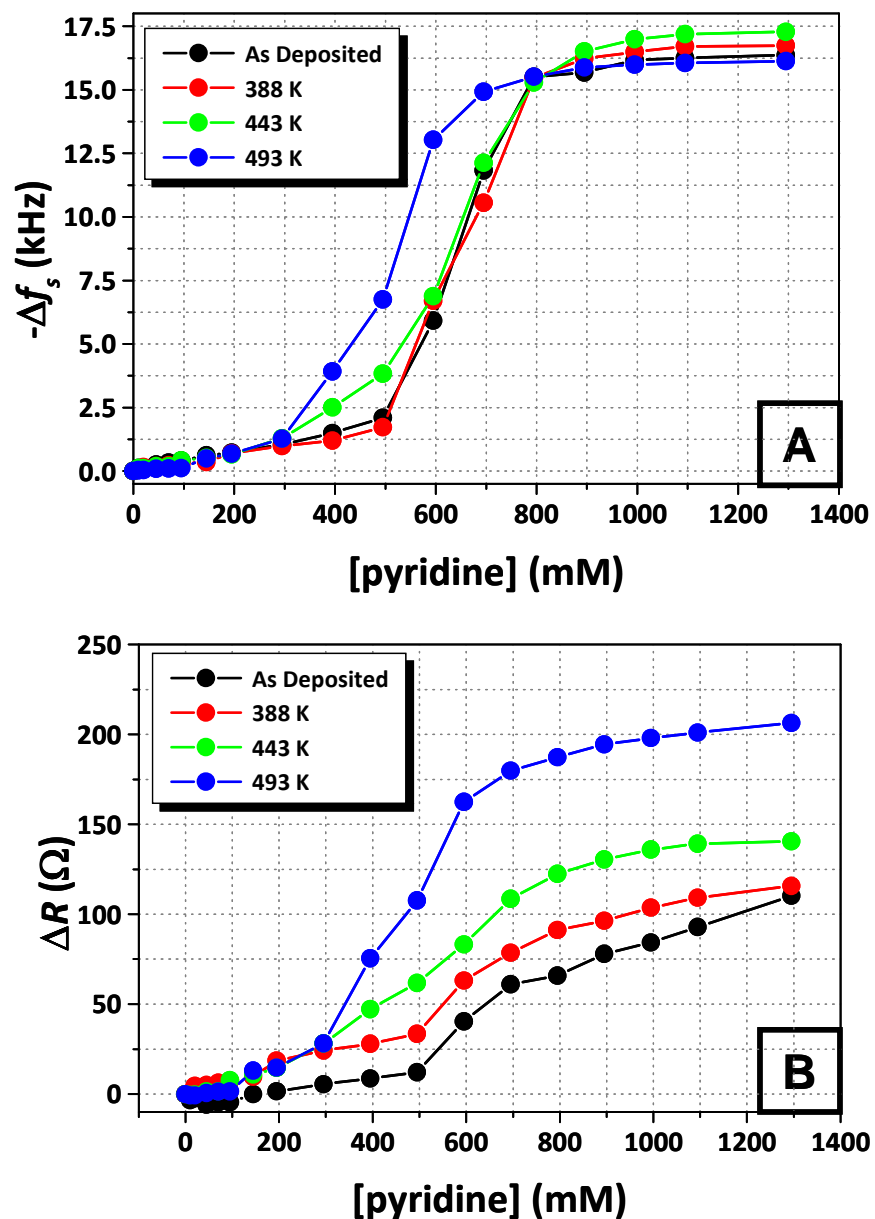


Figure 4-12. Plot of (A) equilibrium frequency shifts (Δf_s) and (B) equivalent resistance change (ΔR) against pyridine (aq) concentration. Three films were annealed at 388, 443, and 493 K prior to QCM experiments, per the procedure described in Section 4.2

A plot of Δf_s versus ΔR for all samples allows a clear distinction between the contribution from rigidly adsorbed pyridine (*i.e.*, pyridine filled micropores) and weakly bound pyridine (Figure 4-13). For an as-deposited nanoPPX sample, progressively higher slope in the Δf_s - ΔR plot till $\Delta R \approx 62 \Omega$ indicates increase in the rigidity of pyridine as it impregnates the micropores. Beyond this point (*i.e.*, $\Delta R > 62 \Omega$), the slope of the curve abruptly decreases marking the saturation of micropore filling and a subsequent rise in the viscous loading component due to pyridine build-up on the external surface. Furthermore, as annealing temperature increases, steepness of the initial rise in the slope of the Δf_s - ΔR progressively decreases, signifying diminishing Δf_s component of rigid pyridine adsorption.

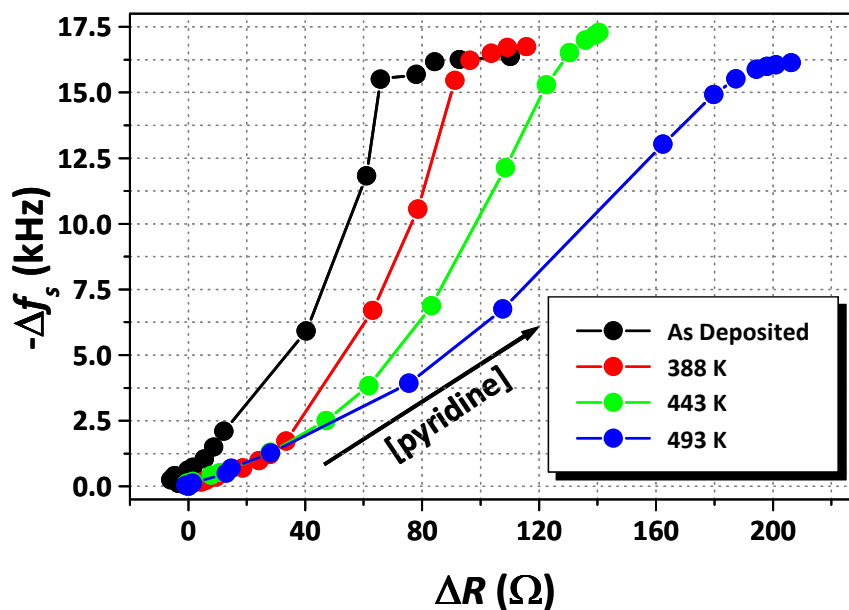


Figure 4-13. Plot of frequency shifts (Δf_s) against equivalent resistance change (ΔR). Three nanoPPX coated QCM crystals were annealed at 388, 443, and 493 K prior to QCM experiments, per the procedure described in Section 4.2.

Post-metallization, the amount of metal (*i.e.*, Co) deposited relative to the underlying polymer was quantified by measuring the Co/C (at. %) ratio, obtained from EDX (Figure 4-14). All samples were treated with 1 M pyridine (aq) solution for 48 h and rinsed in DI water for 4 min prior to Co plating for 1 min. Co/C ratios for the first three samples (*i.e.*, as-deposited, 388 and 413 K annealed samples) lie in the range 0.25 – 0.3. In contrast, samples annealed at higher temperatures (*i.e.*, 443 and 493 K) show a lower (less than 0.15) Co/C ratio, implying a slower plating rate relative to the first three samples.

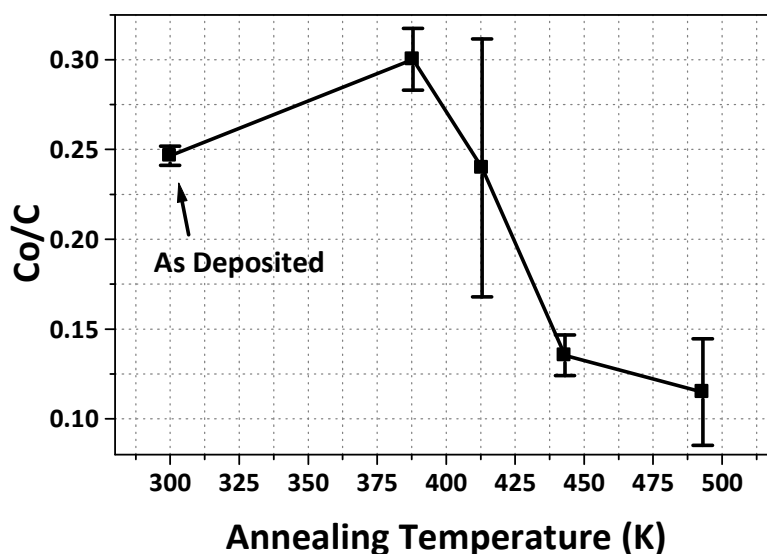
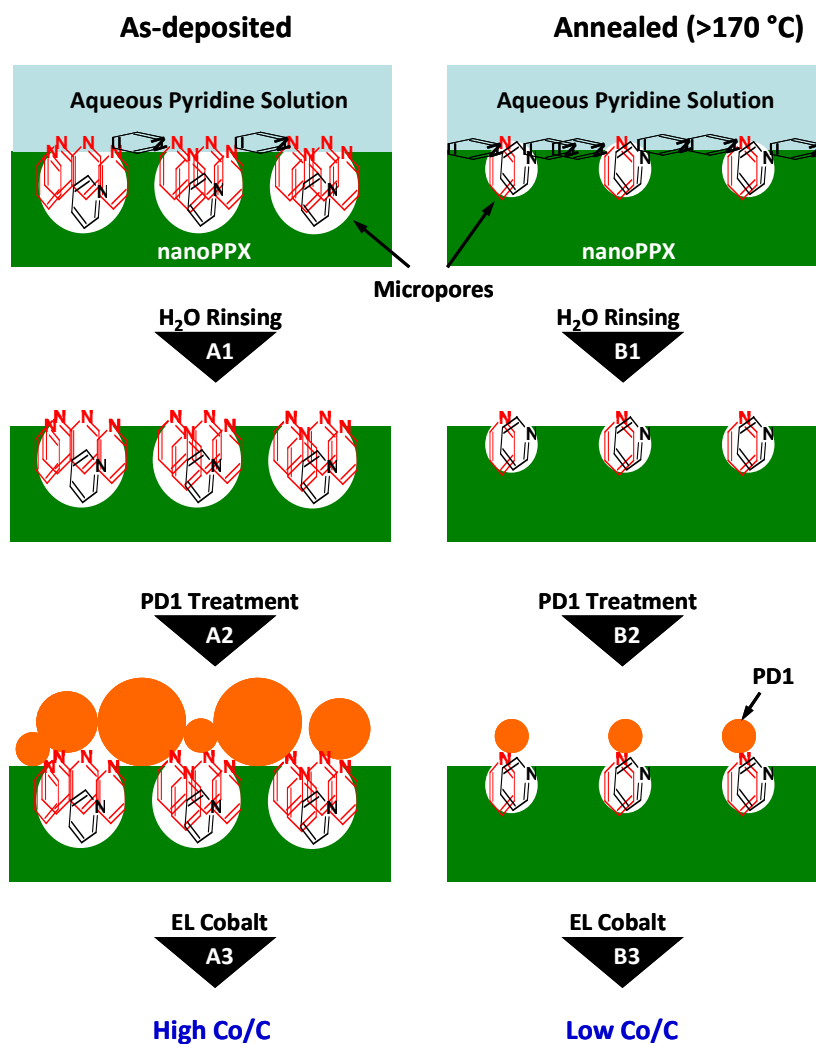


Figure 4-14. Plot of Co/C (at. % ratio) against annealing temperature of nanoPPX film. Refer to Section 4.2 for experimental details.

The pyridine adsorption and subsequent metallization behavior can be explained by means of a micropore model, illustrated in Scheme 4-1. The presence of larger amorphous regions or micropores in an as-deposited nanoPPX allows adsorption of pyridine in large quantities into these sites (Scheme 4-1, Path A). In contrast, annealed

nanoPPX films have increased crystallinity and constricted micropores, restricting the access for rigid pyridine adsorption (Scheme 4-1, Path B). Furthermore, the crystalline regions on the surface of annealed nanoPPX are sites where pyridine build-up is expected, resulting in greater energy dissipation in these samples. After the rinsing step, this build-up of weakly bound pyridine is removed, while the rigidly bound pyridine in the micropores remains in the nanoPPX film. Consequently, the residual pyridine in an as-deposited nanoPPX is higher compared to that in annealed counterparts after the rinsing step. After PD1 treatment, samples with higher residual pyridine will bind larger PD1 nanoparticles due to the relatively high surface density of accessible N-sites on the surface. Subsequently, the high density of PD1 nanoparticles is capable of binding a dense layer of Co particles that is manifested in the observed EDX results. On the other hand, fewer and smaller PD1 nanoparticles will bind on samples with smaller amounts of residual pyridine. Consequently, the Co particles deposited on these samples are sparsely distributed resulting in a lower Co/C ratio.

From the above model, it appears that the plating rate remains unaffected by annealing at low temperatures (*i.e.*, less than 413 K), possibly due to the unchanged micropore structure and/or crystallinity at the surface. As a result, the large amount of residual pyridine is able to bind a dense layer of Co particles, as noted above. At higher annealing temperatures (*i.e.*, greater than 413 K), however, the crystallinity at the surface increases resulting in constricted micropores that restrict rigid pyridine adsorption. Consequently, the plating rate markedly decreases in these samples, evident in the EDX results.



Scheme 4-1. Cartoon showing effect of annealing on metal deposition rate. Green block represents crystalline domains, while the white areas denote the surface amorphous domains or micropores in the nanoPPX film that can be accessed by ligand molecules. Path A and B show electroless metallization *via* noncovalent ligand functionalization on as-deposited and annealed (at temperatures higher than 170 °C) nanoPPX films, respectively. Pyridine molecules available for PD1 binding are shown in red (N-sites at the nanoPPX surface), while those which are unavailable are shown in black (N-sites not at the nanoPPX surface or weakly bound pyridine at the nanoPPX surface).

4.4. Summary

In this chapter, we discussed, in detail, the mechanism for pyridine incorporation into a nanoPPX film. Pyridine adsorption in a nanoPPX film is facilitated by the formation of π - π interactions with aromatic moieties in the polymer chain. NanoPPX films treated with an aliphatic ligand such as amylamine, although, do show metallization, the metal layer however cannot sustain the Scotch[®] tape adhesion test, as expected, due to the presence of weaker van der Waals interactions.

XRD results demonstrate that nanoPPX structure has higher chain disorder relative to a planar film. Consequently, a nanoPPX film demonstrates a significantly higher rate of pyridine adsorption and an equilibrium concentration, consistent with the preliminary metal growth model. Further analysis using gas physisorption study reveal that a nanoPPX film is dominated by micropores of size \sim 1–2 nm. In other words, pyridine adsorption and stabilization occurs into these micropores that represents the chain disorder on the curved nanorod surface, as previously hypothesized.^{3,5} In comparison, a planar film shows significantly lower micropore volume; this disparity in the porosity of the two films is responsible for the observed difference in pyridine intake, leading to their contrasting metallization behavior. Furthermore, the refined metal growth model described in Chapter 2 which proposes that pyridine orientation at the nanoPPX surface depends on its adsorption condition (vapor phase *vs.* aqueous solution treatment) is also supported by the CO₂ adsorption data.

We tested our interpretation of the relationship between the porosity (or crystallinity) of a nanoPPX film and pyridine intake by measuring pyridine adsorption in nanoPPX films with varying crystallinities and subsequently quantifying the metal

deposited on them. As expected, pyridine adsorption is more “rigid” in as-deposited nanoPPX film compared to that in annealed counterparts due to the higher accessibility of pyridine into the micropores of an as-deposited nanoPPX. EDX results further reveal that a more “rigid” adsorption of pyridine, as in the case of an as-deposited film, leads to a denser metal layer on the nanoPPX surface, consistent with the metal growth model. In contrast, nanoPPX films annealed at high temperatures (*i.e.*, greater than 413 K) show relatively higher proportion of weakly bound pyridine, due to the constriction of micropores, which is easily removed in the subsequent rinsing step. Metal growth in annealed nanoPPX films is therefore slower and is manifested in the EDX results.

References

1. Ishida, T. et al. *Langmuir* **14**, 2092-2096 (1998).
2. Yang, D. Q., Rochette, J. F. & Sacher, E. *Journal of Physical Chemistry B* **109**, 4481-4484 (2005).
3. Malvadkar, N. A., Sekeroglu, K., Dressick, W. J. & Demirel, M. C. *Langmuir* **26**, 4382-4391 (2010).
4. Sauerbrey, G. *Zeitschrift Fur Physik* **155**, 206-222 (1959).
5. Demirel, M. C., Cetinkaya, M., Singh, A. & Dressick, W. J. *Advanced Materials* **19**, 4495-4499 (2007).
6. Cetinkaya, M., Malvadkar, N. & Demirel, M. C. *Journal of Polymer Science Part B-Polymer Physics* **46**, 640-648 (2008).
7. Senkevich, J. J. & Desu, S. B. *Polymer* **40**, 5751-5759 (1999).
8. Gao, S., Huo, L.-H., Shu, H. & Ng, S. W. *Acta Crystallographica Section E* **61**, m389-m391 (2005).
9. Harrowfield, J. M., Lugan, N., Shahverdizadeh, G. H., Soudi, A. A. & Thuery, P. *European Journal of Inorganic Chemistry*, 389-396 (2006).
10. Qiao, S. Z., Bhatia, S. K. & Zhao, X. S. *Microporous and Mesoporous Materials* **65**, 287-298 (2003).
11. Barrett, E. P., Joyner, L. G. & Halenda, P. P. *Journal of the American Chemical Society* **73**, 373-380 (1951).
12. Srivastava, R., Srinivas, D. & Ratnasamy, P. *Microporous and Mesoporous Materials* **90**, 314-326 (2006).

13. Lavalley, J. C. *Catalysis Today* **27**, 377-401 (1996).
14. Philipp, R. & Fujimoto, K. *Journal of Physical Chemistry* **96**, 9035-9038 (1992).
15. Stoeckli, H. F. *Journal of Colloid and Interface Science* **59**, 184-185 (1977).
16. Malvadkar, N., Dressick, W. J. & Demirel, M. C. *Journal of Materials Chemistry* **19**, 4796-4804 (2009).
17. Surendran, G., Gazicki, M., James, W. J. & Yasuda, H. *Journal of Polymer Science Part a-Polymer Chemistry* **25**, 2089-2106 (1987).
18. Storck, S., Bretinger, H. & Maier, W. F. *Applied Catalysis a-General* **174**, 137-146 (1998).

Chapter 5. Applications

Until now, we established a generalized approach to synthesize hybrid nanostructures of metals and ceramics on quasi-periodic, aligned nanorods of PPX *via* noncovalent ligand functionalization. These hybrid nanostructures are characterized by high surface area, strong interface strength and metal (or ceramic) growth that mimics the underlying PPX nanorod morphology. We now attempt to employ these attractive structural properties of the hybrid nanostructures in three cutting-edge applications. First, we exploit the high surface area of metal/nanoPPX in building catalysts for hydrogen production from sodium borohydride decomposition (Section 5.1). Next, we utilize the conformal nature of the metal layer and its derived quasi-periodicity in fabricating Ag/nanoPPX-based SERS platforms for biodetection (Section 5.2). Finally, we present a preliminary investigation that explores the prospects of TiO₂/nanoPPX as orthopaedic implant coatings (Section 5.3).

5.1. Catalyst for Hydrogen Production

5.1.1. Introduction

The development of sustainable, environment-friendly, and low-cost energy sources is undoubtedly the greatest challenge of the twenty-first century. Despite the soaring prices of hydrocarbon fuels, alternative energy technologies of today are prohibitively expensive for a complete replacement of existing fossil-fuel technologies. Fortunately, the development of nanoscience and nanotechnology in the past two decades

has brought fascinating breakthroughs in alternative energy technologies, notably photovoltaics, batteries and fuel cells. Fuel cells, in particular, are now on the verge of commercialization in transportation applications, albeit certain issues still remain to be resolved. These issues include cost associated with precious metal loading in the catalytic electrodes, poor ionic conductivity of the membrane over entire humidity range and low temperatures (up to -40 °C), poor chemical and mechanical stability of the membrane with cycling, and hydrogen storage, among others.

Table 5-1. DOE-established targets for on-board hydrogen storage systems.¹

Targets	2010	2015	Ultimate
Net gravimetric capacity	4.5 wt.% ^a (1.5 kWh/kg)	5.5 wt.% ^a (1.8 kWh/kg)	7.5 wt.% (2.5 kWh/kg)
Net volumetric capacity	28 g/L ^a (0.9 kWh/L)	40 g/L ^a (1.3 kWh/L)	70 g/L (2.3 kWh/L)
Fuel charging rate	1.2 kg/min	1.5 kg/min	2.0 kg/min
Fuel discharging rate	0.02 g/s	0.02 g/s	0.02 g/s
Cost of storage	\$4/kWh (\$133/kg.H ₂)	\$2/kWh (\$67/kg.H ₂)	TBD

^a Revised targets established in 2009. 1 kg of H₂ \equiv 33.3 kWh

In order to be competitive, and eventually replace the hydrocarbon technology, the US Department of Energy (DOE) established various targets (Table 5-1) in January 2002 for onboard hydrogen storage systems to be used in light-duty vehicles. In addition to these targets, factors such as safety, toxicity, fuel (H₂) purity, leakage limit and durability of the system are also considered. It is also important to note that these targets are meant for the entire hydrogen storage system and not for the material used for storing hydrogen; therefore, the challenge before the research community is much greater. While established hydrogen storage technologies such as compressed hydrogen, liquid hydrogen

and slush hydrogen can be used for stationary applications, they do not pass the gravimetric capacity and safety thresholds established by the DOE for mobile applications. Moreover, a significant portion of cost and energy has to be invested for liquefaction and compression of hydrogen and to insulate the system to mitigate boil-off, thereby reducing the energy pay-off for such systems. Researchers are therefore rigorously pursuing both physical (*e.g.*, activated carbon, carbon nanotubes, porous polymers, metal-organic frameworks *etc.*) and chemical (*e.g.*, metal hydrides, synthesized hydrocarbons, amine borane complexes *etc.*) pathways for hydrogen storage in mobile applications. To date, a plethora of literature, including several comprehensive reviews and reference books,²⁻⁶ has been published covering various hydrogen storage materials. In this thesis, we focus on NaBH₄ as the source of hydrogen, for reasons mentioned below.

The potential of NaBH₄ as a hydrogen source was realized as early as 1953 when Schlesinger *et al.* demonstrated the facile hydrolysis of NaBH₄ in water leading to its decomposition and releasing hydrogen gas.⁷ In order to control the hydrogen released from NaBH₄, the aqueous solution of NaBH₄ can be stabilized by addition of an alkali hydroxide. A solution of NaBH₄ at pH > 9 is highly stable and can be easily transported without any hydrogen release. Hydrogen can be extracted from such a solution by means of a heterogeneous metal catalyst, typically Pt-⁸ or Ru-based^{9,10}. Hydrogen evolution depends not only on the catalyst, but also on parameters such as temperature, pH and concentration. The reaction, in theory, produces up to eight hydrogen atoms (four molecules) from four atoms of hydrogen in the NaBH₄ and water each (Eq. (5-1)).



NaBH_4 has numerous advantages as a source of hydrogen making it a very attractive for mobile fuel cell application. NaBH_4 has 10.9 wt.% hydrogen content and can be safely stored as alkaline-stabilized aqueous solution for months. The catalytic hydrolysis of NaBH_4 is exothermic ($\Delta H = 217$ kJ/mol) and operates *via* zero order kinetics;¹⁰ hydrogen can therefore be extracted at room temperature without any input heat. Moreover, due to the absence of any side-reactions, the hydrogen obtained is very pure. The byproducts of the hydrolysis reaction are environmentally benign and can be recycled back to NaBH_4 .

Despite these advantages, there are several challenges that have to be overcome before the implementation of NaBH_4 as hydrogen source in mobile fuel cell technology. Recycling of the spent fuel (*i.e.*, NaBO_2) to NaBH_4 is possible by reaction with MgH_2 ;¹¹ coke or methane;¹² or *via* various electrochemical pathways¹³, through they may not be necessarily economically favorable.¹⁴ One must realize however that the hydrolysis by-product, NaBO_2 , is in the form $\text{NaBO}_2 \cdot x\text{H}_2\text{O}$ ($x = 2$ to 4). Therefore, conversion of $\text{NaBO}_2 \cdot x\text{H}_2\text{O}$ to NaBH_4 , *via* the aforementioned techniques, must involve an additional step to remove the crystalline water. Moreover, it was shown that the conversion rate decreases with an increase in the crystalline water content.¹⁵ Besides poor recyclability, the current price of NaBH_4 (~\$55/kg) is too high and therefore restricts any serious consideration for its use as a source of hydrogen.¹⁶ There are however claims made that technology is being developed that will reduce the cost of NaBH_4 by 1/10th of its current price.¹⁷ Even if such drastic reduction in price occurs, the price of hydrogen generated

from NaBH_4 will be $\sim \$26/\text{kg}(\text{H}_2)$, which is still 10–15 times the price of gasoline (1 kg of $\text{H}_2 \approx 1$ gallon of gasoline equivalent).¹⁸ The high price of hydrogen extraction from NaBH_4 is primarily because heterogeneous Ru or Pt-based catalysts constitute a significant portion of the cost. Economical viability of the NaBH_4 -based hydrogen storage systems therefore depends on the development of cheaper alternatives for noble-metal catalysts without compromising the hydrogen discharge kinetics.

In this thesis, we develop Co-based catalyst using nanoPPX film as the catalyst support. Co nanoparticles are stabilized onto the nanoPPX template using noncovalent functionalization strategy, described in Chapter 2. By engineering the porosity during nanoPPX deposition and/or metal deposition stages, it is possible to attain hydrogen release rates that are comparable to those achieved by noble metal catalysts. Not only is the Co metal comparatively inexpensive compared to Ru or Pt, but also the combination of OAP and electroless metallization used for the preparation of the catalyst is potentially scalable.

5.1.2. Preparation of Co Catalyst

For Co metallization, pyridine functionalization (both aqueous and vapor treatments) and surface catalyzation was carried out for 48 h and 45 min, respectively, on helical nanoPPX films per the procedure described in Chapter 2. After the two treatments, the films were then transferred to the electroless Co plating bath that was freshly prepared using previously reported procedure.¹⁹ Briefly, 0.9 g of tetrasodium salt of ethylenediaminetetraacetic acid (EDTA), 1 g of NH_4Cl and 0.6 g of $\text{CoCl}_2 \cdot 6\text{H}_2\text{O}$ were dissolved in 15 mL of water. A 5 mL solution containing 0.4 g of dimethylamine-borane

(DMAB) in water was then added. The pH of the resultant solution was adjusted to 8.2 by drop-wise addition of 0.1 M NaOH (aq) solution. Surface catalyzed helical nanoPPX films were submerged in the plating bath and metallization was allowed to continue for the specified time at 25 °C. The Co plating bath was gently agitated during metallization to remove any bound H₂ bubbles on the surface. Co coated helical nanoPPX films were removed from the bath, rinsed in DI water, dried under N₂ gas, and stored in a vacuum desiccator until required for hydrogen release experiments.

5.1.3. Hydrogen Release Rate Measurement

Aqueous solution of 2.5% NaBH₄ (0.677 M) and 1% NaOH (0.261 M) was used for all the experiments at room temperature. The pH (=13) was kept constant, while the solution temperature was maintained at 25 ± 0.5 °C. The solution was contained in a 125 mL beaker, and the hydrogen gas generated was collected in a water column, which was immersed into a beaker. The amount of hydrogen release was recorded with respect to time. From these data, the release rate was obtained by differentiating the hydrogen release volume with respect to time. The hydrogen release rate was measured in mL of hydrogen per square centimeter area of the cobalt film per minute (mL·cm⁻²·min⁻¹).

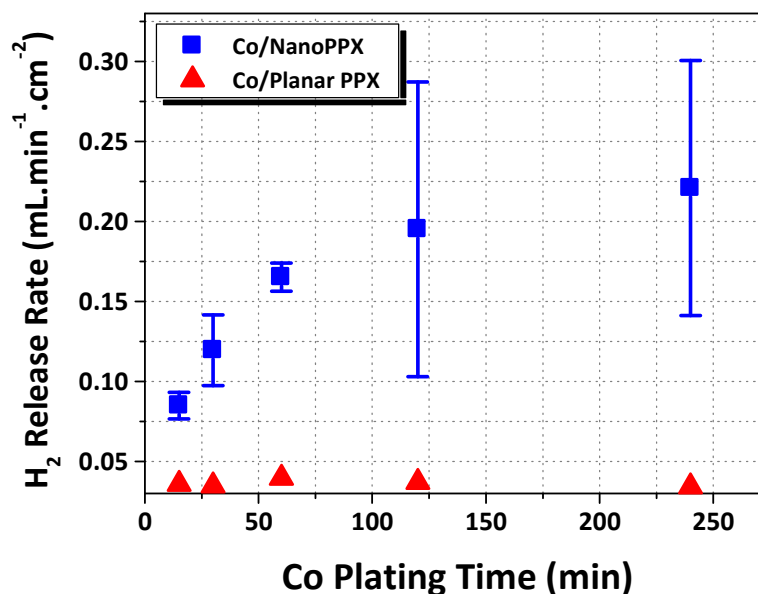


Figure 5-1. Effect of Co plating time on the hydrogen release rate from NaBH_4 decomposition. Other metallization parameters, *i.e.*, pyridine adsorption time, PD1 treatment time are as given in Section 5.1.2. Reprinted from *J. Power Sources* 182, 323–328, Copyright 2008 with permission from Elsevier.

Hydrogen release rates obtained on Co/nanoPPX films show a monotonic increase leading to saturation with respect to Co plating time, as seen in Figure 5-1. On the other hand, Co plated on planar PPX surfaces using analogous metallization route show little or no hydrogen evolution (Figure 5-1). The noticeable difference in the catalytic activity of the two sets of films is because of the morphology of the metal layer. While Co deposited on the nanoPPX film show a continuous and conformal (with respect to the underlying nanoPPX) metal growth, Co metallized planar PPX shows non-continuous and/or no metallization with poor adhesion, as evidenced in Chapter 2. Figure 5-2 shows the EDX data obtained for weight percentage of deposited Co as a function of plating time. An

exponential decay of the cobalt amount that saturates at ~90 wt.% is observed. At plating times less than 45 min, the low coverage of Co on the nanoPPX surface has poor catalytic activity that is manifested in the above hydrogen release rate data. For longer plating times (*i.e.*, > 45 min), the nanoPPX surface is completely covered with Co, evident in the EDX data. As a result, the catalytic activity is now dependent on the porosity of the Co layer, rather than the coverage. The porosity of the Co layer, quantified as the surface roughness, too shows saturation at longer plating times (Figure 5-2) due to pore “fill-up” by the deposited metal, per our metal growth model. Catalytic activity therefore saturates at longer plating time.

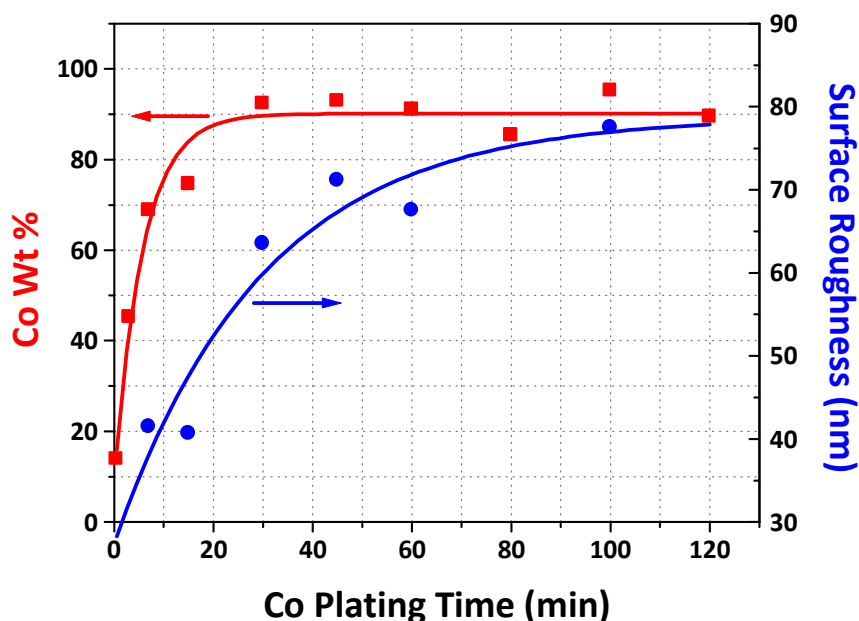


Figure 5-2. Plots showing Co weight percentage (from EDX) and surface roughness (from AFM) of Co membrane deposited on nanoPPX film with respect to Co plating time. First-order exponential decay fits for both plots are shown for visual assistance.

Catalytic activity can be improved by increasing the surface area at the polymer deposition and/or the metallization stage, as explained herein. Surface area increase at the polymer deposition stage is achieved by using a helical nanoPPX film instead of a columnar nanoPPX that not only exhibits higher surface area, but also eliminates any effect due to the spatial non-uniformity in the thickness typically observed in a columnar nanoPPX film. Increase in the porosity at the metal deposition state is achieved by switching the pyridine treatment condition to vapor phase, as described in Chapter 2.

Figure 5-3 shows the hydrogen production obtained from a unit area of the Co films prepared from vapor and aqueous pyridine-treated helical nanoPPX substrates plated 60 min. The hydrogen release shows an approximately linear increase in the volume of hydrogen as a function of time. Using a linear curve fit through the observed data points the hydrogen release rate was calculated. Clearly, the Co film deposited on vapor pyridine treated nanoPPX films show a higher hydrogen release rate ($0.37 \text{ mL}\cdot\text{cm}^{-2}\cdot\text{min}^{-1}$) compared to Co film deposited on aqueous pyridine treated nanoPPX films ($0.25 \text{ mL}\cdot\text{cm}^{-2}\cdot\text{min}^{-1}$). To understand in detail the reasons for the observed difference in the catalytic activity, we studied the topographical microstructures of the two films using FESEM. Figures 5-4A and 5-4B show the FESEM images of Co coated (1 min in Co plating bath) nanoPPX films treated with aqueous and vapor pyridine, respectively. The FESEM images indicate that during the Co deposition, the topography of the underlying helical nanoPPX film is maintained. In other words, during initial stages of Co growth, Co nanoparticles cover the nanoPPX conformably. At longer bath times however, Co film grown on vapor treated nanoPPX film shows a higher porosity due to the slower growth of the metal fronts (Figure 5-4D) compared to Co film grown on

aqueous pyridine treated nanoPPX film that shows fused metal fronts (Figure 5-4C). This behavior is consistent with the refined model for Ni film growth described in Chapter 2. The smaller nanoparticles and higher porosity of Co film deposited on vapor pyridine treated nanoPPX film translate into higher catalytic activity due to the larger number of active reaction sites.²⁰

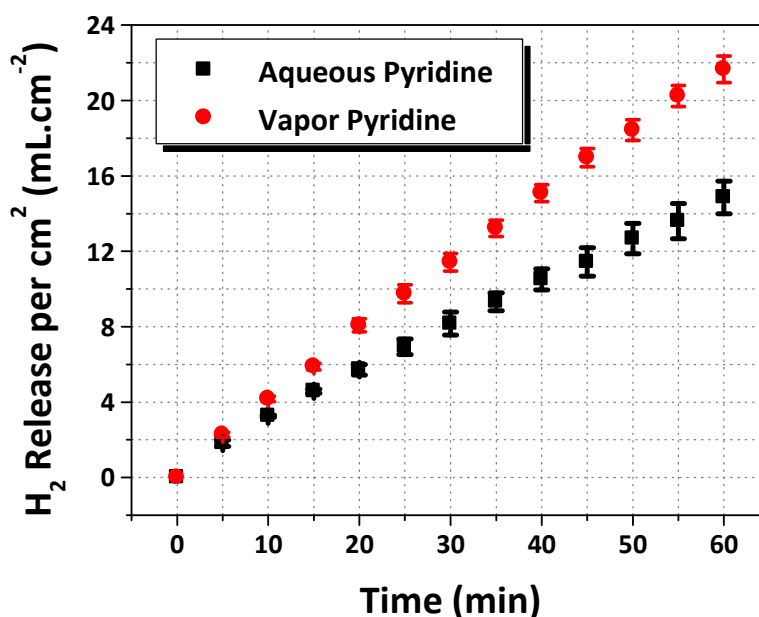


Figure 5-3. Hydrogen collected from catalytic decomposition of alkaline stabilized aqueous NaBH₄ solution using Co film deposited on helical nanoPPX templates treated with aqueous and vapor pyridine. Other metallization parameters: Ligand adsorption time = 48 h. PD1 treatment time = 45 min. Co plating time = 60 min. Hydrogen volume measured at room temperature and pressure (RTP). Raw data of hydrogen volume was normalized with the area of the catalyst film. Error bars represent one standard error of mean. Reproduced with permission from Malvadkar *et al.*, *Langmuir* **26**, 4382–4391 (2010). DOI: 10.1021/la9034529. Copyright 2010 American Chemical Society.

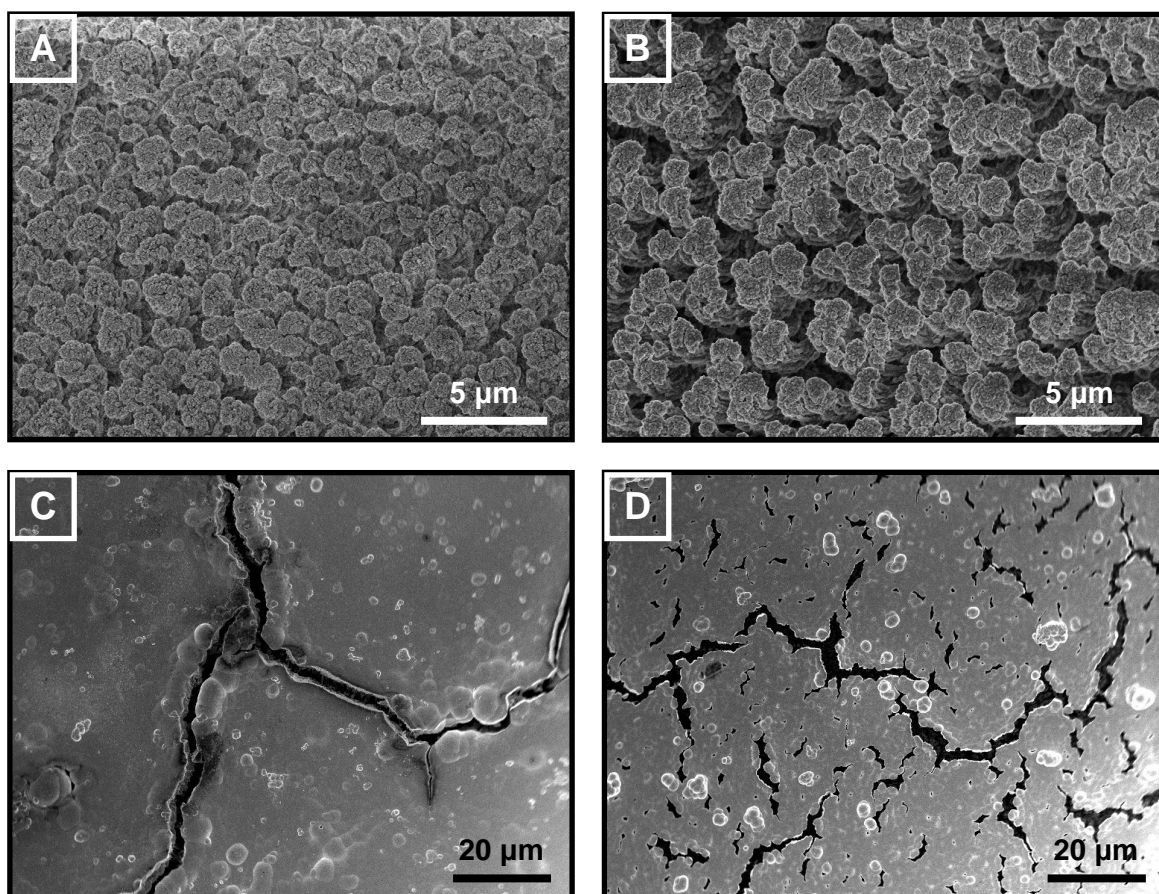


Figure 5-4. FESEM images showing topography of Co film deposited on helical nanoPPX films treated with (A) aqueous and (B) vapor pyridine, respectively, after 1 min Co plating. Scale bar for both images = 5 μm . FESEM images showing topography of Co film deposited on helical nanoPPX films treated with (C) aqueous and (D) vapor pyridine, respectively, after 60 min Co plating. Scale bar for both images = 20 μm . Reproduced with permission from Malvadkar *et al.*, *Langmuir* **26**, 4382–4391 (2010). DOI: 10.1021/la9034529. Copyright 2010 American Chemical Society.

The reusability of the Co/columnar-nanoPPX (plating time = 240 min) catalyst was tested under identical experimental conditions (*i.e.*, 2.5% NaBH₄ and 1% NaOH). The catalyst was washed with water and dried with N₂ after each 1 h cycle. The hydrogen release rate showed only 8% decrease in the catalytic activity after four cycles.²¹ Further, we compared the release rates obtained from our Co/nanoPPX catalysts with some of the prominent data published in literature, as listed in Table 5-2. We should note that our hydrogen release rate is significantly higher compared to that of a metallic cobalt catalyst (*i.e.*, 32 mL(g·min)⁻¹).²² Other metal catalysts, such as Pt and Ru, show higher release rates compared to that obtained on our catalysts (Table 5-2). However, the facile preparation technique, with comparable release rate results, makes our method promising for future development in this area.

Table 5-2. Comparison of hydrogen release rates from catalytic decomposition of NaBH₄ on various catalysts.

Catalyst	[NaBH ₄] (wt. %)	[NaOH] (wt. %)	Temperature (°C)	H ₂ release rate (mL/g·min)	Reference
A-26 ^a	20	10	25	4032	10
IRA-400 ^a	12.5	1	25	~9600	9
Pt/C	10	5	No data	23,090	23
CoB ^b	2	5	15	~3500	24
Co/nanoPPX	2.5	10	25	~7450	This work

^a Ru-based catalyst systems. ^b Unsupported catalyst.

5.1.4. Summary

In summary, we have demonstrated an inexpensive means to extract hydrogen out of NaBH₄ by using Co/nanoPPX catalyst prepared *via* noncovalent functionalization

route. Cost reduction is possible not only by replacing noble metal (*e.g.*, Pd, Ru *etc.*) by Co, but also by the scale-up capability of the entire fabrication process (*i.e.*, OAP followed by electroless metallization). Highest hydrogen release rate ($0.37 \text{ mL}\cdot\text{min}^{-1}\cdot\text{cm}^{-2}$) is obtained on Co membranes deposited on helical nanoPPX films functionalized *via* vapor pyridine treatment. A geometric area of $\sim 3.75 \text{ m}^2$ for Co/nanoPPX (helical morphology) is required to yield the DOE-targeted discharge rate of $0.02 \text{ g (H}_2\text{)/s}$ (Table 5-1). Such an area can be easily generated by stacking multi-layers of Co/nanoPPX catalyst plates held together by separators for fluid infiltration.

Despite these excellent results, one should note that presently no material, including NaBH_4 , has met all the DOE targets for on-board hydrogen storage.²⁵ In November 2007, an independent review panel appointed by the DOE unanimously recommended against pursuing NaBH_4 for onboard hydrogen storage in a “go/no-go” decision, primarily because the issue of cost overshadows all other advantages of the material.²⁶ NaBH_4 may therefore be more suitable for portable applications in niche areas such as an auxiliary power source. Nonetheless, this does not undermine the excellent catalytic properties exhibited by Co/nanoPPX. Analogous approach to reduce catalyst cost could be applied in other chemical reaction systems. More importantly, we have shown a generic approach to grow porous metals or ceramics with controlled properties that extends its application range beyond catalysis. Next, we show that quasi-periodic and uniform nano-morphology of nanoPPX can be exploited in fabricating SERS-platforms for biodetection.

5.2. Surface-Enhanced Raman Spectroscopy Substrates

5.2.1. Introduction

Ever since its discovery and verification in the 1970s,²⁷⁻²⁹ surface enhanced Raman spectroscopy (SERS) has become very popular among surface scientists due to its ability to characterize molecular monolayers, interfacial reactions, and biological surfaces. Despite such popularity, there are several problems in using SERS as a diagnostic tool, such as false-negative/false-positive identification of the analyte, especially for large biomolecules and microorganisms; low signal enhancement; and non-reproducibility. It was soon realized that there is a strong correlation between the signal enhancement properties, such as the enhancement factor (EF) and signal repeatability and stability, with the morphology of the SERS-active metals such as Au and Ag. Although enhancement can be achieved on rough SERS-active metals prepared by any conceivable method, challenges lie in fabricating these surfaces with high consistency, reproducibility and stability in order to achieve reliable repeatability in the SERS signal. The rapid development in nanoscience and nanotechnology in the past two decades has renewed interest in SERS due to its potential to overcome these barriers.

Facile synthesis of Au and Ag nanoparticles is possible *via* wet chemical route through controlled reduction of their respective ions producing size-controlled SERS templates that exhibit large enhancement. The extensive literature on using Au and Ag nanoparticles in SERS suggests that besides the size, factors such as particle size variation, shape,³⁰⁻³² and the state of aggregation³³ have a great impact on the enhancement properties. For instance, it was demonstrated that nanoparticle cluster of 1

μm diameter exhibit EF on the order of 10^6 compared to the isolated counterparts that showed only 10^4 -fold enhancement of the Raman signal.³⁴ Although, control of size and shape of nanoparticles is easily achievable, control over the aggregation is not. Traditionally prepared Au and Ag nanoparticles using citrate reduction have a negative surface charge. This surface charge (*i.e.*, zeta potential) controls the particle-particle separation. Through addition of ionic analyte, the zeta potential varies and consequently disturbs the state of aggregation. One way to control the particle-particle separation can be by using an appropriate ligand. However, using such nanoparticles as SERS-active ingredient in chemical diagnosis creates large interference peaks from the ligand itself.

Given the importance of particle spacing in the SERS behavior, a good control over organization of nanoparticles is necessary. Stabilizing the colloidal nanoparticles on a surface was proposed as a possible method to control the enhancement properties.³⁵ Unfortunately, SERS substrates prepared by stabilizing nanoparticles on a flat surface lack long-range periodicity, which is an absolute necessity for characterizing large biomolecules and microorganisms. Alternatively, SERS substrates can be generated by nanoscale patterning of Au and Ag using advanced methods such as electron beam lithography, dip-pen lithography, and scanning probe lithography. However, these serial technologies are of little practical use due to their limited scale-up capability. Three-dimensional organization of Au nanoparticles has shown to yield better SERS performance compared to the two-dimensional arrangement on flat surfaces.³⁶⁻³⁸ Moreover, introducing periodicity in these three-dimensional ensembles induces additional enhancement effect.³⁹ Methods such as nanosphere lithography,³⁷ layer-by-layer assembly,^{40,41} self-assembly,³⁸ deposition of Au or Ag nanoparticles on ceramic

nanorods⁴², polymeric nanorods,⁴³ anodic aluminum oxide nanochannels,⁴⁴ and optical fibers⁴⁵ have been employed to build three-dimensional architectures of Au or Ag nanoparticle structures.

The nanostructure of a nanoPPX film comprises of quasi-periodic, oblique arrangement of PPX nanorods on the substrate.⁴⁶ These morphological properties are ideal to build SERS substrates for biodetection that requires high structural uniformity on a large area ($\sim\text{mm}^2$). For instance, we showed that pathogenic bacteria⁴³ and viruses⁴⁷ can be detected with excellent sample-to-sample reproducibility and low detection time (~ 10 s spectral acquisition time) using thermally evaporated Au films on nanoPPX as SERS platforms. Although such excellent results enhance the potential of this technology for diagnostics, the technique as described to date is only applicable to pure samples (*i.e.*, lack of target specificity). We therefore explore molecular probe (MP) based detection approach, which is highly specific to target DNA, in this thesis.

In this thesis, we prepare Ag/nanoPPX SERS substrates *via* electroless methods using two routes: (1) by treating the nanoPPX films by a commercial Pd/Sn catalyst and then metallizing the surface using an electroless Ag bath; (2) *via* noncovalent functionalization, *i.e.*, first treating the nanoPPX films with an adhesive component (ligand) that binds a Pd catalyst and then metallizing the surface using the Ag bath. Structural characterization is performed using SEM, TEM and AFM studies, while EF is measured using 4-fluorobenzenthioi (FBT) as the probe molecule. Further, we describe a metal growth model correlating the EF to the morphological characteristics of the substrates. From the substrates prepared by the two routes mentioned above, we one substrate based on their morphology and enhancement properties for detecting

Respiratory syncytial virus (RSV) gene sequence by means of a MP bearing a fluorescent moiety.

5.2.2. Preparation of NanoPPX-Templated SERS Substrates

Columnar nanoPPX films were deposited on allyl-functionalized Si substrates using the procedure explained in Chapter 2. Preparation of SERS substrates *via* electroless routes requires preparation of various electroless reagents as described below.

Electroless Reagents: NanoPPX films were subjected to Ag metallization using two different routes: (A) using a commercial Pd/Sn catalyst followed by plating in Ag bath and (B) using Sn-free Pd catalyst followed by plating in Ag bath. The preparation of various electroless reagents used for Ag metallization is described below:

- 1. Pd/Sn Catalyst:** Pd/Sn catalyst was freshly prepared just before use. To prepare the Pd/Sn catalyst, 10 g of CATAPREP™ 404 stabilizer (Shibley Inc.) was weighed and dissolved in ~45 mL of H₂O. This solution was transferred to a 50 mL volumetric flask. 1.5 mL of CATAPOSIT™ 44 Pd/Sn concentrate (Shibley Inc.) was then added using a micropipette and diluted to the mark using H₂O. The flask was tightly sealed because the colloid is O₂ sensitive if exposed for extended times.
- 2. Sn-free Pd Catalyst:** Sn-free Pd catalyst was prepared per the procedure described for PD1 in Section 2.2.2 (Chapter 2).
- 3. Electroless Ag Bath:** Electroless Ag bath too was freshly prepared before each experiment. To prepare the bath, 0.7 g of AgNO₃ and 10 g of (NH₄)₂SO₄ were

dissolved in 70 mL of H₂O and the resulting solution was added to a 100 mL volumetric flask. Aqueous ammonia (28%, w/w) was added to dilute the solution up to the mark. 2.8 g of CoSO₄·7H₂O was then added to the solution. The resultant composition of the bath was AgNO₃ (0.05 M), (NH₄)₂SO₄ (0.9 M), NH₃ (2.1 M), CoSO₄·7H₂O (0.12 M), pH = 10.

Scheme A – Direct Ag Metallization using Pd/Sn: NanoPPX films were treated with Pd/Sn catalyst for 10 min. Excess catalyst was carefully removed using a Pasteur pipette. The films were then gently washed and rinsed in 0.12 M HCl (aq) solution for 5 – 10 s. Care was taken not to pour the HCl solution directly on the film as it can remove the bound Pd/Sn catalyst. Immediately after HCl treatment, the films were immersed in the 10% Accelerator 19™ (aq) solution for 30 s. Film were removed from the Accelerator solution, washed in H₂O and transferred to the electroless Ag bath. The plating bath was gently agitated to ensure uniform deposition of Ag onto the nanoPPX films. Plating was carried out for various times ranging from 5 – 150 min.

Scheme B – Direct Ag Metallization using PD1: Metallization using PD1 catalyst was carried out according to Scheme 2.2 (Chapter 2). Briefly, samples were treated with 1 M pyridine (aq) for ~48 h, followed by PD1 treatment for 45 min and finally Ag plating was carried out for various times ranging from 5 – 150 min.

5.2.3. Preparation of Molecular Probes

RSV Hairpin Probe Design: A probe sequence from the Respiratory syncytial virus (RSV) genomic sequence (Accession Number: M11486) was selected corresponding to the G protein sequence from 5329–5352 bp (Table 5-3). This sequence was evaluated for minimal secondary structures, loop and dimer formation using Gene Runner DNA analysis software (www.genelink.com). The nearest neighbor T_m of the probe is 60 °C. A hairpin sequence was added to the 5' and 3'-end of the sequence that yields a stable hairpin structure without creating loop and secondary structure with the target loop sequence. The 5'-end of the hairpin probe sequence was either labeled with hexachlorofluorescein (Hex) or cyanine 5 (Cy5) dye. The 3'-end was modified with two thiol linker groups.

Table 5-3. Designed RSV Probes

Synthetic control (SPCT)	positive template	TTTGGTGGTGTGAT GGTTGGCTCTTCTGT GGGCTTGGTG	G probe complementary in M11486: 5321–5360
G gene from RSV		CGCAGCCACAGAAG AGCCAACCATCAAC ACTGCG	G probe position in M11486: 5329–5352

Probe Modification: The hairpin Probe DNA sequences were synthesized at Genelink with SC6 thiol and Cy5 fluorophore containing sequence as detailed in Table 5-4. These probes were synthesized using 3' thiol C6 CPG or 3' Dithiol CPG (Glen Research, VI, USA) as the solid support followed by the oligo sequence and coupled to Cy5 dye. The crude probes obtained after complete deprotection were ethanol precipitated and

polyacrylamide gel purified. Immobilization of DNA, unless otherwise stated, was carried out as follows: Prior to immobilization steps, the SERS substrates were cleaned in a UV/ozone chamber oxidative medium for ~2 min. Immobilization of Probe-DNA on the SERS substrate was allowed for ~24 h at room temperature. Afterwards, the surfaces were washed several times with the buffer solution and dried under air stream.

Table 5-4. Modifications and Synthesis

Probe Name	GL Designed Probes Final	3' Mod (details)
SPCT	TTTGGTGGTGTGATGGTTGGCT CTTCTGTGGGCTTGGTG	
SC6-Cy5	CGCAGCCACAGAAGAGCCAACC ATCAACACTGCG7	SS-C6 (3'-SH-C6-oligo-Cy5)

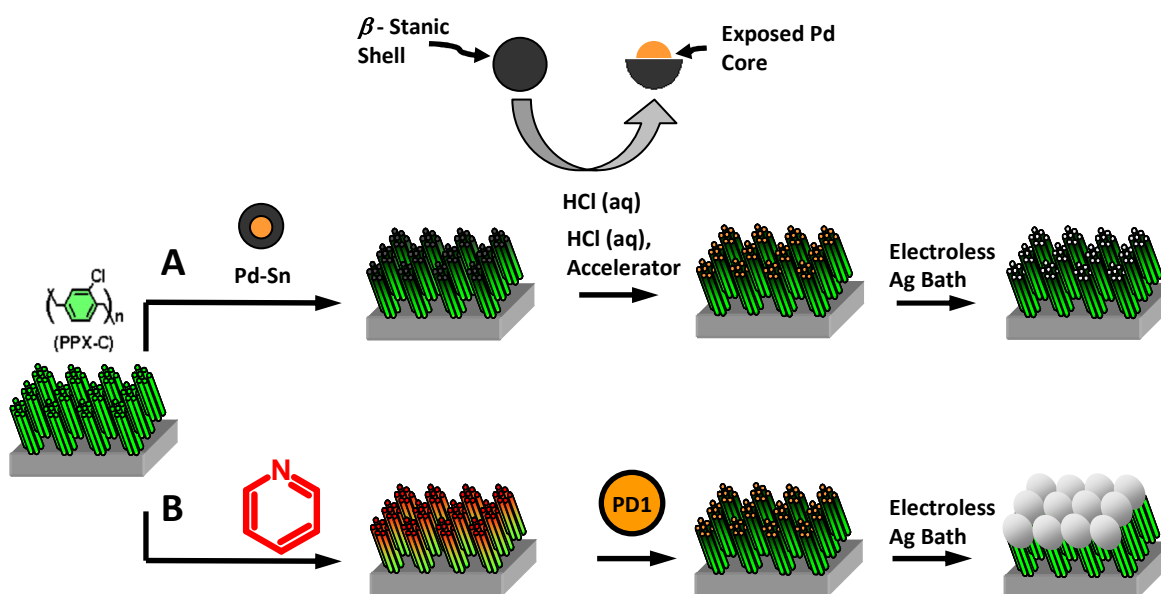
Hybridization Assay: Hybridization was carried out by adding a 100 μ L of complementary DNA (at least 4-fold of probe DNA concentration) onto the surfaces. The hybridization assay was allowed to react for ~3 h in a dark and ambient environment. Afterwards, the assay was rinsed with the buffer solution and dried under air stream.

5.2.4. Characterization of SERS Substrates

4-fluorothiophenol (FBT) (Caution: Stench from FBT. Use only in a well-ventilated fume hood) was used as the analyte to measure the SERS enhancement and signal uniformity of the substrates. The analyte solution was prepared by dissolving 20 μ L of FBT in 20 mL of ethyl alcohol. Ag coated nanoPPX films were immersed in the FBT solution immediately after Ag deposition and stored overnight in a sealed vial. Afterwards, the films were removed and rinsed in ethyl alcohol for 1 min. to remove any

physisorbed FBT molecules. The films were stored in sterilized Petri dish until required for SERS characterization. We used Renishaw inVia microRaman equipped with 35mW HeNe laser ($\lambda = 632.8$ nm) and Ar-ion ($\lambda = 514.5$ nm) lasers for SERS characterization. For each sample the 50 \times objective lens and 10 s acquisition time was used. For normalization of SERS spectra due to the variation in the acquisition power, a Raman spectrum of Si (100) was used as the reference.

5.2.5. Mechanism of Metal Growth



Scheme 5-1. NanoPPX-templated SERS substrates prepared *via* (A) commercial Pd/Sn catalyst treatment; (B) noncovalent pyridine adsorption followed by PD1 treatment.

Schemes 5-1A and B show the two routes used to prepare SERS substrates. Scheme A uses a commercial Pd/Sn core/shell colloidal species to catalyze the nanoPPX

surface. The β -stannic shell binds the colloid onto the polymer surface *via* noncovalent forces such as van der Waals interaction. Later, the catalytic Pd⁰ core is exposed by treatment with an “acceleration” agent (*e.g.*, fluoroboric acid) that removes a portion of the β -stannic shell. After exposing the Pd⁰ core, the films are transferred to the Ag bath where reduction of Ag takes place on the catalytic Pd⁰ sites. Scheme B uses the noncovalent functionalization strategy described in Chapter 2. Similar to other metal layers, Ag/nanoPPX substrates prepared *via* Scheme B show enhanced interface adhesion, which is manifested in the Scotch[®] tape adhesion test resulting in less than 5% metal removal. SERS substrate prepared by this route therefore shows enhanced stability and robustness compared to substrates prepared *via* Scheme A in which the metal particles are bound *via* much weaker van der Waals interaction.

5.2.6. Structure of SERS Substrates

In the remainder of our discussion, references to films prepared by Schemes A and B are taken to mean films prepared as shown in Scheme 5-1. Figure 5-5A₁ shows the FESEM image (top-view) of a Ag/nanoPPX substrate prepared *via* Scheme A. Uniform deposition of Ag particles on the nanoPPX substrate is observed, resulting in a continuous porous film. However, the particle deposition occurs only on the top of the PPX nanorods relinquishing the underlying aligned nanorod morphology as shown in Figure 5-5A₂ (side-view). In contrast, Ag formation according to Scheme B in Figure 5-5B₁ appears to be conformal to the aligned PPX nanorods, similar to the observed morphology of Ni⁴⁸ and Co⁴⁹ films previously grown on nanoPPX substrates *via* the noncovalent ligand functionalization route. Figure 5-5B₂ shows a side-view of the Ag

plated nanoPPX films prepared according to Scheme B. The deeper penetration of the metal in the nanoPPX porous structure observed contrasts with the morphology of the Ag/nanoPPX film prepared *via* Scheme A (Figure 5-5A₂) and contributes to the interface adhesion *via* mechanical metal anchoring, complementing the contribution of π - π interactions, consistent with the aforementioned Scotch[®] tape test result.

Table 5-5. Comparison of the SERS substrates.

Sample No.	Scheme	Catalyst Used	Catalyst Time (min)	Plating Time (min) (Metal)	Ag Particle Size ($D_{\text{average}} \pm \sigma$)	Mean EF
1	A	Pd/Sn	10	5 (Ag)	—	6.8×10^2
2	A	Pd/Sn	10	30 (Ag)	—	1.4×10^4
3	A	Pd/Sn	10	60 (Ag)	22 ± 24	6.1×10^4
4	A	Pd/Sn	10	150 (Ag)	—	3.8×10^4
5	B	PD1	45	5 (Ag)	—	2.1×10^4
6	B	PD1	45	30 (Ag)	—	2.5×10^5
7	B	PD1	45	60 (Ag)	69 ± 47	3.0×10^5
8	B	PD1	45	150 (Ag)	—	1.2×10^5

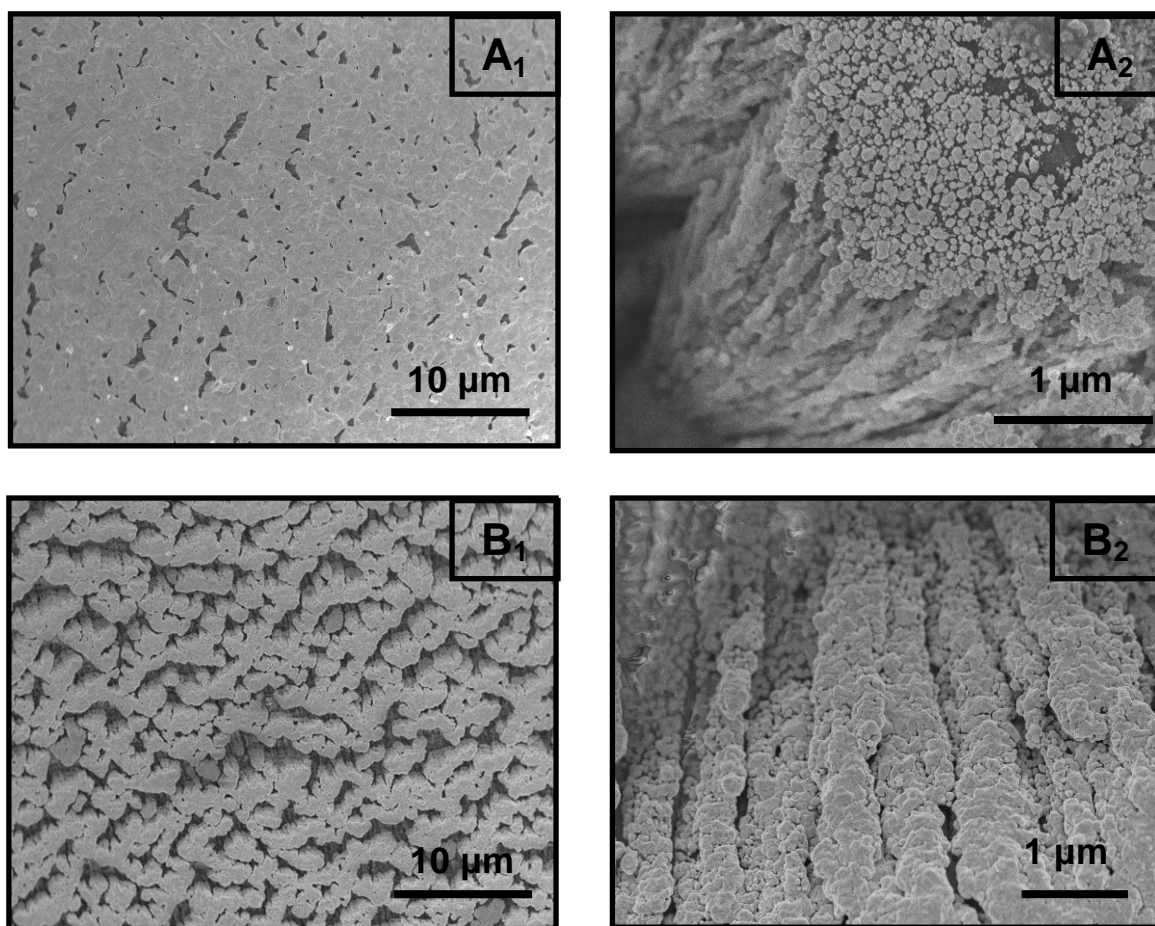


Figure 5-5. FESEM image of SERS-active Ag substrate prepared *via* (A₁) Scheme A (*cf.* Sample 3 in Table 5-5); (B₁) Scheme B (*cf.* Sample 7 in Table 5-5); (A₂) shows high magnification SEM image of Scheme A substrate prepared by 15 min plating in Ag bath. Particle agglomeration on top of the PPX nanorods is visible (B₂) shows high magnification cross-section FESEM image of Scheme B substrate plated for 60 min in Ag bath. Conformal growth of Ag over the aligned nanorod morphology of a nanoPPX film is evident.

Contact mode AFM images were taken for substrates prepared *via* Scheme B with varying plating time. The AFM images show a monotonic increase in the Ag particle size

with the plating time (Figure 5-6), though exact quantification of particle size is difficult due to the tip convolution. The increase in the particle size is accompanied by a decrease in particle-particle separation from adjacent PPX nanorods.

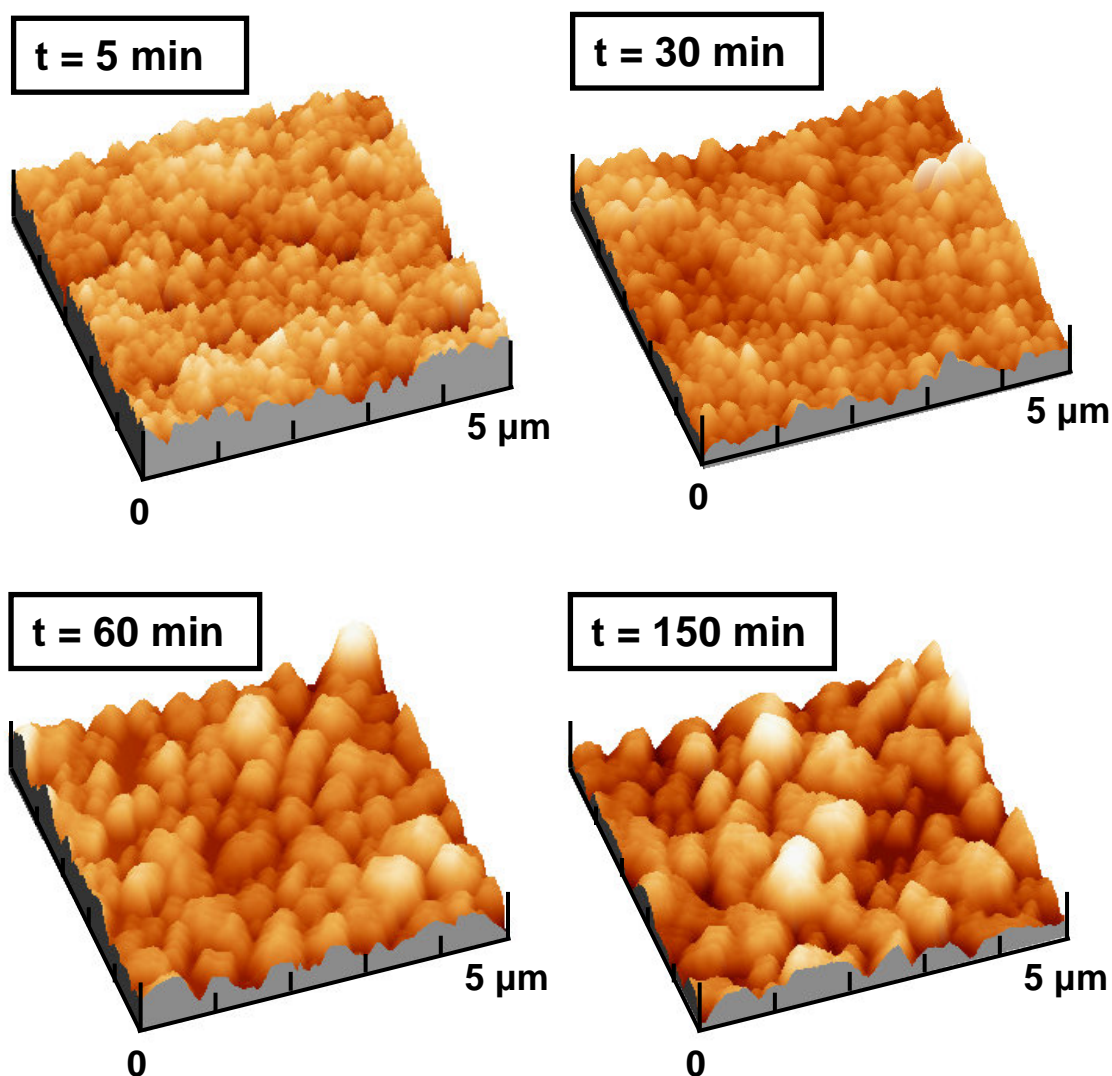


Figure 5-6. Contact mode AFM images of Scheme B substrates plated for 5, 30, 60 and 150 min in Ag bath. Other metallization parameters, *i.e.*, pyridine adsorption time, PD1 treatment time are as given in Section 5.2.2.

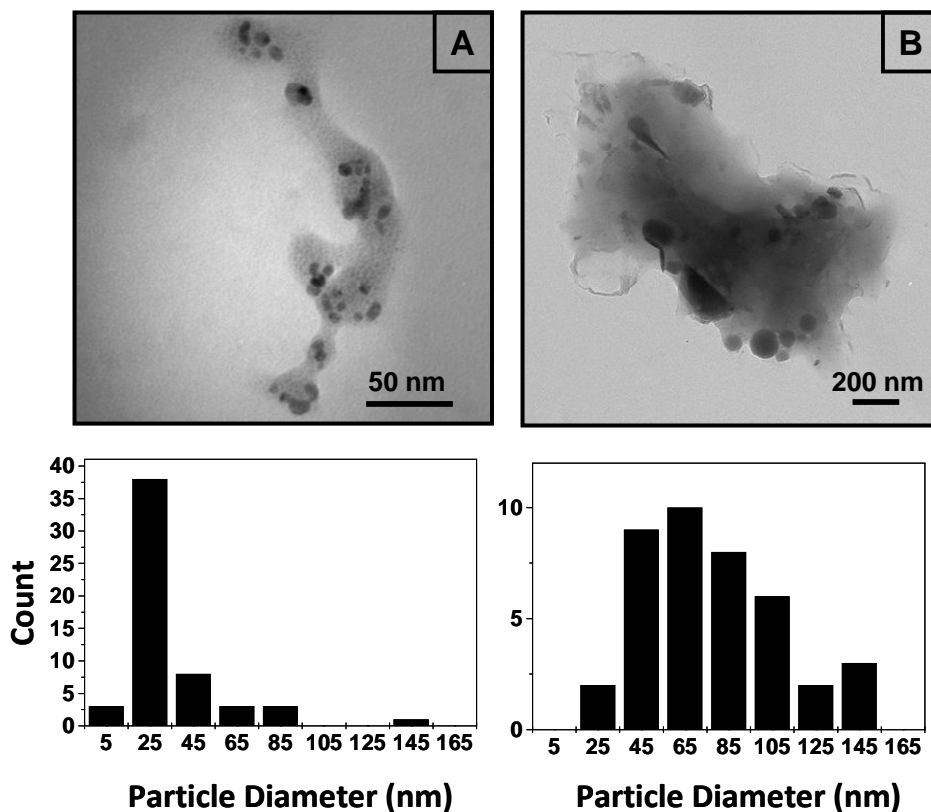


Figure 5-7. Particle size distribution (right) obtained from TEM images (left) of scarped-off Ag particles deposited on nanoPPX film *via* (A) Scheme A (*cf.* Sample 3 in Table 5-5); and (B) Scheme B (*cf.* Sample 7 in Table 5-5).

TEM analyses provide a quantitative measure of the Ag particle size distribution for the three types of substrates. All TEM images (Figures 5-7A and 5-7B) show Ag nanoparticles encapsulated by the PPX matrix. Particle size distribution (shown in Table 5-5) obtained from these images show the median particle size of Scheme A and B substrates to be ~ 22 nm and ~ 69 nm, respectively. In addition, the polydispersity, calculated as the standard deviation (σ) of particle size, of Scheme B ($\sigma_B \approx 47$) is higher compared to that of Scheme A ($\sigma_A \approx 24$). The large size and polydispersity of Ag particles of Scheme B substrates are inherited from the broad size distribution of PD1

particles (4–53 nm) used to catalyze the pyridine-functionalized nanoPPX film.⁵⁰ Moreover, the high surface coverage of pyridine on the nanoPPX surface *via* aqueous solution treatment also assists in binding PD1 particles with broad size range.⁵¹ Pd/Sn catalyst particles, on the other hand, exhibit much lower polydispersity values compared to PD1. Although typical Pd/Sn catalyst particle diameters range from ~1–5 nm, aggregates occur and exhibit somewhat larger apparent polydispersity values (4–20 nm).⁵² Consequently, Ag plating on nanoPPX films catalyzed by the Pd/Sn catalyst exhibit smaller average Ag particle sizes and particle distributions than Ag films plated using the PD1 catalyst.

5.2.7. SERS Properties

4-fluorothiophenol (FBT) (Caution: Stench from FBT. Use only in a well-ventilated fume hood) was used as the analyte to measure the SERS enhancement and signal uniformity of the substrates. The analyte solution was prepared by dissolving 20 μ L of FBT in 20 mL of ethyl alcohol. Ag coated nanoPPX films were immersed in the FBT solution immediately after Ag deposition and stored overnight in a sealed vial. Afterwards, the films were removed and rinsed in ethyl alcohol for 1 min. to remove any physisorbed FBT molecules. The films were stored in sterilized Petri dish until required for SERS characterization. We used Renishaw inVia microRaman equipped with 35mW HeNe laser ($\lambda = 632.8$ nm) and Ar-ion ($\lambda = 514.5$ nm) lasers for SERS characterization. For each sample the 50 \times objective lens and 10 s acquisition time was used. For normalization of SERS spectra due to the variation in the acquisition power, a Raman spectrum of Si (100) was used as the reference.

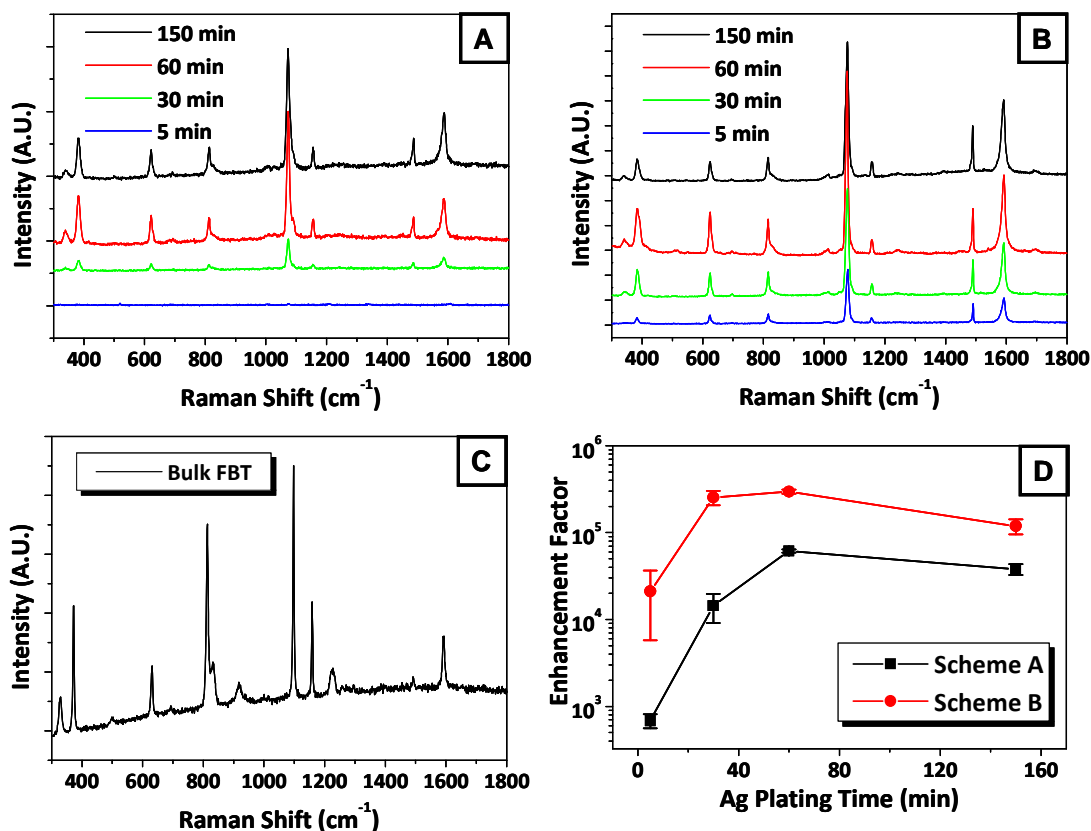


Figure 5-8. SERS spectra of FBT on substrates prepared *via* (A) Scheme A, and (B) Scheme B. (C) Raman spectrum of pure FBT. (D) Plot of EF (calculated from $\nu(\text{C-F})$ peak at 1074 cm^{-1}) against Ag plating time.

Figures 5-8A and 5-8B show the SERS spectrum of FBT adsorbed on Ag/nanoPPX substrate prepared *via* Schemes A and B, respectively. A bulk Raman spectrum of FBT is shown in Figure 5-8C for comparison. The major difference between the SERS and the bulk Raman spectrum is the absence of the 918 cm^{-1} peak corresponding to the $\delta(\text{C-S-H})_{\text{bend}}$ mode. The absence of the 918 cm^{-1} peak is due to the deprotonation of FBT resulting in the formation 4-fluorobenzenethiolate that is adsorbed onto the Ag surface. Similar observation was reported in previous SERS studies on

FBT.^{53,54} The $\nu(\text{C-F})_{\text{stretch}}$ peak at 1074 cm^{-1} observed in the SERS spectrum of FBT was used to calculate the EF for the substrate. The EF is given by:

$$EF(50 \times 1074 \text{ cm}^{-1}) = \frac{N_{\text{bulk}} I_{\text{poly}}}{N_{\text{poly}} I_{\text{bulk}}}, \quad (5-2)$$

where I_{bulk} and I_{poly} are measured intensities of FBT in bulk Raman and SERS mode, respectively, while N_{bulk} and N_{poly} are the number of molecules in the bulk and adsorbed on metalized nanoPPX substrate, respectively. Si phonon peak at 521 cm^{-1} was used as a basis of normalization of the SERS spectrum. N_{bulk} is estimated to be $\sim 4.6 \times 10^9$, based on the density of FBT (1.197 g/cm^3) and the volume of focal region produced by the confocal optics. N_{poly} is calculated to be $\sim 10^5$ based on a $1 \text{ }\mu\text{m}$ diameter circular area of the sample surface exposed to the incident beam. $I_{\text{poly}}/I_{\text{bulk}}$ is approximated to 1/15.

EFs obtained on substrates prepared *via* Schemes A and B are listed in Table 5-5. It is striking that substrates prepared using Scheme A and B show similar trend for EF variation with respect to Ag plating time, although Scheme A substrates show EF values are approximately an order of magnitude lower compared those exhibited by Scheme B substrates (Figure 5-8D). The highest EF achieved for both types of substrates occurs on samples that are plated for 60 min in Ag bath. The similarities and differences of the EF variation can be explained by studying the size distribution of their respective catalytic seed layer used in preparing the substrates and their Ag coverage on the nanoPPX templates.

5.2.8. Influence of Metal Structure on EF

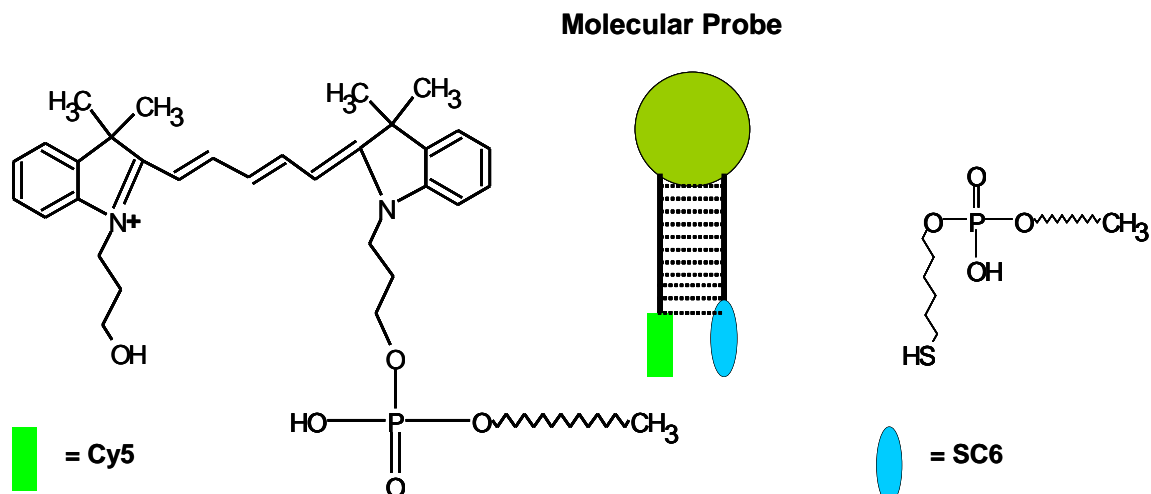
We describe herein a model correlating the observed variation of the EF and the growth of the Ag particles prepared *via* electroless metallization. Our model is partially substantiated by structural characterization (*i.e.*, FESEM, AFM and TEM studies) and previously studied geometry of the PPX nanorod growth.⁴⁶ For Ag/nanoPPX films prepared *via* Schemes A and B, the low EFs for substrates plated for less than 30 min reflects the low coverage of Ag on the nanoPPX templates. At these plating times, the Ag nanoparticles are small and have high curvatures, as observed by AFM (Figure 5-6), that are derived from the size of their Pd catalysts used. Moreover, at lower plating times, the Ag particle-particle separation between adjacent nanorods is too large for efficient interaction of their plasmon electromagnetic fields required for “hot-spot” formation on the surface. The enhancement achieved is only due to the curvature of the Ag particles and/or the formation of a few “hot-spots” due to particle agglomeration within a single PPX nanorod. At ~60 min of plating time, the distance between growing metal fronts on adjacent PPX nanorods are very close to each other. The gaps between these two metal fronts are now close enough for “hot-spot” formation. FBT molecules bound in these gaps experience strong electromagnetic fields during SERS excitation and therefore show highest EFs. At plating times greater than 60 min, the Ag particle growth fronts increasingly physically encounter growth fronts from Ag particles on adjacent PPX nanorods. As a result, the growing metal fronts merge with one another forming a continuous porous Ag film. Due to this fusion of Ag particles, the FBT molecules are restricted primarily on the surface of the film. Therefore, the only contribution to the

enhancement at this stage is due to the nanoscale roughness of the Ag film alone leading to the observed saturation of EF.

The difference in the enhancement factors between Ag/nanoPPX films prepared according to Schemes A and B, on the other hand, arises due to the difference in their morphologies and particle size distributions. The growth of Ag particles on Scheme B substrates occur uniformly along the length of the PPX nanorods (Figure 5-5B₂). We also know from previous studies that the distance between two adjacent PPX nanorods (center-to-center) is ~250 nm, while the average diameter of each nanorod is ~120 nm.⁴⁶ Therefore, in an ideal Ag/nanoPPX sample, two Ag particles growing on adjacent nanorods would have to reach a diameter of 65 nm in order to merge with one another. This value is in close agreement with the median Ag particle size of Scheme B substrate (~69 nm) that shows the highest EF. The growth of Ag particles on Scheme A substrates, on the other hand, occurs only on the top of the PPX nanorods. As a result, much of the contribution to the EF is due to particle agglomeration on top of the PPX nanorods (note Figure 5-5A₂). Moreover, Raman enhancement studies on single Ag nanoparticles by Emory *et al.* have shown that efficient enhancement using an incident laser with 647 nm wavelength, close to the one used in our study, requires particles size in the range of 190–200 nm.⁵⁵ Scheme B substrates show a median particle size that is closer to this range than that of Scheme A substrates, which explains the higher EF achieved on Scheme B substrates. Furthermore, particle agglomeration at ~60 min plating time causes red-shifting of the surface plasmon absorption band,⁵⁶ inducing additional electromagnetic enhancement of the Raman signal.

5.2.9. RSV Gene Detection

In order to test the efficacy of our Ag/nanoPPX films as platforms for biodetection, we prepared a molecular probe (MP)-based assay for RSV detection using SERS substrate prepared according to Scheme B using 60 min plating time. RSV is a virus that can cause serious infections in children and persons having weak or compromised immune systems; rapid testing and identification is of paramount importance in providing successful, prompt treatment. MPs are oligonucleotide probes that can report the presence of specific nucleic acids in homogenous solutions or on solid substrates.⁵⁷ There are several advantages of using MPs for DNA/RNA detection, including no target labeling, no need to wash after hybridization, and a single hybridization step (as compared to sandwich DNA/RNA assays).⁵⁸ MPs typically consist of the MP oligonucleotide sequence having a hairpin structure sensitive to a complementary target oligonucleotide present in the species to be detected and a fluorescent dye and quencher attached to the 3' and 5' ends, respectively, of that MP oligonucleotide. Our MP oligonucleotide sequence is complementary to RSV, and will specifically hybridize with RNA from our viral target, RSV. We selected Cy5 dye as the fluorophore that has an excitation peak close to the wavelengths of the Raman instrument (*i.e.*, 632 nm) and SC6 as the thiol linker to conjugate to our SERS substrates (Scheme 5-2).



Scheme 5-2. Molecular structures of Cy5-MP (left) and SC6 linker (right)

Detection of the hybridized and non-hybridized configurations of the MPs was performed by SERS studies of the fluorophores. Metalized nanoPPX substrate prepared *via* Scheme B was selected for RSV gene detection, due to its high EF and highly reproducible FBT SERS spectra, using the MP with a Cy5 fluorescent moiety and SC6 linker. Enhancement of the Raman signal of the Cy5 occurs *via* surface enhanced resonance Raman scattering because the excitation wavelength is close to the electronic transition of the fluorophore. Figures 5-9A (top plot) shows the SERS spectrum of the Cy5-MP-SC6 in non-hybridized configuration on Ag/nanoPPX substrate. When the probe hybridizes with a RSV target, the conformational reorganization separates the fluorophore from nanoparticles diminishing the SERS signal, as seen in Figures 5-9 (bottom plot).

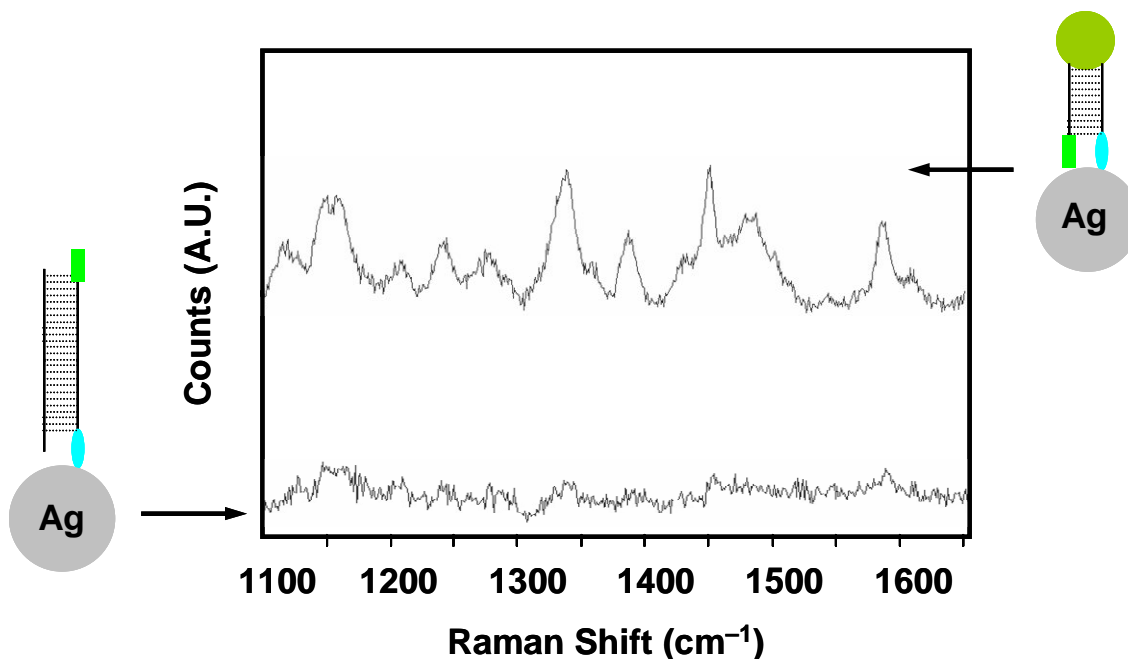


Figure 5-9. SERS spectrum of non-hybridized (top) and hybridized (bottom) Cy5-MP-SC6 molecular probe immobilized on Ag/nanoPPX (*via* Scheme B) substrate.

5.2.10. Summary

In this section, a comparative study on the SERS properties of Ag/nanoPPX substrates prepared *via* PD1 catalyst (using noncovalent ligand functionalization route) and a commercial (Pd/Sn-based) catalyst is presented. Electroless methods provide a significant advantage in that they allow selective metal deposition on catalyst sites, unlike vapor phase deposition where metal growth is largely unregulated. Using electroless methods, metal particle size and particle-particle separation can be tuned by controlling the size and surface coverage of the Pd-colloid used to catalyze the surface, thereby permitting EF optimization of each SERS substrate. In addition, use of an aromatic ligand (*e.g.*, pyridine) provides a means to anchor the metal particle on the nanoPPX surface,

resulting in improved stability and robustness of the substrate. Moreover, the ligand functionalization approach is particularly effective in mimicking the three-dimensional nano-architecture of the underlying nanoPPX template, thereby inducing additional Raman enhancement and allowing detection of large biomolecules.³⁶⁻³⁸

Substrates prepared *via* the ligand functionalization route were therefore employed for RSV gene detection using a MP modified with Cy5 fluorophore and SC6 linker. SERS spectrum of Cy5-MP-SC6 immobilized on Ag/nanoPPX clearly shows Cy5 peaks due to the proximity of the fluorophore to the Ag surface. In contrast, Cy5-MP-SC6 hybridized with RSV gene show diminished peaks due to the induced separation of the fluorophore from the Ag surface during hybridization. Such a methodology can therefore be used to detect oligonucleotide sequences with high selectivity and reproducibility (< 10% variation signal variation), and low detection limit ($\sim 10^{-10}$ M) and time (~ 10 s signal acquisition time).⁵⁹

5.3. Orthopaedic Implant Coatings

5.3.1. Introduction

Osteoporosis is a condition where the bone mineral density (BMD) is drastically reduced, microstructure of the bone is degraded, and the protein functions in bone are altered leading to a high susceptibility for bone-fracture. Osteoporosis can occur at any age and affects equally among all racial, gender and ethnic groups. Today, osteoporosis affects 10 million people in the US and an additional 34 million people are in a high-risk category due to their low BMD.⁶⁰ One out of every two women and one in four men over 50 will have an osteoporosis-related fracture in his or her lifetime.⁶⁰ Due to these overwhelming statistics, osteoporosis is responsible for more than 1.5 million bone fractures⁶⁰ and is expected to rise 300% over the next 60 years.⁶¹ Bone replacement surgery is typically carried out using stainless steel, Ti alloys, Co alloys etc having excellent load-bearing and corrosion resistance properties. However, these implants last only for 10–15 years in the body and the patient has to undergo surgery again.⁶² Such a lifespan may be acceptable for older patients but not for younger patients. “Fit and forget” has therefore been the most desired property of an orthopaedic implant.

The low lifespan of an implant is attributed to the poor apposition of the bone to the implant surface. The formation of bone–implant interface occurs in a number of stages, but can be broadly classified as osteoinduction, osteoconduction and osteointegration. Osteoinduction is the initial stage of bone growth where proteins from the surrounding blood and tissue fluids are adsorbed on the surface of the implant to form

a “conditioning” layer. Thereafter, mesenchymal stem cells from surrounding tissues grow on the surface, which later differentiates into bone-forming cells or osteoblasts.

The second stage, *i.e.*, osteoconduction refers to the growth of the bone (*via* osteoblast formation and proliferation) on the surface of the implant and incursion of blood-vessels into the trellis structure. Osteoconduction depend not only on the prior osteoinduction, but also on the biomaterial itself. For example, osteoconduction on known biocompatible materials such as stainless steel and titanium is significantly higher than non-biocompatible metals such as Ag or Cu. Furthermore, bone growth on seemingly similar materials such as commercially pure titanium and Ti-6Al-4V alloy was found to be drastically different.⁶³ Ti is known to form a passive TiO₂ oxide layer when exposed to ambient condition. It is well documented that this passive oxide layer on a metal implant undergoes electrochemical changes, both *in vivo* and *in vitro*.⁶⁴⁻⁶⁶ It was later postulated that such changes in the passive oxide layer on the implant surface play a crucial role in osteoconduction.⁶⁷

Finally, osteointegration, first conceptualized by Brånemark *et al.*, refers to the direct and stable anchorage between the bone and implant at an optical microscope level without any relative motion.⁶⁸ Osteointegration is not a separate event in itself, but is directly depended on the prior osteoinduction and osteoconduction. Osteointegration is affected by numerous factors that can be broadly classified as patient-related or implant-related. Patient-related factors include age, host-bone quality, anabolic growth factors, hormonal activity, smoking activity and osteoporosis. Additionally, surgery has to be performed such that the micro-motion of the implant is minimized; this is necessary to reduce any unfavorable effect on the osteointegration. Most of the patient-related factors

are unalterable for a particular patient and therefore their ability to improve the osteointegration is minimal. Much of the efforts today are directed at improving the osteointegration through modifications to the implant surface. Some of these techniques are discussed further.

Biochemical methods to modify the implant surfaces are being explored to improve the bone–implant interface. Some of the methodologies that have been tried include enhancement of osteoblasts activity *via* TGF- β_1 enhanced collagen synthesis,⁶⁹ improving osteoinduction *via* bone morphogenetic proteins (BMPs),⁷⁰ and increasing mitogenicity *via* biomolecules such as FGF-2⁷¹. Furthermore, effects of various physicochemical properties of the implant surface such as wettability, surface charge and surface chemistry on the osteointegration have also been studied. Surface composition modification of metal implant by coating bioceramics such as titania, alumina and hydroxyapatite has been shown to have favorable effect on osteointegration. However, the brittle nature of these ceramics makes them prone to cracking under *in situ* loading.⁷² Besides biochemical and physicochemical modifications of the implant surface, morphology of the implant surface is also a critical factor that influences osteointegration. Surface roughness not only provides mechanical interlocking with the bone, but also directs the motion of the osteoblasts in surfaces with grooves or pits.⁷³ Moreover, it is suggested that surface roughness, surface topography and surface composition may interactively influence both the selectivity of the initial protein layer that determines the osteoinduction process and the later calcification steps leading to bone-formation.⁷⁴ Broadly, improved bone-formation and proliferation are achieved when the implant surface “mimics” the surface morphology and chemistry of the host-

bone, though the precise mechanism through which it is achieved remains poorly understood.

In this thesis, the TiO₂/nanoPPX composite films prepared *via* the noncovalent ligand functionalization method, as described in Chapter 3, are employed as orthopaedic implant coatings. The noncovalent ligand functionalization strategy used in this work to fabricate TiO₂/nanoPPX composite films address two important problems of the current orthopaedic implant coatings: first, the problem of *in situ* cracking of ceramic coatings could be mitigated by inserting a flexible and robust “sandwich” layer (*i.e.*, the nanoPPX film) between the metal and the ceramic layer and second, the nanostructured morphology provide a favorable platform for osteoblast growth. PPX is an FDA-approved (USP Class VI) polymer and is therefore suitable for chronic implantation. Furthermore, the tunability of the nanostructured morphology of the underlying nanoPPX, and hence the TiO₂ layer due to the conformal nature of ceramization, could provide customized implant coatings per the structure of the host bone.

5.3.2. Experimental Procedure

TiO₂-coated planar and nanoPPX composite films were prepared according to the procedure described in Chapter 3. Briefly, helical nanoPPX and planar PPX films were functionalized with 0.5 M phenylphosphonic acid (aq) solution for 48 h, followed by treatment in TiO₂ LPD bath for 24 h. After removal from LPD bath, the TiO₂ coated nanoPPX films were then soaked in DI water for ~12 h to remove any residual phenylphosphonic acid and physisorbed TiO₂ particles. The films were then transported

to the Department of Orthopaedics at the Penn State Hershey Medical Center, Hershey, PA (Prof. Henry J. Donahue's Lab) in a sterile enclosure for cell-growth studies.

Human mesenchymal stem cells (hMSC) purchased from Cambrex Biosciences were cultured in a growth medium consisting of DMEM-low glucose (Invitrogen), 10% fetal bovine serum (FBS, Hyclone), 2 mM L-glutamine, and 1% penicillin-streptomycin (Cambrex Biosciences) kept in a humidified incubator at 37 °C and 5% CO₂. The growth medium was replaced every 3–4 days. After ~80% confluence, the cells were isolated in a 6-well tissue culture plate. Supplements consisting of dexamethasone, β -glycerophosphate, and ascorbate (Cambrex Biosciences) were then added to the growth medium to induce osteoblast differentiation. Subsequently, the cell-growth platforms were introduced in the plate wells. The differentiation medium was replaced twice a week. After 14 days, the differentiation medium was removed and the cell-growth platforms were washed with phosphate-buffered saline (PBS) three times. A 1 mL aqueous solution of 0.1% Alizarin Red S (Sigma-Aldrich, Cat# A-3757), a Ca-responsive indicator, was then added to each plate and samples were incubated for 10 min. Samples were then washed in H₂O twice. Thereafter, 1 mL of 100 mM cetylpyridinium chloride (Sigma-Aldrich, Cat# C-9002) was added to each sample. After 30 min incubation, the eluted Alizarin Red S solution was removed and its absorbance was measured at 570 nm using water as blank. The optical density was normalized with the surface area of each cell-growth platform for a comparative analysis of the extent of hMSC differentiation.

5.3.3. Results and Conclusions

Figure 5-10 shows the optical density at 570 nm of eluted Alizarin Red S from stained mineralized substrates. TiO₂/nanoPPX films show a ~9.5-fold higher density of hMSC differentiated into osteoblasts compared to a plate (polystyrene) control kept in the same differentiation medium. The surface roughness of the TiO₂ layer derived from the underlying nanoPPX nanomorphology plays an important role in enhancing the growth and differentiation of osteoblasts. Similar observations of enhanced bone growth on other nanomorphologies of TiO₂ and on other bioceramics have been reported.^{75,76} TiO₂ coated on a planar film too showed a ~5-fold higher density of hMSC differentiated into osteoblasts compared to the plate control. The enhanced differentiation of hMSC on TiO₂ coated planar PPX films is due to the presence of the TiO₂ nanoparticles on the planar PPX surface. One should however note from the discussion in Chapter 3 that these nanoparticles grow in patches on the surface and have poor interface adhesion with the underlying planar PPX substrate. Therefore, TiO₂-coated planar PPX are not suitable as orthopaedic implant coating, despite amplified hMSC differentiation. The density of mineralized cell density on a pristine nanoPPX film is not very different from that of the plate control, implying that surface chemistry plays a dominant role in the proliferation and differentiation process. Figure 5-11 shows the results of hMSC differentiation on three TiO₂/nanoPPX films prepared by varying the time in LPD bath. A steady increase in the optical density is observed indicating favorable growth of osteoblast as the quantity of TiO₂ in the composite increases.

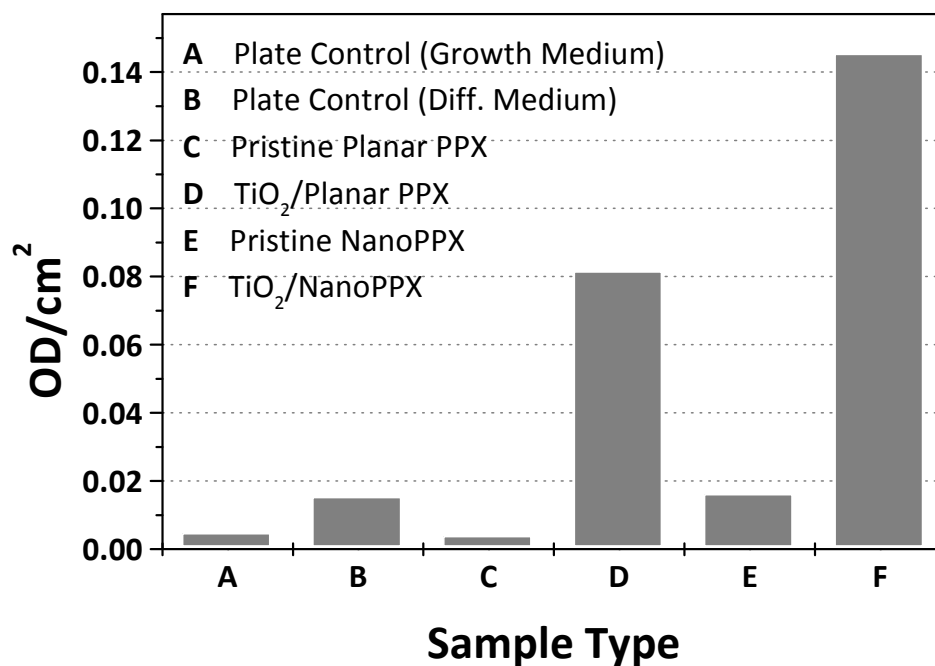


Figure 5-10. Differentiation of hMSCs to osteoblasts on various substrates kept in differentiation medium for 14 days. Cells were stained with a Ca-responsive indicator, Alizarin Red S. Optical density (OD) at 570 nm was used as a measure of the differentiation capacity for each substrate. Plate controls kept in basic and differentiation media are shown for comparison.

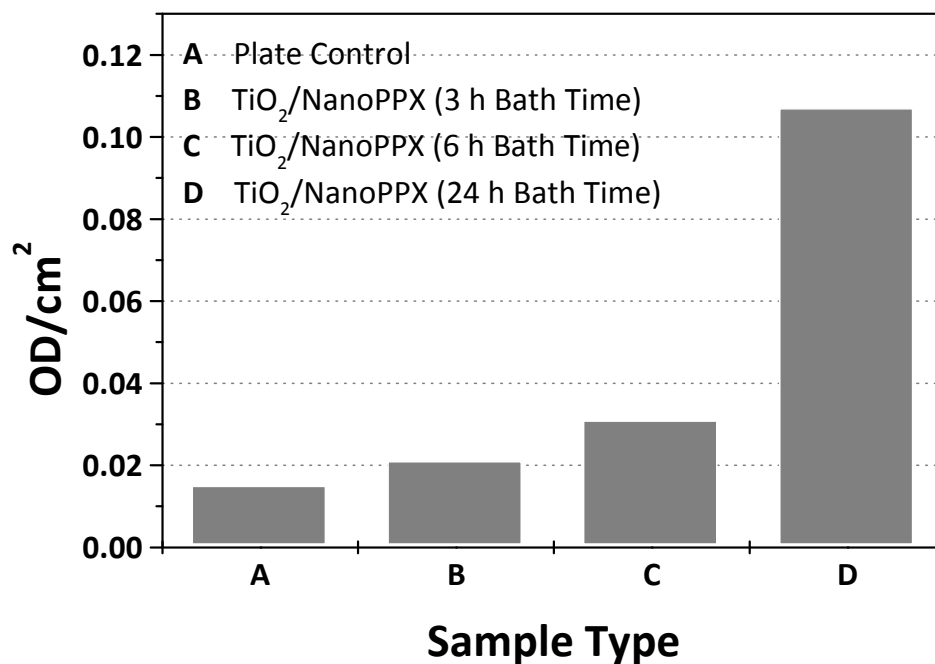


Figure 5-11. Differentiation of hMSCs to osteoblasts on TiO₂/nanoPPX surfaces (B to D) prepared by varying LPD bath time. Samples were kept in differentiation medium for 14 days before measurements. Plate control kept in differentiation medium (A) is shown for comparison.

Although it is difficult to draw detailed conclusions from these preliminary results, it is clear that TiO₂/nanoPPX composite films provide an effective platform for the growth and differentiation of bone cells compared to planar controls. Further studies are needed to analyze the repeatability of these experiments and to evaluate the adhesion of the osteoblasts to the coating surface.

References

1. www.eere.energy.gov/hydrogenandfuelcells/.
2. Schlapbach, L. & Zuttel, A. *Nature* **414**, 353-358 (2001).
3. Sakintuna, B., Lamari-Darkrim, F. & Hirscher, M. *International Journal of Hydrogen Energy* **32**, 1121-1140 (2007).
4. Orimo, S. I., Nakamori, Y., Eliseo, J. R., Zuttel, A. & Jensen, C. M. *Chemical Reviews* **107**, 4111-4132 (2007).
5. Varin, R. A., Czujko, T. & Wronski, Z. S. *Nanomaterials for solid state hydrogen storage* (Springer, New York ; London, 2009).
6. van den Berg, A. W. C. & Areal, C. O. *Chemical Communications*, 668-681 (2008).
7. Schlesinger, H. I. et al. *Journal of the American Chemical Society* **75**, 215-219 (1953).
8. Kojima, Y. et al. *International Journal of Hydrogen Energy* **27**, 1029-1034 (2002).
9. Amendola, S. C. et al. *International Journal of Hydrogen Energy* **25**, 969-975 (2000).
10. Amendola, S. C. et al. *Journal of Power Sources* **85**, 186-189 (2000).
11. Cakanyildirim, C. & Guru, M. *International Journal of Hydrogen Energy* **33**, 4634-4639 (2008).
12. Kojima, Y. & Haga, T. *International Journal of Hydrogen Energy* **28**, 989-993 (2003).

13. Park, E. H. et al. *International Journal of Hydrogen Energy* **32**, 2982-2987 (2007).
14. Demirci, U. B., Akdim, O. & Miele, P. *International Journal of Hydrogen Energy* **34**, 2638-2645 (2009).
15. Liu, B. H., Li, Z. P., Morigasaki, N. & Suda, S. *International Journal of Hydrogen Energy* **33**, 1323-1328 (2008).
16. Ture, E. I., Tabakoglu, F. O. & Kurtulus, G. in *16th World Hydrogen Energy Conference* (Lyon, France, 2006).
17. <http://merit.hydrogen.co.jp/>.
18. Lee, K. in *8th World Renewable Energy Congress* (Denver, CO, 2004).
19. Markowitz, M., Baral, S., Brandow, S. & Singh, A. *Thin Solid Films* **224**, 242-247 (1993).
20. Rhee, C. K. et al. *Langmuir* **25**, 7140-7147 (2009).
21. Malvadkar, N., Park, S., Urquidi-MacDonald, M., Wang, H. & Demirel, M. C. *Journal of Power Sources* **182**, 323-328 (2008).
22. Jeong, S. U. et al. *International Journal of Hydrogen Energy* **32**, 1749-1754 (2007).
23. Wu, C., Zhang, H. M. & Yi, B. L. *Catalysis Today* **93-5**, 477-483 (2004).
24. Lee, J. et al. *Catalysis Today* **120**, 305-310 (2007).
25. Sartbaeva, A., Kuznetsov, V. L., Wells, S. A. & Edwards, P. P. *Energy & Environmental Science* **1**, 79-85 (2008).
26. <http://www.nrel.gov/docs/gen/fy08/42220.pdf>.

27. Fleischm.M, Hendra, P. J. & McQuilla.Aj. *Chemical Physics Letters* **26**, 163-166 (1974).
28. Jeanmaire, D. L. & Vanduyne, R. P. *Journal of Electroanalytical Chemistry* **84**, 1-20 (1977).
29. Albrecht, M. G. & Creighton, J. A. *Journal of the American Chemical Society* **99**, 5215-5217 (1977).
30. Orendorff, C. J., Gole, A., Sau, T. K. & Murphy, C. J. *Analytical Chemistry* **77**, 3261-3266 (2005).
31. Tian, Z. Q. et al. *Faraday Discussions* **132**, 159-170 (2006).
32. Wang, T., Hu, X. G. & Dong, S. J. *Journal of Physical Chemistry B* **110**, 16930-16936 (2006).
33. Sztainbuch, I. W. *Journal of Chemical Physics* **125** (2006).
34. Blatchford, C. G., Campbell, J. R. & Creighton, J. A. *Surface Science* **120**, 435-455 (1982).
35. Grabar, K. C. et al. *Journal of the American Chemical Society* **118**, 1148-1153 (1996).
36. Lu, L. H. et al. *Chemistry of Materials* **17**, 5731-5736 (2005).
37. Kahraman, M., Aydin, O. & Culha, M. *Chemphyschem* **10**, 537-542 (2009).
38. Wang, T., Hu, X. G., Wang, J. L. & Dong, S. J. *Talanta* **75**, 455-460 (2008).
39. Kuncicky, D. M., Christesen, S. D. & Velev, O. D. *Applied Spectroscopy* **59**, 401-409 (2005).
40. Aroca, R. F., Goulet, P. J. G., dos Santos, D. S., Alvarez-Puebla, R. A. & Oliveira, O. N. *Analytical Chemistry* **77**, 378-382 (2005).

41. Goulet, P. J. G., dos Santos, D. S., Alvarez-Puebla, R. A., Oliveira, O. N. & Aroca, R. F. *Langmuir* **21**, 5576-5581 (2005).
42. Deng, S. et al. *Nanotechnology* **20** (2009).
43. Kao, P. et al. *Advanced Materials* **20**, 3562-3565 (2008).
44. Ko, H., Chang, S. & Tsukruk, V. V. *Acs Nano* **3**, 181-188 (2009).
45. Amezcua-Correa, A. et al. *Advanced Functional Materials* **17**, 2024-2030 (2007).
46. Cetinkaya, M., Malvadkar, N. & Demirel, M. C. *Journal of Polymer Science Part B-Polymer Physics* **46**, 640-648 (2008).
47. Demirel, M. C. et al. *Biointerphases* **4**, 35-41 (2009).
48. Demirel, M. C., Cetinkaya, M., Singh, A. & Dressick, W. J. *Advanced Materials* **19**, 4495-4499 (2007).
49. Malvadkar, N., Sekeroglu, K., Dressick, W. J. & Demirel, M. C. *Langmuir* **26**, 4382-4391 (2010).
50. Dressick, W. J. et al. *Colloids and Surfaces a-Physicochemical and Engineering Aspects* **108**, 101-111 (1996).
51. Brandow, S. L., Dressick, W. J., Marrian, C. R. K., Chow, G. M. & Calvert, J. M. *Journal of the Electrochemical Society* **142**, 2233-2243 (1995).
52. Dobisz, E. A., Bass, R., Brandow, S. L., Chen, M. S. & Dressick, W. J. *Applied Physics Letters* **82**, 478-480 (2003).
53. Dixon, M. C. et al. *Langmuir* **23**, 2414-2422 (2007).
54. Szafranski, C. A., Tanner, W., Laibinis, P. E. & Garrell, R. L. *Langmuir* **14**, 3580-3589 (1998).

55. Emery, S. R., Haskins, W. E. & Nie, S. M. *Journal of the American Chemical Society* **120**, 8009-8010 (1998).
56. Ung, T., Liz-Marzan, L. M. & Mulvaney, P. *Journal of Physical Chemistry B* **105**, 3441-3452 (2001).
57. Tyagi, S. & Kramer, F. R. *Nature Biotechnology* **14**, 303-308 (1996).
58. Strohsahl, C. M., Miller, B. L. & Krauss, T. D. *Nature Protocols* **2**, 2105-2110 (2007).
59. Malvadkar, N. et al., In Preparation (2010).
60. www.nof.org.
61. Palin, E., Liu, H. N. & Webster, T. J. *Nanotechnology* **16**, 1828-1835 (2005).
62. Emery, D. F. G., Clarke, H. J. & Grover, M. L. *Journal of Bone and Joint Surgery-British Volume* **79B**, 240-246 (1997).
63. Johansson, C. B., Han, C. H., Wennerberg, A. & Albrektsson, T. *International Journal of Oral & Maxillofacial Implants* **13**, 315-321 (1998).
64. Sundgren, J. E., Bodo, P. & Lundstrom, I. *Journal of Colloid and Interface Science* **110**, 9-20 (1986).
65. Sundgren, J. E., Bodo, P., Lundstrom, I., Berggren, A. & Hellem, S. *Journal of Biomedical Materials Research* **19**, 663-671 (1985).
66. Pan, J., Thierry, D. & Leygraf, C. *Electrochimica Acta* **41**, 1143-1153 (1996).
67. Albrektsson, T. et al. *Annals of Biomedical Engineering* **11**, 1-27 (1983).
68. Branemark, P. I. et al. *Scandinavian Journal of Plastic and Reconstructive Surgery and Hand Surgery*, 7-132 (1977).
69. Rosen, D. et al. *Bone* **15**, 355-359 (1994).

70. Groeneveld, E. H. J. & Burger, E. H. *European Journal of Endocrinology* **142**, 9-21 (2000).
71. Mohan, S. & Baylink, D. J. *Clinical Orthopaedics and Related Research*, 30-48 (1991).
72. Bauer, T. W., Taylor, S. K., Jiang, M. & Medendorp, S. V. *Clinical Orthopaedics and Related Research*, 11-18 (1994).
73. Chehroudi, B., McDonnell, D. & Brunette, D. M. *Journal of Biomedical Materials Research* **34**, 279-290 (1997).
74. Schwartz, Z. & Boyan, B. D. *Journal of Cellular Biochemistry* **56**, 340-347 (1994).
75. Popat, K. C., Leoni, L., Grimes, C. A. & Desai, T. A. *Biomaterials* **28**, 3188-3197 (2007).
76. Popat, K. C. et al. *Journal of Biomedical Materials Research Part A* **80A**, 955-964 (2007).

Chapter 6. Conclusions and Recommendations for Future Work

In this thesis, a methodology to fabricating nanoPPX-templated hybrid nanostructures of metals and ceramics *via* noncovalent functionalization is presented, the mechanism of ligand intake in the nanoPPX film is established and applications of these hybrid nanostructures in hydrogen storage, biodetection and biomedical coatings are explored. The oblique angle polymerization (OAP) technique developed by our research group is a template-free, non-lithographic approach for preparing structure-controlled nanomorphologies of polymers. This work constitutes a continued research effort of our group in augmenting the advantages of the OAP method for application in cutting-edge technologies. Furthermore, wet chemical routes, such as those used for depositing metal or ceramic nanoparticles in this work, are also favorable for use in a manufacturing environment.

Noncovalent functionalization of polymers prepared by OAP has several advantages over conventional covalent functionalization techniques, including: 1) noncovalent bonds are reversible and therefore have the ability to reversibly functionalize the surface without adversely affecting the material's desirable physicochemical properties; 2) a generic nanoPPX template is versatile and can create a family of porous materials, including metals¹ and ceramics², using an appropriate ligand and/or deposition bath; and 3) due to the presence of high energy surfaces in nanoPPX films, the ligand adsorption is readily controlled and temporally stable under ambient conditions.³

NanoPPX-based hybrid nanostructures prepared *via* the noncovalent functionalization show several structural and physical commonalities. For example, the growth of metal (or ceramic) layer is conformal to the underlying nanorod morphology of a nanoPPX film due to penetration of ligand along the thickness of the nanoPPX film. In addition, the polymer/metal composite structure does not show any signs of adhesive weakness, although the metal nanoparticles are stabilized by noncovalent forces.³ Such a counterintuitive behavior is ascribed to the expected mechanical interlocking between the deposited metal and the polymer nanostructure, as well as the larger number of noncovalent interactions as noted elsewhere for analogous noncovalent based systems.⁴

Gas and pyridine physisorption studies used for investigating the mechanism of noncovalent ligand functionalization illustrate that irreversible stabilization of aromatic ligands is facilitated by the large amount of micropores present in the nanoPPX structure. However, the investigation assumes that physisorption occurs uniformly along the length of nanorods. In other words, structural properties of a planar and nanoPPX films are considered to be homogeneous along the film thickness. Although such an assumption is highly plausible, experimental evidence exists for thickness-dependent structural properties in a polymeric film.^{5,6} Therefore, an in-depth study taking into account the effect of thickness of the nanoPPX film is required to confirm the conclusions derived from the experimental data of the physisorption studies.

NanoPPX-based hybrid nanostructures have promising applications in various emerging technologies, as discussed in the preceding chapter. We demonstrated that modification of porosity both at the polymer deposition and metal plating stages profoundly impacts the catalytic activity of the Co/nanoPPX composites. Analogous

approach could be applied to improve the performances of the other applications mentioned in this thesis. For instance, maximization of the “hot-spot” density, and therefore the enhancement factor, of a Ag/nanoPPX SERS substrate can be accomplished by controlling of the inter-nanorod spacing and using appropriate size of the Pd catalyst. The preliminary cell-growth studies on TiO₂/nanoPPX surfaces need to be extended to include biochemical surface modifications (described in Chapter 5) and the tunability aspect of the nanoPPX morphology to improve hMSC differentiation and bone–TiO₂ interface adhesion. Besides the applications discussed in this thesis, other potential applications of the noncovalent functionalization methodology may include drug-eluting platforms,⁷ and anti-reflecting coatings, among others. The ability to control the nanostructured morphology and interfacial properties of the material layer coating the nanoPPX film is a prerequisite in all these applications. Continued efforts to better understand the properties of these hybrid systems are therefore needed to encourage the development of the present and emergence of new applications.

Challenges also lie in extending the generality of this method of functionalization to nanostructured polymeric materials prepared *via* routes besides OAP and polymer chemistries other than poly(*p*-xylylenes). Conformal metallization of novel hierarchal structures with nanosized organic building-blocks (*e.g.*, block copolymers), in combination with continuous and robust interface obtained *via* the noncovalent functionalization can open up newer applications in cutting-edge technologies. Feasibility for successful application of noncovalent functionalization in other polymer/ligand systems however entails the presence of micropores/surface disorder in the polymer structure, as realized in this thesis.

References

1. Malvadkar, N., Park, S., Urquidi-MacDonald, M., Wang, H. & Demirel, M. C. *Journal of Power Sources* **182**, 323-328 (2008).
2. Malvadkar, N., Dressick, W. J. & Demirel, M. C. *Journal of Materials Chemistry* **19**, 4796-4804 (2009).
3. Demirel, M. C., Cetinkaya, M., Singh, A. & Dressick, W. J. *Advanced Materials* **19**, 4495-4499 (2007).
4. Chen, M. S., Brandow, S. L., Schull, T. L., Chrisey, D. B. & Dressick, W. J. *Advanced Functional Materials* **15**, 1364-1375 (2005).
5. Liang, Y. R., Zheng, M. Z., Park, K. H. & Lee, H. S. *Polymer* **49**, 1961-1967 (2008).
6. Knaapila, M. et al. *Journal of Physical Chemistry B* **107**, 12425-12430 (2003).
7. Anderson, M. K. in *Controlling the Adsorption of Proteins on Poly(p-xylylene) Polymeric Thin Films* (Masters Thesis, Pennsylvania State University, Engineering Science and Mechanics, University Park, 2010).

Appendix A. Statistical Analysis of Ni Film Roughness Variations*

This material summarizes the statistical analysis of the two-level factorial design exploring the effects of the plating variables and their interactions on the roughness of the plated Ni film. The variables studied, with upper and lower limits explored here coded as +1 and -1, respectively, are shown in Table A-1. Additional details are found in Chapter 2, Section 2.5.

Table A-1. Variables Considered in the Electroless Metallization of the Nanostructured PPX-CI Substrates

Variable Designation	Variable Description	Lower (-1) Level	Upper (+1) Level
N	Electroless Ni bath plating time	30 min	60 min
C	PD1 catalyst treatment time	45 min	90 min
L	Pyridine ligand treatment time	30 h	48 h
F	Pyridine ligand treatment conditions	Pyridine aqueous solution	Pyridine vapor

Table A-2 illustrates the results for the 16 coded electroless Ni plating experiments describing the two-level factorial design based on the 4 variables considered in Table A-1.

* Reproduced with permission from Malvadkar *et al.*, *Langmuir* **26**, 4382–4391 (2010). DOI: 10.1021/la9034529. Copyright 2010 American Chemical Society.

Table A-2. Summary of the Factorial Design Experiment and Ni Roughness Results

Experiment Number	Variables				Ni Film Roughness Measurements (nm)						Average Roughness R_{ave} (nm)
	N	C	L	F	R_1	R_2	R_3	R_4	R_5	R_6	
1	-1	-1	-1	-1	43.2	45.18	44.28	44.45	–	–	44.2775
2	1	-1	-1	-1	39.22	38.37	39.62	–	–	–	39.07
3	-1	1	-1	-1	30.05	29.49	29.76	–	–	–	29.76667
4	1	1	-1	-1	26.47	24.9	25.14	–	–	–	25.50333
5	-1	-1	1	-1	32.75	34.69	33.25	–	–	–	33.56333
6	1	-1	1	-1	30.07	31.72	28.15	–	–	–	29.98
7	-1	1	1	-1	24.88	25.52	24.68	–	–	–	25.02667
8	1	1	1	-1	29.68	32.51	35.56	33.66	–	–	32.8525
9	-1	-1	-1	1	44.46	48.32	46.44	48.05	49.23	49.93	47.73833
10	1	-1	-1	1	58.79	64.19	59.3	55.77	58.81	58.85	59.285
11	-1	1	-1	1	44.3	44.58	43.02	44.74	47.08	38.12	43.64
12	1	1	-1	1	34.62	33.37	31.72	33.61	35.06	35.01	33.89833
13	-1	-1	1	1	51.83	51.23	43.13	46.19	50.9	46.6	48.31333
14	1	-1	1	1	53.66	49.19	53.63	56.38	53.21	51	52.85
15	-1	1	1	1	34.12	36.54	32.82	32.74	34.09	32.08	33.73167
16	1	1	1	1	53.3	47.83	52.54	50.65	55.67	42.27	50.37667

Each row in Table A-2 represents a separate experiment, performed in random order, for the factorial design at the coded levels from Table A-1 shown for each variable. Roughness values measured by AFM for electroless Ni deposited in each experiment are listed, together with the average roughness calculated for the experiment, in each line of Table A-2. From Table A-2, a total of $N = 74$ Ni film roughness measurements were made, as shown by the entries of the R_i ($i = 1-6$) columns. The grand average roughness $= 41.57054 \text{ nm} = 41.57 \text{ nm}$ is calculated as the average of all 74 roughness measurements

Table A-3. Table of Contrasts for the Electroless Ni Film Roughness Measurements

E	Sum	D	Variables and Variable Interactions															
			X	of the	A												N	
P	R _i	T												N	N	N	C	C
T	(nm)	A					N	N	C	N	C	L	C	C	L	L	L	
			N	C	L	F	C	L	L	F	F	F	L	F	F	F	F	
1	177.11	4	-1	-1	-1	-1	1	1	1	1	1	1	-1	-1	-1	-1	1	
2	117.21	3	1	-1	-1	-1	-1	-1	1	-1	1	1	1	1	1	-1	-1	
3	89.3	3	-1	1	-1	-1	-1	1	-1	1	-1	1	1	1	-1	1	-1	
4	76.51	3	1	1	-1	-1	1	-1	-1	-1	-1	1	-1	-1	1	1	1	
5	100.69	3	-1	-1	1	-1	1	-1	-1	1	1	-1	1	-1	1	1	-1	
6	89.94	3	1	-1	1	-1	-1	1	-1	-1	1	-1	-1	1	-1	1	1	
7	75.08	3	-1	1	1	-1	-1	-1	1	1	-1	-1	-1	1	1	-1	1	
8	131.41	4	1	1	1	-1	1	1	1	-1	-1	-1	1	-1	-1	-1	-1	
9	286.43	6	-1	-1	-1	1	1	1	1	-1	-1	-1	-1	1	1	1	-1	
10	355.71	6	1	-1	-1	1	-1	-1	1	1	-1	-1	1	-1	-1	1	1	
11	261.84	6	-1	1	-1	1	-1	1	-1	-1	1	-1	1	-1	1	-1	1	
12	203.39	6	1	1	-1	1	1	-1	-1	1	1	-1	-1	1	-1	-1	-1	
13	289.88	6	-1	-1	1	1	1	-1	-1	-1	1	1	1	1	-1	-1	1	
14	317.07	6	1	-1	1	1	-1	1	-1	1	-1	1	-1	-1	1	-1	-1	
15	202.39	6	-1	1	1	1	-1	-1	1	-1	1	1	-1	-1	-1	1	-1	
16	302.26	6	1	1	1	1	1	1	1	1	1	1	1	1	1	1	1	

Table A-3 and Table A-4 summarize the calculations of the effects for each variable and variable interaction.¹ Table A-3 illustrates the Table of Contrast information required for calculation of the Effects for the Ni roughness data in Table A-4. Column 1 of Table A-3 again indicates the experiment number, column 2, labeled “**Sum of the R_i**”, provides the sum of the roughness data from Table A-2 for a given experiment, and column 3, labeled “**DATA**”, provides the number of roughness measurements used to calculate the “**Sum of the R_i**” value. For example, in Experiment 1 in Table A-3 the “**Sum of the R_i**” = 43.20 + 45.18 + 44.28 + 44.45 = 177.11 nm from the “**DATA**” = 4 roughness values taken from Table A-2. The remaining columns in Table A-3 summarize the coded levels of the four variables and all possible variable interactions. Coded levels for the various interactions are determined by multiplying the appropriate

row elements of the interacting variables for each experiment. For example, the $NC = N \times C = +1$ interaction for experiment 1 is found by multiplying the values of N (*i.e.*, -1) and C (*i.e.*, -1). For experiment 2, $NC = -1 = N \times C = (+1) \times (-1)$. Values for other interactions are generated in similar fashion.

Table A-4. Calculation of the Effects for the Electroless Ni Roughness

Total R (+)	Total Data (+)	Total R (-)	Total Data (-)	Average R (+)	Average R (-)	Effect E	Effect ID
1593.50	37	1482.72	37	43.06757	40.07351	2.994054	N
1342.18	37	1734.04	37	36.27514	46.86595	-10.5908	C
1508.72	37	1567.50	37	40.77622	42.36486	-1.58865	L
2218.97	48	857.25	26	46.22854	32.97115	13.25739	F
1567.68	38	1508.54	36	41.25474	41.90389	-0.64915	NC
1655.36	38	1420.86	36	43.56211	39.46833	4.093772	NL
1647.60	38	1428.62	36	43.35789	39.68389	3.674006	CL
1620.61	37	1455.61	37	43.80027	39.34081	4.459459	NF
1454.83	37	1621.39	37	39.31973	43.82135	-4.50162	CF
1571.73	37	1504.49	37	42.47919	40.66189	1.817297	LF
1648.30	37	1427.92	37	44.54865	38.59243	5.956216	NCL
1453.49	36	1622.73	38	40.37472	42.70342	-2.3287	NCF
1537.09	36	1539.13	38	42.69694	40.50342	2.193523	NLF
1503.23	36	1572.99	38	41.75639	41.39447	0.361915	CLF
1628.33	37	1447.89	37	44.00892	39.13216	4.876757	NCLF

The Table of Contrasts is used to calculate the Effect, “E”, shown in Table A-4 for each variable and variable interaction. For a given variable or variable interaction in Table A-3, the values from the “Sum of the R_i ” column corresponding to the +1 level of that variable or variable interaction are added and placed in the column labeled “**Total R(+)**” in Table A-4. Corresponding values from the “DATA” column in Table A-3 are added and placed in the column labeled “**Total Data(+)**” in Table A-4. An average for the +1 level of the variable or variable interaction, calculated by dividing the “Total R(+)” value by the “Total Data(+)” value, is shown in the column labeled “**Average R(+)**” in Table A-4. Corresponding values for the -1 level of the same variable or variable interaction are calculated and summarized in columns labeled “**Total R(-)**”,

“**Total Data(-)**”, and “**Average R(-)**”, respectively, in Table A-4. The Effect, “E”, for each variable or variable interaction in Table A-4 is then calculated as the difference between the average values, as shown in Equation (1):

$$E = \text{Average R(+)} - \text{Average R(-)} \quad (\text{A-1})$$

For example, for the NC interaction the +1 level in Table A-3 corresponds to “Sum the R_i” and “DATA” values in rows (*i.e.*, “EXPT”) 1, 4, 5, 8, 9, 12, 13, and 16. The calculation of the “Total R(+)”, “Total Data(+)”, and “Average R(+)” values are summarized in Equations (A-2), (A-3), and (A-4), respectively:

$$\begin{aligned} \text{Total R(+)} &= 177.11 + 76.51 + 100.69 + 131.41 + 286.43 + 203.39 + \\ &289.88 + 302.26 = 1567.68 \end{aligned} \quad (\text{A-2})$$

$$\text{Total Data(+)} = 4 + 3 + 3 + 4 + 6 + 6 + 6 + 6 = 38 \quad (\text{A-3})$$

$$\text{Average R(+)} = 1567.68 / 38 = 41.25474 \text{ nm} \quad (\text{A-4})$$

The “Sum the R_i” and “DATA” values in rows (*i.e.*, “EXPT”) 2, 3, 6, 7, 10, 11, 14, and 15 correspond to the -1 level of the NC interaction in Table A-3. The calculation of the “Total R(-)”, “Total Data(-)”, and “Average R(-)” values are summarized in Equations (A-5), (A-6), and (A-7), respectively, and the NC effect is given by Equation (A-8):

$$\begin{aligned} \text{Total R(-)} &= 117.21 + 89.3 + 89.94 + 75.08 + 355.71 + 261.84 + \\ &317.07 + 202.39 = 1508.54 \end{aligned} \quad (\text{A-5})$$

$$\text{Total Data(-)} = 3 + 3 + 3 + 3 + 6 + 6 + 6 + 6 = 36 \quad (\text{A-6})$$

$$\text{Average R(-)} = 1508.54 / 36 = 41.90389 \quad (\text{A-7})$$

$$E = \text{Effect N} \times \text{C} = 41.25474 - 41.90389 = -0.64915 \quad (\text{A-8})$$

Effects summarized in Table A-4 for the other variables and variable interactions are calculated in an analogous manner.

The significance of the effects calculated in Table A-4 is evaluated *via* the analysis of variance (ANOVA) method as described in the literature.² The null hypothesis tested in each case is that a given effect is not significant. Briefly, testing is accomplished by comparing the variance (σ^2) calculated as the mean square error (MSE) from the pooled runs to the variance calculated as the mean square between (MSB) runs. The F-distribution is then used to determine with a given probability (*i.e.*, 99%) whether significant differences between the variances are observed or not. If an effect, E, is not significant (*i.e.*, the null hypothesis is true), no significant differences between the variances are observed. Therefore, MSE and MSB are independent estimates of σ^2 and their ratio $F_0 = \text{MSB}/\text{MSE} \sim 1.0$ has an F-distribution. In contrast, if an effect is significant then the variance estimated *via* MSB exceeds that estimated by MSE and the ratio $F_0 = \text{MSB}/\text{MSE} > 1.0$. In this case, the F-distribution provides an F_c (p , DF_{MSB} , DF_{MSE}) value, where “p” is the probability that F_0 is large because the effect is truly significant (rather than due to random error), DF_{MSB} is the degrees of freedom for the MSB, and DF_{MSE} is the degrees of freedom for the MSE, that permits assessment of the validity of the null hypothesis. For our two-level factorial design, $DF_{\text{MSB}} = 1$ (*i.e.*, number of variable levels minus one) and $DF_{\text{MSE}} = 58$ (*i.e.*, the sum of the DF for each experiment, which corresponds to “Y” in Table A-5 below).² If $F_0 < F_c$, it can be stated with ($p =$) 99% confidence that the null hypothesis is accepted and the effect is not significant (*i.e.*, it is due to random error). On the other hand, if $F_0 > F_c$, the effect, E, is significant with ($p =$) 99% confidence. The calculations of MSE and the MSB and F_0 necessary to carry out the ANOVA for our system are summarized in Table A-5 and Table A-6 below.

Table A-5 summarizes information needed to calculate the MSE. These include calculations of the sample variance, “S”, and the number of degrees of freedom, “DF”, for each experiment. Values for “S” and “DF” are defined by Equations (A-9) and (A-10), respectively:

$$S = \sum_{i=1 \text{ to } q} (R_i - R_{ave})^2 / (q - 1) \quad (\text{A-9})$$

$$DF = q - 1 \quad (\text{A-10})$$

In Equations (A-9) and (A-10), “q” is the total number of roughness measurements made for each particular experiment. At the bottom of Table A-5, values for the sum of the DF, designated “Y”, and the sum of the “DF × S”, designated “Z”, for all experiments are also listed. The MSE for our system is then given by the ratio of “Z” and “Y” according to Equation (A-11):

$$MSE = Z/Y = 6.216445 \quad (\text{A-11})$$

Table A-5. Calculation of Factors Required for ANOVA for the Ni Roughness Results

Ni Film Roughness Measurements (nm)						R _{ave} (nm)	S	DF	DF × S
R ₁	R ₂	R ₃	R ₄	R ₅	R ₆				
43.2	45.18	44.28	44.45	–	–	44.2775	0.668425	3	2.005275
39.22	38.37	39.62	–	–	–	39.07	0.4075	2	0.815
30.05	29.49	29.76	–	–	–	29.76667	0.078433	2	0.156867
26.47	24.9	25.14	–	–	–	25.50333	0.715233	2	1.430467
32.75	34.69	33.25	–	–	–	33.56333	1.014533	2	2.029067
30.07	31.72	28.15	–	–	–	29.98	3.1923	2	6.3846
24.88	25.52	24.68	–	–	–	25.02667	0.192533	2	0.385067
29.68	32.51	35.56	33.66	–	–	32.8525	6.054892	3	18.16468
44.46	48.32	46.44	48.05	49.23	49.93	47.73833	3.979417	5	19.89708
58.79	64.19	59.3	55.77	58.81	58.85	59.285	7.41487	5	37.07435
44.3	44.58	43.02	44.74	47.08	38.12	43.64	9.04352	5	45.2176
34.62	33.37	31.72	33.61	35.06	35.01	33.89833	1.642697	5	8.213483
51.83	51.23	43.13	46.19	50.9	46.6	48.31333	12.37515	5	61.87573
53.66	49.19	53.63	56.38	53.21	51	52.85	6.13462	5	30.6731
34.12	36.54	32.82	32.74	34.09	32.08	33.73167	2.541697	5	12.70848
53.3	47.83	52.54	50.65	55.67	42.27	50.37667	22.70471	5	113.5235
–	–	–	–	–	–	Y = Sum of DF column entries = 58			–
–	–	–	–	–	–	Z = Sum of (DF × S) column entries = 360.5544			–

Table A-6 summarizes the calculation of the MSB and F_0 values and the evaluation of the significance of each effect, E. For the two-level factorial design, the MSB in Table A-6 are given by Equation (A-12), where $N = 74$ is the total number of roughness measurements made:²

$$MSB = N \cdot E^2/4 = 74 \cdot E^2/4 \quad (\text{A-12})$$

The F_0 values are calculated from Equation (A-13):

$$F_0 = MSB/MSE \quad (\text{A-13})$$

From the literature,² the appropriate F-distribution value of F_c for $p = 99\%$ confidence is $F_c(0.99, 1, 58)$. However, because F_c values for $DF_{MSE} = 58$ are not available in our F-distribution Table, we use the nearest and more conservative listed F_c value of $F_c(0.99, 1, 40) = 7.21$, cited for $DF_{MSB} = 1$ and $DF_{MSE} = 40$, as a substitute. Comparison of the F_0 values in Table A-6 with this F_c value shows that 14 of the 16 variables and variable interactions are significant at the 99% confidence level (*i.e.*, $F_0/F_c > 1$; $F_0 > F_c$). Only the NC and CLF variable interactions are not significant (*i.e.*, $F_0/F_c < 1$; $F_0 < F_c$ so they can be attributed to random error).

Table A-6. Calculation of the MSB and F_0 and the Significance of the Effects

Effect ID	Effect	MSB	F_0	$F_0/F_c(0.99, 1, 40)$	Significance (Confidence)
N	2.994054	165.8407	26.67769	3.649479	YES (99%)
C	-10.5908	2075.058	333.8008	45.66358	YES (99%)
L	-1.58865	46.69038	7.510773	1.027466	YES (99%)
F	13.25739	3251.529	523.052	71.55294	YES (99%)
NC	-0.64915	7.79587	1.25407	0.171555	NO
NL	4.093772	310.0409	49.87423	6.82274	YES (99%)
CL	3.674006	249.7189	40.17063	5.495298	YES (99%)
NF	4.459459	367.9054	59.18251	8.096102	YES (99%)
CF	-4.50162	374.895	60.30689	8.249916	YES (99%)
LF	1.817297	61.09754	9.828356	1.344508	YES (99%)
NCL	5.956216	656.3155	105.5771	14.44284	YES (99%)
NCF	-2.3287	100.3225	16.13822	2.207691	YES (99%)
NLF	2.193523	89.01358	14.31903	1.958827	YES (99%)
CLF	0.361915	2.423178	0.389801	0.053324	NO
NCLF	4.876757	439.981	70.77683	9.682193	YES (99%)

Appendix A References

1. Box, G.E.P.; Hunter, W.G.; Hunter, J.S. *Statistics for Experimenters: An Introduction to Design, Data Analysis, and Model Building*; John Wiley & Sons: New York, 1978; Ch. 10.
2. Schmidt, S.R.; Launsby, R.G. *Understanding Industrial Designed Experiments*, 3rd Ed.; Air Academy Press: Colorado Springs, CO, 1992, Ch. 4.

Appendix B. Gas Physisorption:

Background and Theory

Physisorption of probe gases such as N₂, Ar, He or CO₂ at constant temperature is routinely used to characterize the structure of a material. The resultant adsorption isotherm gives abundant information including the nature of porosity, surface area, pore volume, and adsorption enthalpies, among others. The IUPAC classifies porosity in a material into three types according to the pore width: microporosity (≤ 2 nm), mesoporosity (2–50 nm) and macroporosity (≥ 50 nm). The classification, as it may seem, is not arbitrary and profoundly affects the gas adsorption behavior of the material. For instance, gas adsorption in a mesoporous material shows a distinct capillary condensation effect. On the other hand, adsorption in microporous and macroporous materials occurs *via* micropore filling and multilayer adsorption mechanisms, respectively. We now discuss some of the commonly used models and methods to evaluate the three types of porosity in a material.

B.1. BET Surface Area

In 1938, Stephen Brunauer, Paul Emmett, and Edward Teller extended the Langmuir adsorption theory to account for multilayer adsorption on the surface.¹ The primary assumption of the BET theory is that the enthalpy of adsorption of the second

(and subsequent) layers is equal to the heat of liquefaction (ΔH_L) of the adsorbate. The resulting isotherm can be expressed as

$$\left[Q \left(\frac{p}{p_0} - 1 \right) \right]^{-1} = \frac{c-1}{Q_m c} \left(\frac{p}{p_0} \right) + \frac{1}{Q_m c} \quad (\text{B-1})$$

where, Q is the amount of gas adsorbed, Q_m is the amount of gas required to form a monolayer and c is a quantity expressed as

$$c = \exp \left(\frac{\Delta H_1 - \Delta H_L}{RT} \right) \quad (\text{B-2})$$

where, ΔH_1 is the enthalpy of adsorption of the first layer. The plot of $\left[Q \left(\frac{p}{p_0} - 1 \right) \right]^{-1}$ vs.

$\left(\frac{p}{p_0} \right)$ is called the BET plot and is linear in the range $0.05 \leq \left(\frac{p}{p_0} \right) \leq 0.35$. The slope and

y-intercept can yield the numerical values for c and Q_m . By knowing the size of the adsorbate molecule one can calculate the monolayer surface area, which is referred to as the BET surface area of the material. Parameters of probe molecules used in gas physisorption study are listed in Table B-1.

Table B-1. Constants used in CO₂ and N₂ adsorption study

Adsorbate	Temperature (K)	Cross-section Area (Å ²) ²	β^3	Condensate Density (g/cm ³) ^{2,4}
N ₂	77.35	16.2	—	0.807
CO ₂	273.15	18.7	0.46	1.03

B.2. Mesoporosity

Adsorption isotherm of a mesoporous material (*i.e.*, having pore width in the range 2–50 nm) is characterized by the presence of a sudden increase in the adsorption due to the phenomenon of capillary condensation in the mesopores, typically in the range of $0.3 \leq (p/p_0) \leq 0.95$. Capillary condensation is preceded by multilayer adsorption on the surface of the mesopores (evaluated by the BET method), which occurs within $(p/p_0) < 0.3$. In the case of materials with both microporosity and mesoporosity, the adsorption proceeds in a sequence of micropore filling (see Section B.3), multilayer adsorption and finally capillary condensation mechanisms. Capillary condensation is usually characterized by adsorption and desorption branches taking different paths, resulting in a discrete hysteresis that is dependent on the pore geometry and temperature. The curvature of the meniscus of the condensate in the mesoporous regime can be described by the Kelvin equation:

$$r_K = \frac{-2\sigma_L \nu_L}{RT \ln\left(\frac{p}{p_0}\right)} \quad (\text{B-3})$$

where, ν_L and σ_L are the molar volume and the surface tension of the condensate, respectively. The pore radius can therefore be derived from the above equation after accounting the thickness of the multilayer.

$$r_p = r_K + t \quad (\text{B-4})$$

In the above expression, r_p denotes the radius of the pore and t is the statistical thickness of the multilayer. In this thesis, we use the model developed by Harkin and Jura⁵ to calculate the statistical thickness of the multilayer given by:

$$t_{HJ} (\text{\AA}) = \left(\frac{13.99}{0.034 - \log\left(\frac{P}{p_0}\right)} \right)^{1/3}, \quad t_{HJ} \in (0, 10) \quad (\text{B-5})$$

Finally, mesopore size distribution is obtained by computational algorithms, most popular among which is the BJH method named after Barrett, Joyner and Halenda.⁶ Pore size distribution obtained from the BJH method, which is based on the Kelvin equation, is reliable only for pores greater than 2 nm wide because of the inapplicability of Kelvin equation in the micropore regime. For pores below 2 nm (*i.e.*, in the micropore regime) CO₂ adsorption isotherm using the Dubinin–Astakhov method (*vide infra*) is used to analyze the porosity.

B.3. Microporosity

Microporosity analysis using CO₂ (273.15 K) as the adsorbate is favored compared to N₂ (77.35 K) because of the higher affinity of CO₂ to enter the micropores and the restricted diffusion of N₂ at 77.35 K.⁷⁻⁹ Moreover, the saturation pressure of CO₂ at 273.15 K is ~35 atm, permitting operation in low relative pressures without having a low-pressure capability in the instrument.

The Dubinin–Astakhov (DA) equation is commonly used for low relative pressure adsorption study in microporous materials and is based on the Polanyi potential theory.¹⁰

$$Q = Q_0 \exp \left[- \left(\frac{A}{\beta E_0} \right)^n \right] \quad (\text{B-6})$$

In the above equation, Q represents the volume of adsorbate (*i.e.*, CO₂) adsorbed in the micropores at adsorption potential A . Q_0 is the limiting micropore volume, E_0 is the

characteristic adsorption potential, n is the empirically-determined exponent, and β represents affinity coefficient for the adsorbate. The adsorption potential, A , is dependent on the temperature, T and relative pressure of the adsorbate (p/p_0) and is given by:

$$A = -\Delta G = -RT \ln\left(\frac{p}{p_0}\right) \quad (\text{B-7})$$

The DA equation is a generalized form of the more commonly used Dubinin–Radushkevich (DR) equation¹¹ that can be deduced by substituting the exponent, n with 2. The advantage of DA equation is that non-linearity observed for many adsorbate-adsorbent systems fitted using the DR equation can be corrected. The physical significance of n , however, is not apparent, although studies have shown that it reflects the width of the adsorption energy distribution, which can be correlated to the pore-size distribution.¹² For instance, values for n greater than 2 were obtained for homogeneous micropore distribution, such as the case in molecular sieves.¹³ DA plots of adsorbent with heterogeneous micropore distribution showed values for n less than 2.¹⁴ The DA equation can be linearized in the form:

$$\ln Q = \ln Q_0 - \left[\left(\frac{RT}{\beta E_0} \right) \ln\left(\frac{p_0}{p}\right) \right]^n \quad (\text{B-8})$$

The y-intercept yields the limiting micropore volume while the characteristic adsorption potential can be obtained from the slope of the linear curve.

Micropore size distribution is obtained by solving the inverse Stoeckli integral equation.¹⁵ Stoeckli proposed that the experimental isotherm can be considered as a cumulative effect of individual isotherms of spherical micropores, each having a particular diameter (x). Mathematically, this can be expressed as:

$$\Theta(p) = \int f(x)\theta(p, x)dx \quad (\text{B-9})$$

where, $\Theta(p)$ is the experimental “global” isotherm, $f(x)$ is the micropore size distribution function, and $\theta(p, x)$ is the “local” isotherm given by the DA equation (Equation B-8). In this thesis, *a priori* micropore size distribution function, $f(x)$, with a Gaussian distribution is considered. Finally, the micropore size distribution is obtained by solving the inverse integral equation (Equation B-9) iteratively.

Appendix B References

1. Brunauer, S., Emmett, P. H. & Teller, E. *Journal of the American Chemical Society* **60**, 309-319 (1938).
2. Walker, P. L. & Thrower, P. A. v. (M. Dekker etc., New York etc., 1965).
3. Ismail, I. M. K. *Carbon* **29**, 119-122 (1991).
4. Gregg, S. J. & Sing, K. S. W. *Adsorption, surface area and porosity* (Academic Press, London, 1982).
5. Harkins, W. D. & Jura, G. *Journal of the American Chemical Society* **66**, 1366-1373 (1944).
6. Barrett, E. P., Joyner, L. G. & Halenda, P. P. *Journal of the American Chemical Society* **73**, 373-380 (1951).
7. Reucroft, P. J. & Patel, K. B. *Fuel* **62**, 279-284 (1983).
8. Gil, A. & Montes, M. *Langmuir* **10**, 291-297 (1994).
9. Rodriguezreinoso, F., Garrido, J., Martinmartinez, J. M., Molinasabio, M. & Torregrosa, R. *Carbon* **27**, 23-32 (1989).

10. Polanyi, M. *Transactions of the Faraday Society* **28**, 0316-0332 (1932).
11. Dubinin, M. M. *Journal of Colloid and Interface Science* **23**, 487-499 (1967).
12. Dubinin, M. M. & Stoeckli, H. F. *Journal of Colloid and Interface Science* **75**, 34-42 (1980).
13. Finger, G. & Bulow, M. *Carbon* **17**, 87-91 (1979).
14. Carrascomarin, F., Lopezramon, M. V. & Morenocastilla, C. *Langmuir* **9**, 2758-2760 (1993).
15. Stoeckli, H. F. *Journal of Colloid and Interface Science* **59**, 184-185 (1977).

Appendix C. Quartz Crystal Microbalance: Background and Theory

Quartz crystal microbalance (QCM) is an ultra-high sensitive mass-balance technique used for studying surface adsorption of matter. An AT-cut single-crystal quartz wafer, such as the one shown in Figure C-1A, undergoes shear deformation under application of an AC voltage due to its piezoelectric properties. Resonance of this shear deformation occurs when the thickness of the crystal is an odd multiple of one-half times the acoustic wavelength. In other words, the surface of the crystal experiences maximum shear displacement (during resonance), while the centre undergoes no shear displacement.

In 1959, Sauerbrey showed that this resonance frequency of the shear displacement decreases linearly with any additional mass bound on the quartz crystal.¹ Consequently, the mass deposition can be assessed *in situ* by measuring the resonance frequency of the quartz crystal and applying the Sauerbrey's equation:

$$\Delta f_s^{mass} = - \left(\frac{2f_s^2}{\sqrt{\bar{c}_{66}\rho_Q}} \right) \times \rho_s \quad (\text{C-1})$$

where f_s , \bar{c}_{66} and ρ_Q are the first-harmonic resonance frequency, piezoelectric constant and density of the quartz crystal, respectively. ρ_s represents the surface density of the mass deposited on the quartz surface. Since the Sauerbrey's equation assumes no energy losses at the interface and a uniform surface mass that resonates in unison with the quartz surface, the equation is applicable only for rigid mass deposition in vacuum.

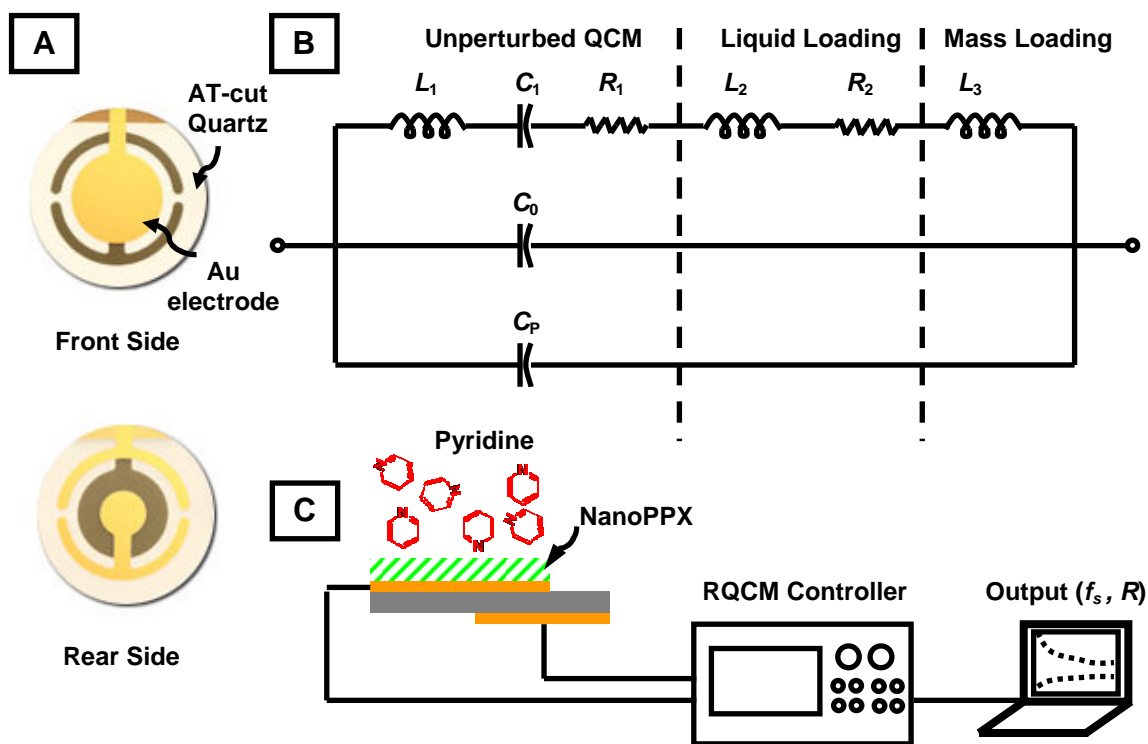


Figure C-1. (A) Front and Rear view of a SRS QCM crystal. (B) Butterworth–van Dyke (BVD) equivalent circuit diagram for simultaneous liquid and mass loading (adapted from Martin *et al.*)². (C) Schematic of the QCM experimental setup for pyridine adsorption measurement on nanoPPX films.

In 1985, Kanazawa and Gordon showed that frequency shifts arising from liquid loading can be predicted if density and viscosity of the liquid is known.³

$$\Delta f_s^{liquid} = - \left(\frac{f_s^{3/2}}{\sqrt{\pi c_{66} \rho_Q}} \right) \times \sqrt{\rho_L \eta_L} \quad (\text{C-2})$$

where, ρ_L and η_L are the density and viscosity of liquid. Later, Martin *et al.* demonstrated, using a continuum electrochemical model and experimental verification, that surface mass density can be estimated when quartz crystal is loaded simultaneously with both, liquid and mass.² Frequency shift arising from simultaneous liquid and mass loading is

obtained simply by adding the terms of the Sauerbrey's and Kanazawa-Gordon's equations, *i.e.*,

$$\Delta f_s^{simultaneous} = \Delta f_s^{mass} + \Delta f_s^{liquid} \quad (\text{C-3})$$

The continuum electrochemical modeling is achieved by means of a modified Butterworth–van Dyke equivalent circuit diagram that describes the electrical behavior of the quartz crystal (Figure C-1B). C_1 , R_1 , and L_1 represent the motional capacitance, resistance and inductance of a bare quartz crystal, respectively, while C_0 represents the static capacitance that dominates in non-resonance condition. C_p denotes the parasitic capacitance arising from the geometry of the crystal arrangement. Both C_0 and C_p are nullified prior to starting the experiment by means of a varactor diode. Under liquid loading, two additional terms, R_2 and L_2 , representing the resistance to shear deformation at the QCM/liquid interface and the corresponding frequency shift arising due to it (Kanazawa-Gordon's term) are added. A layer of rigid mass adsorbed at the surface is modeled as L_3 inducing a Sauerbrey-like condition. By solving the continuum model, analytical expressions for each term can be obtained (Equations C-4–C-10). Constants A_Q , ρ_Q , c_{66} , e_{26} , ε_{22} , \bar{c}_{66} , K_0 , and h_Q represents physical properties of AT-cut quartz, as designated in Table C-1. ω ($=2\pi f$) and ω_s ($=2\pi f_s$) denotes the angular excitation and resonance frequency (for bare crystal).

Table C-1. Properties of SRS QCM crystal (5 MHz resonance)

Description	Symbol	Value
SRS crystal area	A_Q	$1.9625 \times 10^{-5} \text{ m}^2$
Density	ρ_Q	2650 kg/m^3
Shear modulus	c_{66}	$2.901 \times 10^{10} \text{ Pa}$
Piezoelectric constant	e_{26}	-0.0966 C/m^2
Permittivity	ε_{22}	$3.982 \times 10^{-11} \text{ F/m}$
Piezoelectrically stiffened shear modulus	$\bar{c}_{66} = c_{66} + \frac{e_{26}^2}{\varepsilon_{22}}$	$2.947 \times 10^{10} \text{ Pa}$
Electromechanical coupling constant	$K_0 = \frac{e_{26}}{\sqrt{\bar{c}_{66}\varepsilon_{22}}}$	-0.0892
Effective quartz viscosity	η_Q	Empirical
Thickness (5 MHz resonance)	h_Q	$3.317 \times 10^{-4} \text{ m}$
Harmonic number	N	$= 1, 3, 5, \dots$

$$C_0 = \frac{\varepsilon_{22} A_Q}{h_Q} \quad (\text{C-4})$$

$$C_1 = \frac{8K_0^2 C_0}{(N\pi)^2} \quad (\text{C-5})$$

$$L_1 = \frac{1}{\omega_s^2 C_1} \quad (\text{C-6})$$

$$R_1 = \frac{\eta_Q}{\bar{c}_{66} C_1} \left(\frac{\omega}{\omega_s} \right) \quad (\text{C-7})$$

$$L_2 = \frac{\omega_s L_1}{N\pi} \sqrt{\frac{2\rho_L \eta_L}{\omega \bar{c}_{66} \rho_Q}} \quad (\text{C-8})$$

$$R_2 = \frac{\omega_s L_1}{N\pi} \sqrt{\frac{2\omega \rho_L \eta_L}{\bar{c}_{66} \rho_Q}} \quad (\text{C-9})$$

$$L_3 = \frac{2\omega_s L_1 \rho_s}{N\pi \sqrt{\bar{c}_{66} \rho_Q}} \quad (\text{C-10})$$

The QCM monitor (Maxtek RQCM, Inficon Inc., NY, Figure C-1C) used in our experiments allows simultaneous monitoring of frequency shift (Δf_s) and equivalent resistance change (ΔR). The expression for Δf_s and ΔR for simultaneous mass and liquid loading is given by Equations C-11 and C-12, respectively.

$$\Delta f_s = -f_s \left(\frac{L_2 + L_3}{2 \sum_{1,2,3} L_n} \right) \approx -\frac{2f_s^2}{\sqrt{\bar{c}_{66}\rho_Q}} \left(\rho_s + \left(\frac{\rho_L \eta_L}{4\pi f_s} \right)^{1/2} \right) \quad (\text{C-11})$$

$$\Delta R = (R_1 + R_2) - R_1 = R_2 = \frac{\omega_s L_1}{N\pi} \sqrt{\frac{2\omega \rho_L \eta_L}{\bar{c}_{66}\rho_Q}} \quad (\text{C-12})$$

For vapor phase adsorption, we can assume a perfectly rigid adsorption and the corresponding expressions for Δf_s and ΔR can be obtained by substituting $L_2 = R_2 = 0$.

Appendix C References

1. Sauerbrey, G. *Zeitschrift Fur Physik* **155**, 206-222 (1959).
2. Martin, S. J., Granstaff, V. E. & Frye, G. C. *Analytical Chemistry* **63**, 2272-2281 (1991).
3. Kanazawa, K. K. & Gordon, J. G. *Analytica Chimica Acta* **175**, 99-105 (1985).

Appendix D. Nontechnical Abstract

Electroless plating of polymers used for preparing polymer/metal interfaces is an indispensable technique in many engineering industries such as automotive, packaging and microelectronics. The nickel plating industry alone has an annual turnover of over \$15 billion and employs nearly 150,000 people, according to the 2003 EPA report. However, due to the chemical disparities between polymers and metals, formation of a good metal/polymer interface is often a challenge. It is therefore typical to process the polymer surface with a series of treatments including cleaners, predips, etchants, neutralizers, activators, and accelerators prior to plating step. In an industrial scale, every step not only translates into time and production costs in terms of raw-materials, machinery and management, but also generates environmentally hazardous chemical wastes. Moreover, these harsh surface conditioning treatments on polymers with nanoscale (1 nanometer = 10^{-9} m) features leads to deterioration of the desirable surface features and other physicochemical properties. It is therefore desirable to develop alternative methods to reduce the number of steps without compromising the quality of the metal/polymer interface. This thesis explores a novel technique to deposit metal layer (or nanoscale particles) on polymer surfaces with nanoscale features using an adhesive agent (*i.e.*, a ligand) stabilized on the polymer surface by weakly attractive interactions called noncovalent forces.

The polymer films used in this thesis are deposited by a technique called oblique angle polymerization (OAP) that modifies a conventional gas-phase deposition of polymers by directing the polymer precursor (monomer) flux obliquely with respect to

the substrate. The final morphology consists of obliquely aligned nanoscale rod-like (nanorod) polymeric structures on the substrate. Polymers such as, but not limited to, poly-*p*-xylylenes (PPXs or parylenes) can be deposited using the OAP method. To implement electroless plating, the polymer surface is treated with ligands such as pyridine. Subsequently, catalytic palladium-based nanoscale particle dispersions are allowed to covalently (strongly attractive interactions) bind to the ligand. Finally, metal layer can be grown onto the catalyzed surface using an appropriate electroless plating bath. The metal/polymer interface strength is contributed by the adhesive nature of the ligand and the anchoring of the metal layer to the polymer surface characterized by a natural roughness due to the aligned nanorod morphology.

The noncovalent functionalization method goes beyond the formation of simple polymer/metal interfaces. The combined characteristic of OAP-grown polymers and noncovalent functionalization technique, including the quasi-periodicity of the nanorods, the conformal nature of the metal layer, and the tunability of the underlying nanorod morphology are effectively leveraged for application in various emerging technologies. For example, cobalt membrane grown on nanoPPX film show highly interconnected porous structure that functions as an excellent catalyst for hydrogen production required in fuel-cells. Nanoscale particles of silver or gold deposited on nanoPPX films have been shown to work as excellent platforms for pathogen (bacterial and viral) and DNA detection *via* a technique called “surface enhance Raman spectroscopy” (SERS). Bioceramics such as titania can be deposited on nanoPPX films through the noncovalent route and have potential application as orthopaedic implant coatings.

VITA

Niranjan A. Malvadkar

Niranjan A. Malvadkar was born on January 27, 1984 in Pune, India. He graduated from the Indian Institute of Technology Madras, Chennai, India with Bachelor and Master of Technology in Metallurgical and Materials Engineering in June 2006. He started his graduate studies in the Engineering Science and Mechanics department at the Pennsylvania State University in August 2006. In June 2007, he joined Prof. Melik C. Demirel's research group as a research assistant. Niranjan's research interests include structure-controlled polymers, polymer surface functionalization, polymer/metal interfaces, biosensors, biomedical coatings and catalysis. During his doctoral research, he has co-authored several papers and book-chapters in the above research areas.